UNIVERSITY OF THE
WITWATERSRAND,
JOHANNESBURG

Development and Application of activated carbons from Avocado waste: Resource recovery for sustainable applications

M.Sc. Dissertation

Prepared by

Lehlohonolo Mohale (1518716)

Submitted to

School of Chemical and Metallurgical Engineering, Faculty of Engineering and the Built Environment, University of the Witwatersrand, Johannesburg, South Africa

Supervisors: Prof. Jean Mulopo and Dr. Jibril Abdulsalam

November 2023

Abstract

This research sought to produce activated carbons that could be used for hydrogen storage. The effect of hydrothermal pretreatment of the char, the effect of varying the activation ratio of KOH as the activation agent and the effect of activation temperature in producing these activated carbons were evaluated. Hydrothermal pretreatment of the char enhanced the properties of the resulting activated carbons. The best performing activated carbon was produced from the hydrochar pretreated at 200℃. It was observed that activation improved with increased activation agent concentration and activation temperature, to a point, and the best activated carbon was produced at 1:3 activation ratio and 800℃ activation temperature. This activated carbon had the highest total pore and micropore volumes of 1.45cm^3/g and 1.16 cm^3/g, respectively. The highest surface area of 2529.8m^2/g was obtained, which is relatively higher than previously reported surface areas obtained from activated carbons created from coal or biomass. The porosity and the high surface area show well developed activated carbons that have desirable gas adsorption performance. The activated carbons had oxygen containing functional groups that aid in hydrogen sorption, the highest hydrogen sorption at 77K and 1 bar was 352 cm^3/g, which supports the use of the produced activated carbons in the hydrogen economy. These activated carbons enable the circular economy. Well developed micropores were observed in the activated carbons produced through this work and their gravimetric capacity meets the DOE targets for hydrogen storage.

Author's Declaration

I declare that the work in this thesis was carried out in accordance with the requirements of the University of Witwatersrand's Regulations and Code of Conduct for Research Degree Programmes. This work is the authors, except for instances where reference to other people's work is made. Collaborations and assistance from others is recognised as such. Views expressed in this thesis are those of the author.

L.J Mohale

15 November 2023

Acknowledgements

To my supervisors, Jibril Abdulsalam and Jean Mulopo, thank you for all your guidance and support throughout this project. It has been a journey characterized by so many things, including loadshedding that delayed my progress for months as I could not test some of the samples.

To all the staff at Richard Ward, I will always remember your generous support and dedication to the success of this project. A special shout out to Letta Ntuli, you were always willing to help and your contribution to this project is immeasurable.

To my family, you have been my support system from when I shared with you my ambition to take on this project. You believed in me and continued to encourage me. Your constant reminders pulled me up even when I thought to give up. It was not an easy journey, but you stood by me. I have not been there for all the special events and holidays because of this project but you understood and wished me well.

To my friends, church and colleagues, you are the best community one could ask for. A special shout out to the following people: Pfano Mulaudzi, you were there when this journey started. Your support meant the world to me. To Karabo Seerane, thank you for checking up on me and reminding me of the work I needed to put into this project. A special thank you to Nolwazi Mamba, your support and cheerleading reminded me of why I embarked on this journey. I cannot mention all of you by name, but know that your support, curiosity and listening to me vent about this project will always remain in my heart.

Author Contributions

The work presented in this document was done by Lehlohonolo J. Mohale. The following contributions are recognised:

Jibril Abdulsalam (University of the Witwatersrand) and Jean Mulopo (University of the Witwatersrand) provided guidance and supervision throughout the project. They also reviewed and provided feedback on this document.

Letta Mbuli (University of the Witwatersrand) assisted with the FTIR, XRD and TGA analyses.

Motlatsi Phali (University of the Witwatersrand) and Meshack Thivhani (University of Johannesburg) assisted with the CHNOS analysis of the samples.

Petra Dinham (University of the Witwatersrand) and Zaynab Cader (University of the Witwatersrand) assisted with the SEM/EDS analysis of the samples.

Abbreviations

AC	Activated Carbon
AfCFTA	African Continental Free Trade Area
CE	Circular Economy
HC	Hydrochar

Contents

List of Figures

List of Tables

CHAPTER 1: INTRODUCTION

1.1 BACKGROUND AND MOTIVATION

1.1.1 Background

The objective of this research was to produce activated carbons derived from avocado waste in order to evaluate their efficacy as adsorbents for hydrogen storage.

Numerous sectors continue to rely on fossil fuels as their primary source of energy. Fossil fuels have been found to contribute significantly to environmental degradation and pose ecological risks. Furthermore, their reserves are being depleted. Fossil fuels encompass a range of hydrocarbon molecules, such as coal, petroleum, natural gas, oil shale, and heavy oils (Shahzad, 2012). Significant volumes of noxious gases are emitted during the combustion of fossil fuels. Carbon dioxide is well recognized as one of the most prevalent hazardous gases (Abdalla et al., 2018). Carbon dioxide and various other greenhouse gases are responsible for the phenomenon of global warming, leading to elevated temperatures on a global scale. According to Shahzad (2012), the elevated temperatures have the effect of rendering the living conditions exceedingly inhospitable for various animal and plant species worldwide. Moreover, the elevated temperatures have led to the melting of ice in the Arctic and Antarctic areas, resulting in potential consequences such as floods and significant impacts on marine life, fisheries, and agricultural operations (Andersen, 2007).

According to Conserve Energy Future (2015), further drawbacks associated with the utilization of fossil fuels encompass the requirement for substantial reserves, the creation of pollution and its consequential health implications such as chronic asthma and cardiovascular diseases, occurrences of oil spills, and the worsening of the well-being of coal mine workers. Sulphur dioxide is a byproduct released during the combustion of fossil fuels. The combination of rain and certain pollutants results in the formation of acid rain, which has detrimental effects on the environment. This includes the degradation of soil, rendering it unfit for agricultural purposes, as well as the infiltration of water tables and catchment systems, leading to the contamination of water sources, thereby making it unsuitable for drinking and other general uses. Coal mining-related activities have been associated with a significant number of fatalities.

Shahzadd (2012) asserts that there has been an increasing energy demand in tandem with expanding populations. It is inevitable that non-renewable energy sources are being depleted, thus necessitating a critical transition towards alternative renewable energy sources. According to Shahzad (2012), it is imperative to consider the environmental consequences of renewable energy sources as we navigate the shift towards sustainable energy production, alongside various other considerations.

The implementation of astute energy policies can bolster the economy by promoting sustainable energy development, leading to increased productivity and enhanced social welfare as living standards rise. Simultaneously, the enhancement of the population's safety and security is accompanied by the preservation of the environment through the reduction of pollution (Oyedepo, 2012). The oil industry significantly contributes to Nigeria's Gross Domestic Product (GDP). Nevertheless, despite the abundance of reserves, the nation is currently grappling with an energy crisis (Oyedepo, 2012). In addition to this, it is noteworthy that the energy sector incurs substantial system losses (ranging from 33% to 41%) and various other variables contribute to the high cost of energy. In 2004, the energy consumption per capita in Nigeria was approximately 776.9 kgoe, while in South Africa, with a population of around 44 million people, it was approximately 2596.9 kgoe. This disparity can be attributed to the scarcity of petroleum products and frequent blackouts experienced in Nigeria during that period (Oyedepo, 2012). South Africa lacks the huge energy reserves that Nigeria possesses. Nonetheless, it is important to note that there are comparable obstacles associated with both traditional and alternative energy sources. These problems encompass issues such as the availability of these energy sources and the adverse impacts they have on the environment, society, public health, ecosystems, and various other aspects. The importance of sustainable energy development is equally significant for South Africa as it is for the global community.

The role of energy is crucial in the advancement and long-term viability of any economy. According to Mineral Energy and Resources (2019), the country's economic activities such as manufacturing, businesses, transportation of commodities, and the delivery of services are heavily reliant on this factor. The energy sector has a crucial role in promoting economic and social development in South Africa (MER, 2019). Coal is the prevailing primary energy source in South Africa. In addition to biomass (wood, dung, etc.), natural gas, hydropower, nuclear power, solar electricity, and wind also provide significant contributions to the overall energy mix. According to the South African National Development Plan 2030, there is a stated objective to ensure a sufficient energy supply, aiming for about 95% of the population to have access to either the grid or off-grid energy source by the year 2030 (MER, 2019). According to the data from the International Energy Agency (IEA) publication titled "World Energy Balances: Overview 2019," renewable energy sources and waste accounted for around 11% of South Africa's total energy consumption in the year 2016. Based on the findings presented in the South African Energy Sector Report of 2019, it can be argued that South Africa possesses favourable conditions for the expansion of renewable energy generation. The aforementioned option is increasingly demonstrating its viability in the current context. The Renewable Energy Independent Power Producers Procurement Programme (REIPPP) has garnered both domestic and international funding. In addition to this, there has been a notable rise in small and medium-sized enterprises (SMEs) directing their attention towards the development and utilization of renewable energy sources

(MER, 2019). The green economy has been recognized as having the potential to provide approximately 5 million more employment opportunities (MER, 2019).

South Africa experiences a significant energy requirement, with the majority (about 52%) allocated to the industrial sector. The transport sector accounts for 19% of the energy demand, while commerce and agriculture contribute 14%. Residential areas consume 8% of the energy, with agricultural utilizing an additional 6%. The remaining 1% is allocated to an unspecified category (MER, 2019). It is evident that a shift towards sustainable, efficient, environmentally friendly, and renewable sources of energy is imperative. One notable and pressing characteristic of renewable energy is its abundant availability. Moreover, it should be noted that these renewable energy sources possess the desirable attributes of being environmentally friendly and free from potential hazards. The primary sources of renewable energy encompass sun, wind, geothermal, hydropower, and biomass (Shahzad, 2012). According to Shahzad (2012), the utilization of these sources has the potential to stabilize energy costs, despite the significant expenses associated with the initial investment. As the aforementioned industries experience expansion, a concomitant increase in employment prospects is anticipated on a global scale, as well as within the local context of South Africa.

1.1.2 Motivation

Energy security, environmental preservation, and waste beneficiation

There is a pressing need to advance the development of technologically advanced solutions that effectively tackle energy security and climate change in a sustainable manner. It is imperative to ensure that the existing population can reap the benefits of such technologies, while also fostering opportunities for future generations. The primary objective of this technology should be to prioritize the utilization of waste materials in order to minimize the need for waste storage and disposal, while simultaneously maximizing the potential advantages derived from the energy generated. Therefore, the primary objective of this study was to investigate the utilization of avocado waste as a viable feedstock for the synthesis of highly porous activated carbon. The resulting activated carbon material would serve as a potential medium for hydrogen storage, so offering a sustainable alternative to existing energy sources, such as crude oil, which are non-renewable, environmentally hazardous, unsafe, costly, and unreliable.

Hydrogen promotes itself as a more environmentally friendly and secure substitute, with a substantial capacity for energy production. There exists a variety of hydrogen sources, encompassing both renewable and non-renewable options. The selection of a particular source depends on factors such as accessibility, availability, hydrogen potential, and process efficiency (Marbán and Valdés-Solís, 2007).

Hydrogen market and hydrogen economy

BP Global (2021) asserts that hydrogen fuel possesses a substantial and enduring presence in both local and global markets. It is imperative for South Africa to engage in the fuel transition, since it holds the potential for substantial benefits. According to BP Australia, their projected outcomes in terms of business strategy and implementation have the potential to position Australia as a prominent player in the regional energy transition. South Africa possesses the necessary renewable resources, production and distribution facilities, as well as a well-established network, which positions it favourably to actively participate in the ongoing energy transition (CSIS, 2022; Anglo-American, 2022; PEI, 2023). The African free trade agreement, which was ratified in January 2021, provides South Africa and other African nations with the technological capacity to lead and achieve equitable and advantageous profit margins in the context of the energy transition. This is particularly significant considering that Africa has historically not received equal benefits from energy advancements. The establishment of a market and improved market access through this agreement can facilitate the aforementioned outcomes (African Union, 2018).

1.2 RESEARCH PROBLEM STATEMENT

It is imperative to advance the development of energy technologies that are characterized by enhanced safety, improved cleanliness, and greater environmental friendliness. These technologies should be designed to foster equitable economic and social growth, while ensuring that individuals with low incomes and those residing in developing countries are not marginalized. Hydrogen has emerged as a promising energy source for the future. Nonetheless, the comprehensive incorporation of this technology into the future energy framework necessitates the establishment of essential infrastructure for production, delivery, and storage. In order to attain cost-effective hydrogen storage, it is advisable to utilize abundant waste products as both raw materials and precursors for the development of hydrogen storage materials that exhibit high efficiency. This approach not only addresses difficulties related to waste disposal and storage, but also presents prospects for further exploration and utilization.

In this context, the current study synthesised nanoporous carbon composites from avocado waste with the goal of storing hydrogen.

1.3 HYPOTHESIS

Porous carbon materials derived from avocado waste will have a good pore structure for hydrogen storage.

1.4 RESEARCH QUESTIONS

i. Can avocado waste be considered a suitable feedstock for producing porous carbon materials?

ii. Can activated carbon obtained from avocado waste serve as a viable solution for hydrogen storage applications?

1.5 RESEARCH AIM AND OBJECTIVES

The aim of this research project is to synthesise activated carbons that are highly porous, from avocado waste, for hydrogen storage.

The specific objectives include:

- Obtain, prepare and characterize avocado waste in terms of moisture, ash, volatile matter, fixed carbon, carbon, and sulphur
- Hydrothermal pretreatment of the avocado waste at different reaction temperatures
- Synthesis and characterize activated carbons from the obtained hydrochars using chemical (KOH) activation method
- Measure the adsorbed amount of hydrogen onto the activated carbons
- Evaluate the heterogeneous surface characteristics of the synthesised porous carbons in terms of energy distribution using a universal isotherm model

1.6 DISSERTATION OUTLINE

To meet the aim and objectives of this study, it has been divided into five chapters.

Chapter 1 offers an overview of the research topic, along with the rationale for conducting the study and its significance. It also provides a clear definition of the research problem or questions that the dissertation addresses. The chapter outlines the aim and specific objectives of the study, as well as an outline of the dissertation's structure.

Chapter 2 provides a review of existing literature by critically analysing the relevant literature on the hydrogen economy, challenges to hydrogen storage and expected targets, different types of hydrogen storage methods, hydrogen storage in activated carbons, the circular economy, avocado waste and the modelling of hydrogen adsorption onto activated carbon.

Chapter 3 describes the materials and methods used in the study. Within this chapter, the procedures for collecting raw materials, their preparation, and subsequent characterization are highlighted, including the hydrothermal pretreatment and the synthesis of activated carbon. The design of experiment, characterization techniques and equipment used also feature in this chapter.

Chapter 4 presents the research findings in a clear and organized manner, using tables, charts, and graphs as needed. The chapter discusses results from the synthesis and characterization of activated carbons from avocado waste, hydrogen adsorption properties of the activated carbons and the modelling of hydrogen adsorption onto activated carbons using the Universal Isotherm model.

Chapter 5 summarizes the key findings of the study and their significance. This chapter highlights the research's contribution to the field, offers recommendations based on the research findings, and suggests potential areas for future research.

CHAPTER 2: LITERATURE REVIEW

2.1 Global Energy Trends

Energy demand has seen a massive increase with population and income growth. The global population was estimated at 1.6 billion people in 1900, 6.149 billion in 2000 (about 284% increase in 100 years), and 8 billion (about 30.8% increase in 23 years) in 2023 (Worldometer, 2023). This is more than 400% increase in over a hundred and twenty-three years and is expected to grow even further, refer to figure 2.1 and figure 2.2. World gross domestic product (GDP), adjusted for inflation and differences in cost of living between countries, has increased exponentially from an estimated $3.42 trillion in 1900 to $105 trillion in 2023 (IMF, 2023). Global real income has increased over the same period, resulting in higher production and energy consumption for various purposes, including transportation, heating, fuel, etc. About 451 million terajoules of energy was estimated to be used in 2023 as of October 10, this is expected to reach 740 million terajoules by 2040 (The World Counts, 2023). As shown in Figures 2.1 and 2.2, population and income growth are the most significant factors driving energy demand (BP, 2011).

Fossil fuels make up about 83 percent of the energy we consume today, with oil being the largest contributor, followed by coal and natural gas (The world counts, 2023). Fossil fuels have two associated challenges: their usage often results in detrimental environmental impacts, and they are available in a limited supply, taking a long period to replenish or never. This cannot keep up with the accelerating energy demand and the need to conserve the environment.

The International Energy Agency's report published in the second quarter of 2023 details the global energy outlook for 2030. In the report, there is a view that current energy transitions will result in a massively different global energy system by 2030 (IEA, 2023a). It is further argued that the rise of clean energy technologies has shifted how we power most of the systems we use daily (IEA, 2023a). The World Energy Outlook, which is the principal global energy analysis and projections authority, projects a world in which there will be about ten times the number of electric cars, efficient power generation through solar PVs which surpasses today's US power system output, an increase from 30% to close to 50% contribution by renewable energy in the energy mix, fossil fuel heating systems being replaced by electric heating systems and more investments dispatched

towards wind energy by 2030. These projections were made in line with the policy positions of governments across the globe. An improvement in executing national commitments towards clean energy and environmental conservation is expected to see these projections being surpassed. While each sovereign state determines how to achieve its commitments, international cooperation is proving resourceful.

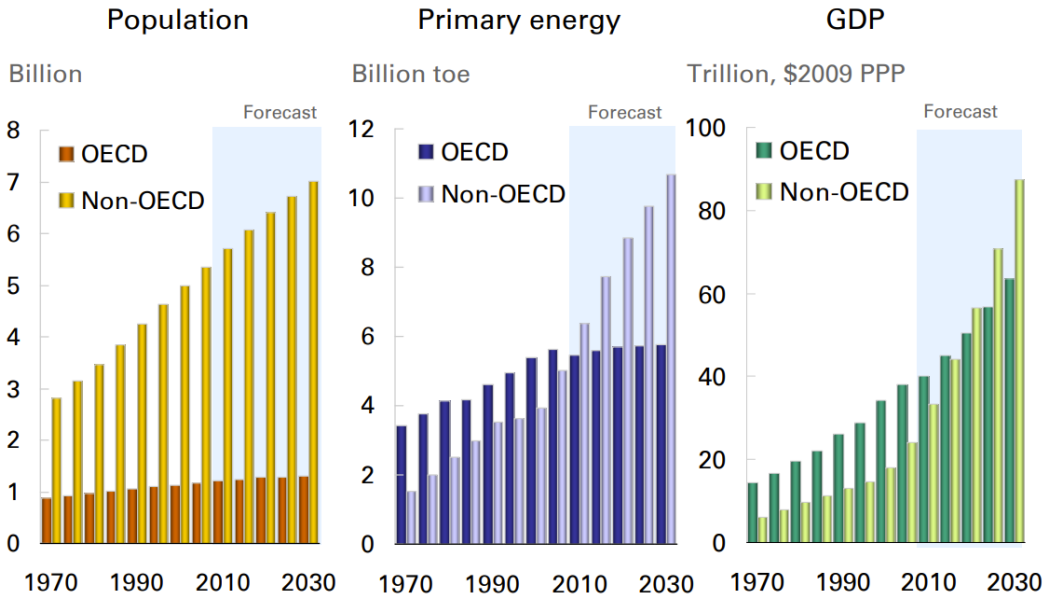

Figure 2.1 Global population, primary energy source, and GDP growth over 60 years forecasted to 2030. (BP, 2011)

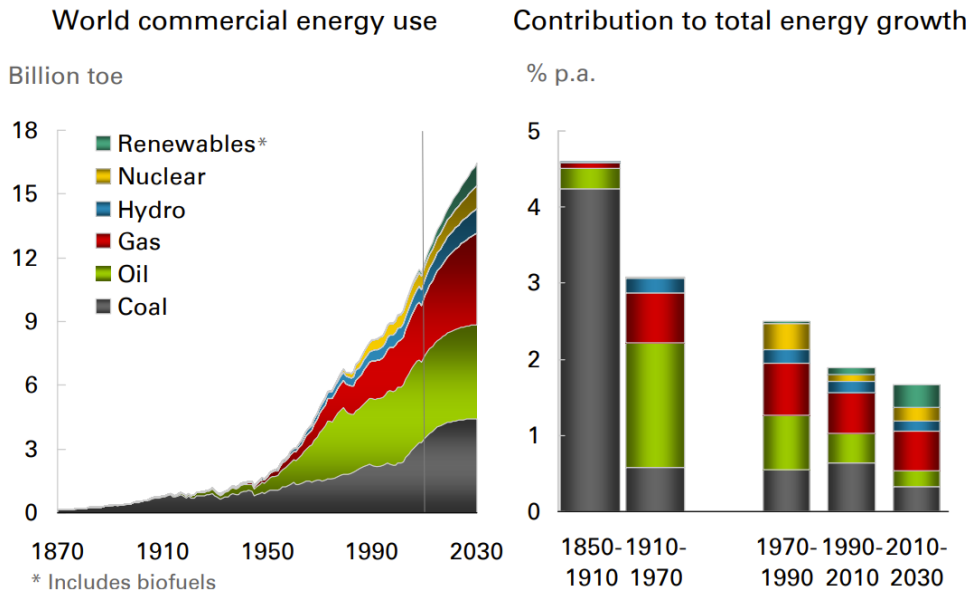

Figure 2.2 Global energy consumption and fuel mix (BP, 2011)

Fossil fuels, categorised into natural gas, oil, and coal, are expected to peak if governments maintain their policy positions with decreased demand after getting over the effects of the 2022 global energy crisis, which was in part due to the Russia-Ukraine war (World Energy Outlook, 2023). Figure 2.3 shows that these three fossil fuel types are expected to peak by 2030, with coal being expected to peak the soonest around 2023/4, followed by oil and natural gas around 2028/9. It is important to note that this does not represent a unified view worldwide since reduced demand in the wealthier countries is offset by increased demand and use of fossil fuels in the poorer and developing economies. The demand curve for fossil fuels is also not expected to flatten out even past the 2050 projected mark. The smooth projections are still expected to alter as things change, such as a spike during hectically colder seasons or natural disasters that cannot be predicted and modelled accurately.

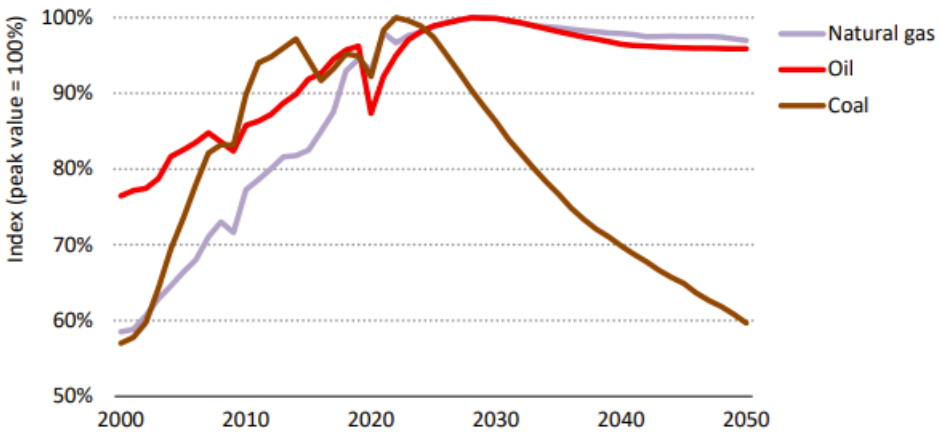

Figure 2.3 Fossil fuel consumption (World Energy Outlook, 2023)

In June 2023, the IEA published the Government Energy Spending Tracker report, which tracked 1600 government financial measures of 67 countries, tracking two areas of spending policies: (i) clean energy investment support and (ii) short-term energy affordability measures. Economic recovery packages from COVID-19 and the 2022 energy crisis have seen governments redirect a lot of money and fiscal attention towards supporting clean energy initiatives, resulting in more than twice the amount committed after the 2007/8 financial crisis. Figure 2.4 shows the massive shift in spending in just the past three years and a tightening of policies and provisions to make clean energy more affordable. Energy affordability has been a priority for most governments after

the global energy crisis. Most of the added financial support/investment came from the USA, the European Union member states, the United Kingdom, and Norway (IEA, 2022).

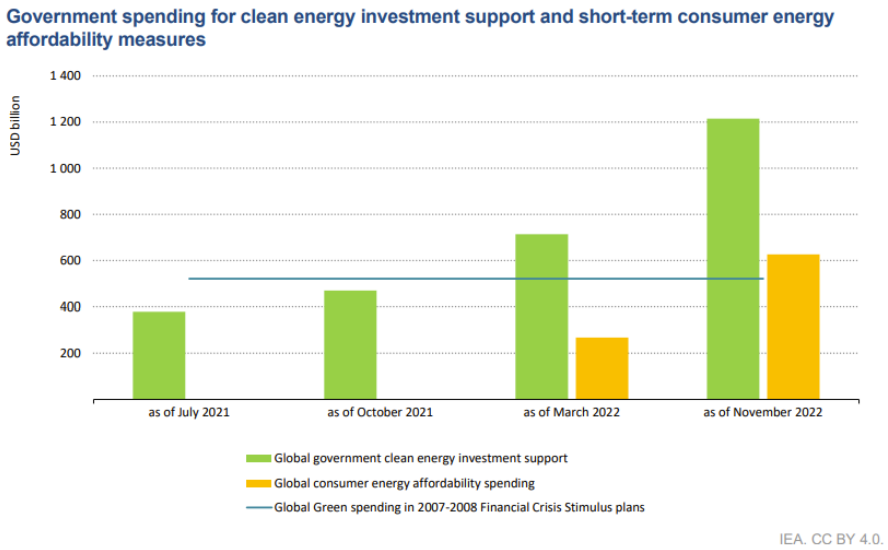

Figure 2.4 Clean energy investments by 67 global governments (IEA, 2023)

2.2 The Hydrogen Economy

The hydrogen economy is a hydrogen-based system of delivering energy. The term was first used by John Bockris in 1970 during his presentation at the General Motors (GM) Technical Center (Abe *et al.*, 2019). Hydrogen is the most abundant element on Earth but does not occur naturally in its elemental form. It must be prepared from other molecules. It is an energy carrier and not a primary fuel. The hydrogen economy is a promising solution to some of the negative effects of using hydrocarbon fuels, where carbon is released into the atmosphere.

Hydrogen gas has the highest energy per unit of weight, 286 kJ/mol, amongst all chemical fuels. It is highly abundant as it is bonded to many molecules and compounds we use. It is environmentally friendly, releasing water and energy as it combusts.

Reaction of hydrogen:

$$H_2 + {}^1/_2\, O_2 \rightarrow H_2O + energy \qquad (2.1)$$

Calculations show that hydrogen has the highest energy storage capacity, with 1 kg of hydrogen-containing about 120 MJ or 33.33 kWh of energy, which is more than that of normal fuels (Abe *et al.*, 2019). Table 2.1 compares a number of fuels to drive this point. The main aim of the hydrogen economy is to produce hydrogen fuel from readily available energy sources.

Table 2.1: A comparison of the energy content of select fuels (Abe *et al.*, 2019)

Fuel	Energy contents [MJ/kg]	
	Lower heating value	Higher heating value
Gaseous hydrogen	119.96	141.88
Liquid hydrogen	120.04	141.77
Natural gas	47.13	52.21
Liquified Natural Gas (LNG)	48.62	55.19
Still gas (in refineries)	46.89	50.94
Crude oil	42.68	45.53
Liquefied Petroleum Gas (LPG)	46.60	50.14
Conventional gasoline	43.44	46.52
Reformulated or Low-Sulphur Gasoline (RFG)	42.35	45.42
Conventional diesel	42.78	45.76
Low-Sulphur diesel	42.60	45.56
Coal (wet basis)	22.73	23.96
Bituminous coal (wet basis)	26.12	27.26
Coking coal (wet basis)	28.60	29.86
Methanol	20.09	22.88
Ethanol	26.95	29.84

2.2.1 Hydrogen: The most promising renewable energy source

In the scope of renewable energy sources, hydrogen is proving quite a viable source. The move towards hydrogen usage will help to reduce the current carbon dioxide concentration in the atmosphere, which is more than 30% above the pre-industrial era (Marbán and Valdés-Solís, 2007; Zhao, 2012). This transition will allow the 196 Paris Agreement member parties and similar international agreement member nations to satisfy their political commitments and social responsibilities of reducing atmospheric carbon dioxide concentrations/outputs.

The Paris Agreement is a formal pact amongst the member states, which was adopted at COP 21 in Paris on the 12th of December 2015 and took effect on the 4th of November 2016. It sets out to limit global warming to less than 2 ^{o}C of the pre-industrial levels. Countries were expected to submit their nationally determined contributions (NDCs) by 2020, outlining their plans to achieve the agreement's goals. The agreement also outlines member parties' financial, technical, and capacity support plans. Progress will be tracked through an enhanced transparency framework (ETF) beginning in 2024, through which countries are expected to report on their actions and progress transparently. There have been notable improvements since the agreement's adoption, including low-carbon solutions and their markets. Power generation and transport sectors are developing more competitive low-carbon technologies (UNFCCC, 2020). The Paris Agreement has also heightened the interest and funding deployed towards the hydrogen economy by member states and those inspired by its resolutions.

The shift to hydrogen is expected to further decentralize energy production, as is now evidenced through oil production by only a few countries whose political and economic instabilities have led to uncertainties in both access to the fuel and its price. Recent developments in Russia, the war, and its impact on the fuel price, which moved from the 60 dollars per barrel region to economically crippling highs of 120 dollars per barrel during the global energy crisis, is an example of this. Hydrogen is a readily available and abundant energy source that can be relied upon for long-term stability, security, and affordability, all of which are critical for the growth of low- and middle-income countries. Most non-renewable energy sources we rely on can be replaced with hydrogen, which has higher energy potential and refills faster than most.

BP stated in 2021 that large-scale hydrogen generation via renewable energy sources is feasible (BP Global, 2021). Significant infrastructure investment in ports, water and energy networks, and distribution will be required to keep up with this level of expansion and growth (BP Global, 2021). In addition to being better, more accessible, and more scalable, hydrogen is a better alternative.

The hydrogen economy comprises five key areas: production, delivery, storage, conversion, and application. Figure 2.5 shows a schematic of these areas.

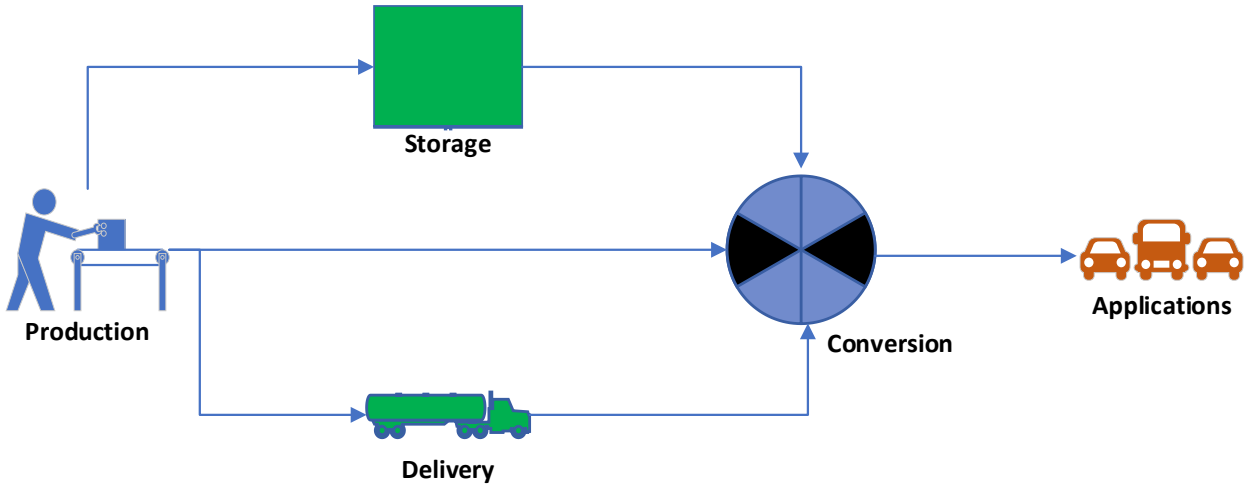

Figure 2.5 Key components of the hydrogen economy

Mining businesses in South Africa have made efforts to decrease their carbon emissions and transition towards decarbonization within the industry. The incorporation of the hydrogen economy into their corporate strategic imperatives and frameworks has facilitated the realization of a sustainable energy transition. The utilization of platinum group metals, which are prominent minerals extracted in South Africa, has been noted in the application of polymer electrolyte membrane (PEM) electrolysers. PEM electrolysers are used to produce hydrogen fuel and in fuel cells to produce electricity from hydrogen, as shown in the fuel cell reactions below (Anglo-American, 2022; Energy.gov, 2021).

Anode Reaction: $2H_2O \rightarrow O_2 + 4H^+ + 4e^-$ (2.2)

Cathode Reaction: $4H^+ + 4e^- \rightarrow 2H_2$ (2.3)

In October 2021, Anglo America, a prominent producer of Platinum Group Metals (PGMs) with operations in South Africa, conducted a hydrogen feasibility study in partnership with the Department of Science and Innovation (DSI), the South African National Development Institute (SANEDI), ENGIE, and Bambili Energy (Anglo-American, 2022). The objective of this initiative was to establish a hydrogen valley within the country, wherein various industrial stakeholders and researchers would undertake many experimental projects.

The research conducted successfully identified three central hubs, namely Johannesburg, Durban, and Limpopo. The projected demand for hydrogen in these hubs is estimated to reach 185 kilotons by the year 2030, as reported by CSIS in 2022. The Johannesburg hub encompasses the regions of Rustenburg and Pretoria, whereas the Durban hub extends its coverage to include Richards Bay. Additionally, the Limpopo hub is situated within the Mogalakwena PGM mine, as depicted in figure 2.6. According to Anglo-American (2022), the hydrogen valley under consideration possesses the capacity to generate an annual estimate ranging from 14,000 to 30,000 jobs, both directly and indirectly. Additionally, it is projected to provide a noteworthy contribution of $4 to $9 billion to the South African GDP. The evaluation proceeded to identify nine pilot projects that were to be promptly initiated following prioritization by the appropriate parties.

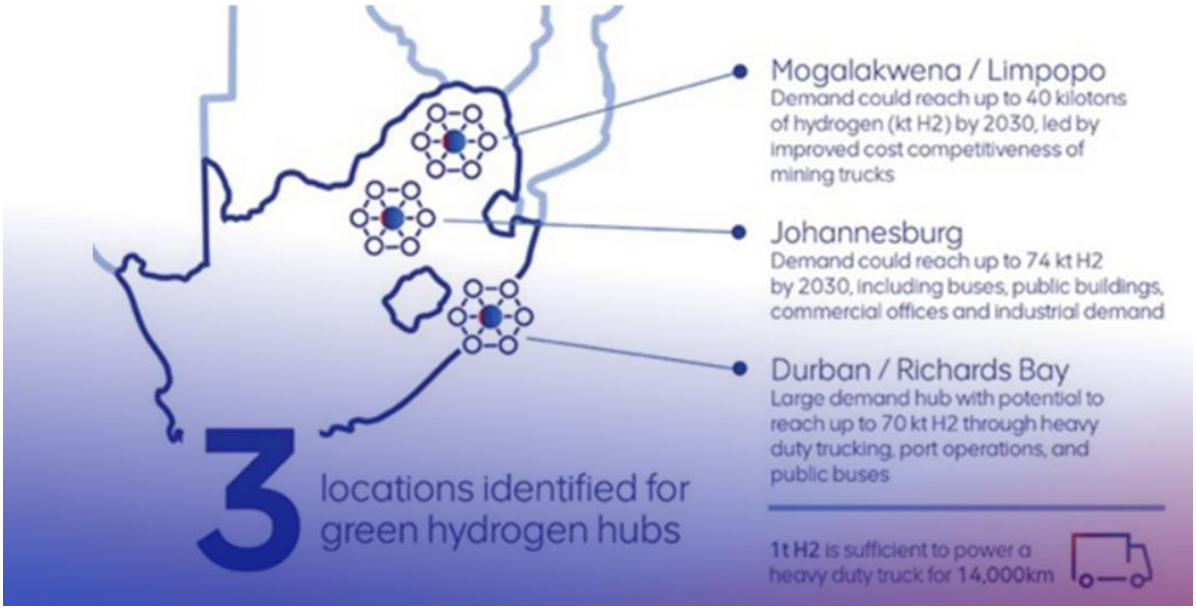

Figure 2.6 Green hydrogen hubs identified through the Anglo-American and partners study (Anglo-American, 2022)

Anglo American South Africa successfully implemented a hydrogen conversion project for a mining haul truck with a weight of 510 tonnes. This conversion involved the utilization of on-site hydrogen production, hence enabling the truck to operate on hydrogen fuel (Anglo-American, 2022). The implementation of this initiative is intended to be extended to their expansive worldwide collection of over 400 trucks. South African firms have initiated or are about to initiate various projects, such as Anglo-American's integrated green hydrogen production, fueling, and haulage system for mines, aimed at achieving zero emissions in the haulage sector.

The Centre for Strategic and International Studies (CSIS, 2022) reports that South Africa has set a goal to establish itself as a prominent producer and exporter of green hydrogen, with the objective of capturing a 4 percent share of the global market by the year 2050. The country aims to enhance the demand for green hydrogen and its associated products. Four primary initiatives have been identified with the aim of expanding the utilization of hydrogen on a national scale and fostering prospects for exportation. The aforementioned projects include the PVI project, COALCO2-X project, Sustainable Aviation Fuels (SAF) project, and Boegoebaai hub. The primary objective of the PVI project is to establish a hydrogen corridor that connects the mining activities in Limpopo with the industrial sectors in Johannesburg, ultimately facilitating transportation to the port of Durban. As part of its initiatives, one of the strategies would involve the conversion of diesel trucks into trucks powered by fuel cells, hence resulting in an augmented need for hydrogen inside the valley. The primary objective of the COALCO2 -X initiative is to employ hydrogen as a means to extract pollutants from coal-fired boilers, so enabling the production of more valuable commodities such as fertilizers, green ammonia, and synthetic acids (CSIS, 2022). The primary objective of the Sustainable Aviation Fuels (SAF) initiative is to mitigate carbon emissions within the aviation sector through the utilization of hydrogen-based fuels, hence promoting environmental sustainability. Finally, the Boegoebaai hub encompasses an industrial area that will serve as the location for several facilities including an electrolyser park, a green ammonia production plant, a desalination plant, a storage facility, a solar, wind, and battery park, a gigafactory dedicated to the manufacturing of electrolysers, and a supplier park. The South African government has allocated funds to aid with these efforts, in addition to various local and international collaborations and funding alternatives accessible to the country, such as public-private partnerships.

As an integral component of the Boegoebaai hub, South Africa aims to achieve an annual hydrogen production capacity of 500 kilotons by the year 2030. This ambitious target will be realized through the utilization of electrolysis equipment with a total capacity of 10 gigawatts, strategically located in the Northern Cape region. The country intends to inaugurate its inaugural Boegoebaai port, which is a constituent of this interconnected system, in the year 2026. Boegoebaai is set to emerge as the focal point for hydrogen export infrastructure, owing to its robust infrastructure and comprehensive support operations headquartered inside the region. The implementation of this project is anticipated to yield positive impacts on local economies, with the creation of over 6000 direct possible jobs. These employment prospects will mostly be concentrated in the areas of port operations and infrastructure rail development..

South Africa possesses several attributes that render it a viable contender for the production of green hydrogen. Several reasons contribute to the country's suitability for wind and solar energy production, one of which being the geography characterized by expansive open landscapes. The country possesses a significant quantity of mines, particularly those which specialize in the extraction of platinum group metals (PGMs) which are used in electrolysers. The country is moreover encompassed by oceans, thereby providing a plentiful source of water for the production of hydrogen. South Africa has also a historical track record of producing grey hydrogen, which is akin to blue hydrogen but lacks the implementation of carbon capture and storage. This process involves the utilization of natural gas or methane by steam methane reformation.

Another notable initiative leveraging on the green hydrogen economy in South Africa is the collaboration of Sasol, a prominent global company specializing in chemicals and energy, and ArcelorMittal, the primary steel manufacturer in sub-Saharan Africa. A collaborative effort has been initiated by the parties concerned to advance the development of carbon capture technologies that yield sustainable fuels, chemicals, and facilitate green steel production via the utilization of hydrogen. One of their significant undertakings is the Saldanha green hydrogen and derivatives study, which entailed an examination of the feasibility of turning the region as a centre for green steel manufacturing and green hydrogen exportation. One such study conducted was the Vaal carbon capture and utilization (CCU) investigation, which aimed to transform carbon captured from the steel manufacturing facility in Vanderbijlpark operated by ArcelorMittal South Africa

into sustainable fuels and chemicals through the utilization of renewable electricity and green hydrogen (PEI, 2023).

The Coega hydrogen development project is an additional initiative that is of significant interest. According to a report by PEI (2023), the project aims to generate green ammonia to cater to the clean fuel and maritime industries in Asia and Europe. Additionally, the emergence of a variety of wind and solar assets is projected. The proposed project will consist of the implementation of a desalination plant and a wastewater recycling system with the objective of expanding the available feedstock for hydrogen production.

Despite the numerous opportunities available, there are also significant challenges that impede the complete realization of the hydrogen economy. These factors encompass a range of elements such as skill sets, physical infrastructure, industry-specific expertise and assistance, regulatory frameworks, domestic and international marketplaces, and other associated aspects..

2.3 Challenges to Hydrogen Storage and Expected Targets

Hydrogen is the most abundant element but does not occur in its elemental form. It has to be harnessed from other molecules, making it an energy carrier and not a primary fuel (Zhao, 2012). The cost of producing, delivering, and storing hydrogen at levels similar to those of the current conventional fuels is high and non-competitive, making it necessary to find competitive, cost-reducing technologies (Energy.gov, 2009; Zhao, 2012).

To enable its daily usage, hydrogen storage is "a crucially missing step towards the hydrogen economy" (Zhao, 2012). Another key issue with the competitive use of hydrogen is that in as much as it has a significantly high energy content per unit mass, it has a low energy content per unit volume due to its extremely low density compared to conventional fuels. This means you need massive capacity to store the same amount of hydrogen as conventional fuels (Blackman, 2005; Zhao, 2012). Hydrogen is a supercritical gas under standard conditions (Tc = 33.19 K, Pc = 1.296 MPa), meaning that it has quite a very low density of 90 g/m^3 at 1 bar and 273 K (Zhao *et al.*, 2017). The volumetric energy density of liquid hydrogen is more than three times lower than that of petrol (Georgiev *et al.*, 2006). Hence, it is imperative to form dense condensed phases as the

bulk solid at temperatures way above 14 K, the triple point of bulk hydrogen (Georgiev *et al.*, 2006).

Four kilograms of hydrogen gas required for normal driving would occupy $49m^3$ at room temperature, which is too much and makes storing and commercializing hydrogen difficult. Hydrogen storage will need to meet the normal tank volume and weight requirements to be used for transportation applications. Stationary applications are much easier to deal with regarding storage requirements. However, mobile applications require range, charging and recharging, and fast fuel injection rates (Georgiev *et al.*, 2006).

According to Energy.gov (2009), the US Department of Energy (DOE) requires that hydrogen storage systems meet three fundamental criteria for automotive applications: they must be reversible, have a gravimetric density around 6 wt.%, and heat of adsorption (ΔH_{ads}) within the 20–30 kJ/mol range (Bhatia and Myers, 2006; Zhao, Kim, Dillon, Heben and Zhang, 2005). Table 2.2 presents the new and old targets for hydrogen storage systems for light-duty vehicles. Considering the revised requirements, the storage challenges must be addressed before hydrogen can effectively be used. The hydrogen economy depends on the development of good, suitable storage mechanisms.

Table 2.2: US Department of Energy (DOE) new and old targets for hydrogen storage (US DOE and FCFP, 2009)

Target	***2010 (new)***	***2010 (old)***	***2015 (new)***	***2015 (old)***	***Ultimate Full Fleet***
System Gravimetric Density (% wt)	4.5 (1.5 kWh/kg)	6 (2.0 kWh/kg)	5.5 (1.8 kWh/kg)	9 (3 kWh/kg)	7.5 (2.5 kWh/kg)
System Volumetric Density (g/L)	28 (0.9 kWh/L)	45 (1.5 kWh/L)	40 (1.3 kWh/L)	81 (2.7 kWh/L)	70 (2.3 kWh/L)
System Fill Time for 5-kg fill, min (Fueling Rate, kg/min)	4.2 min (1.2 kg/min)	3 min (1.67 kg/min)	3.3 min (1.5 kg/min)	2.5 min (2.0 kg/min)	2.5 min (2.0 kg/min)
Storage System Cost ($/kg H2): To be determined in conjunction with other Partnership cost target chances	TBD	133 ($4/kWh)	TBD	67 ($2/kWh)	TBD

According to Ren, Musyoka, Langmi, Swartbooi, North, and Mathe (2015), Zhao *et al.* (2016) and Sethia and Sayari (2016), hydrogen can be stored through the common compression and liquefaction method or even through the use of various materials by physically bonding its gas molecules to the surface of a solid or liquid (physisorption) material or chemically bonding the adsorbate (hydrogen) molecules to the specific surface locations/active sites on the material (chemisorption). However, none of these storage methods can satisfy the US government's legislated storage requirements at 77K (Zhao *et al.* 2017). We need a more practical and cost-effective means to store hydrogen. For this reason, this research seeks to find the most practical hydrogen storage methods, one of which is using bio-waste-activated carbons.

Three important technology hinderances to the hydrogen economy:

1. Reducing the cost of hydrogen, i.e., production, delivery, and storage costs, to make hydrogen competitive with conventional fuels
2. Reducing fuel cell cost and enhancing its durability to make it competitive with conventional technologies
3. Improving hydrogen storage to meet DOE targets

2.4 Hydrogen Storage Methods

2.4.1 Compression Method of Hydrogen Storage

Compression of hydrogen at high pressure is the most common method of hydrogen storage (Zhang *et al.*, 2016). This well-developed method presents opportunities for high hydrogen filling and release (Durbin and Malardier-Jugroot, 2013; Abe *et al.*, 2019). Hydrogen compression to higher pressures consumes a fraction, about 13-18%, of hydrogen's lower heating value, which adds costs. On the other side, a notable positive aspect of this process is that no energy is used for hydrogen release. Increasing the storage pressure only increases the power required for hydrogen compression by a small relative amount. Compressed hydrogen is stored in cylindrical storage devices because circular or spherical storage devices are challenging to fit onboard.

To achieve hydrogen storage by compression, the storage device's construction material should be light, affordable, able to withstand high pressures and prevent hydrogen diffusion and loss of its ductility (hydrogen embrittlement). Four types of hydrogen gas storage by compression technologies or materials have been developed to accommodate these requirements. Type-I materials are the most affordable. These storage devices are made up of metallic materials that can withstand up to 30 bar pressure; aluminum and steel alloys are common construction materials (Usman, 2022). Thicker walls must be used for higher hydrogen pressures or densities, making the device heavier and reducing the total hydrogen gravimetric energy density (Moradi and Groth, 2019). This means less hydrogen is stored in type-I devices (Abdalla *et al.*, 2018; Usman, 2022).

Type-II hydrogen storage by compression technologies is steel pressure vessels with a glass fiber composite overwrap (Moradi and Groth, 2019; Usman, 2022). The structural load is roughly equally distributed between the steel and composite materials. Type-II vessels are 50% more

expensive to manufacture than type-I vessels but 30-40% less heavy (Moradi and Groth, 2019). They also have the highest-pressure tolerance. Type III pressure vessels are full composite wraps with metal liners. They are made of carbon fiber composite materials lined with metal, the carbon fiber composite taking most of the structural load and the liner used for sealing and contributing more than 5% mechanical strength (Usman, 2022). These are half the weight of type-II vessels, but their manufacturing costs are twice that of type-II vessels. They are strong and lightweight but have low thermal conductivity because the composite material takes most of the structural load. This low thermal conductivity is a problem for low heat release rates during hydrogen compression. They are mostly useful for pressure requirements of 450 bar but can also be used for higher pressures up to 700 bar.

Type-IV technology vessels are fully composite. Carbon fiber or carbon glass composite carries the most structural load with polymers like high-density polyethylene (HDPE) for lining (Moradi and Groth, 2019). These vessels are the lightest but most expensive. They are used to store hydrogen at 700 bar and can withstand as much as 1000 bar pressure. A pre-commercial, so-called type-V vessel is also in development. This enhances type-IV vessels with reinforcing space to occupy the skeleton for better volumetric and gravimetric hydrogen densities (Usman, 2022).

Hydrogen storage by compression is an old technology that increases the energy density of gaseous hydrogen by storing it at high pressures (Zhao, 2012). According to Møller *et al.* (2017), storing hydrogen at 700 bar in type III or IV vessels is perhaps the most pragmatic solution to refueling in less than 3 minutes and having enough hydrogen for a 500 km drive. Hydrogen has an energy density of 5.7 MJ/L at 700 bar with a type-IV vessel. There is a risk with onboard pressurised vessels as they can explode.

A number of fuel cell vehicles operating on compressed hydrogen, such as the 2018 Hyundai Nexo and the 2021 Toyota Mirai, are in use (Usman, 2022). These cars have three type-IV cylinders and use compressed hydrogen at 700 bar. They can go for over 600 km without recharging (Usman, 2022). An example of a carbon fiber-reinforced 350-bar and 700-bar compressed hydrogen gas tank is shown in Figure 2.7.

Figure 2.7 Carbon fiber-reinforced 350 bar and 700 bar compressed hydrogen gas tank (Zhao, 2012)

2.4.2 Liquefaction Method of Hydrogen Storage

Storing hydrogen in the liquid state also increases its energy density. This makes the liquid hydrogen denser than the gaseous hydrogen, thus having higher energy content per unit volume than the same unit of gaseous volume. According to Zhao (2012), gaseous hydrogen has a volumetric capacity of 0.030 kg/L at 700 bar. In contrast, liquid hydrogen's volumetric capacity is 0.070 kg/L, more than twice the gaseous one.

According to Usman (2022), liquid hydrogen's density is around 71 g/L at -253 ℃, and its energy density is 8 MJ/L hydrogen. This means that four cylinders of liquid hydrogen are equivalent to one gasoline tank. The critical temperature of hydrogen is -240 ℃, and its normal boiling point temperature is -253 ℃. Hydrogen cannot be liquefied above -240 ℃. It is cooled below its critical temperature to its normal boiling point temperature to be stored as a liquid. Liquefaction of hydrogen, similar to compression, is also a common technology. Liquefied hydrogen gives high hydrogen release rates and low adiabatic expansion energy under cryogenic conditions (Usman, 2022). The low adiabatic expansion energy helps to prevent damage in the case of hydrogen leaking through an opening.

The density of liquefied hydrogen is 1.5 to 2 times higher than that of hydrogen compressed at high pressure, making the size of the storage tank required much smaller and acceptable (Usman, 2022). Hydrogen storage can also be achieved at low pressures, meaning thinner and cheaper storage vessels/tanks can be used. Hydrogen is non-corrosive in the liquid state, so stainless steel

and aluminum alloy vessels that are well insulated are used to store hydrogen in cryogenic conditions.

Liquefaction is expensive, and the energy used to liquefy hydrogen is also expensive. About 30-40% of the net heating value of hydrogen is used in the liquefaction process (Usman, 2022). The boil-off phenomenon, the loss of hydrogen due to energy addition from the surroundings, is another challenge of this liquefaction process, with an estimated 1.5-3% daily evaporation of hydrogen. More open spaces for public parking and garages are necessary because of the boil-off phenomenon. To reduce boil-off, a double-walled vacuum vessel with massive, pricey insulation can be used (Usman, 2022). Another technique to minimize evaporation is having a large vessel with a smaller surface-to-volume ratio. The added insulation and unique design can lead to a heavier vessel and thus reduce its gravimetric energy density. The infrastructure needed for liquid hydrogen is still an issue.

Due to low temperatures and boil-off, there is little opportunity for liquid hydrogen to be used for onboard applications in small and medium-sized vehicles. BMW developed a test vehicle, the BMW Hydrogen 7, in 2005-2007, which burns hydrogen in its internal combustion engine. GM/Opel also developed a test vehicle, the GM Hydrogen 3, in 2006, which uses hydrogen in a series of fuel cells. There is doubt over this technology's future use and expansion in vehicles. Liquefied hydrogen is, however, used in space crafts where costs are not an issue and recently in a 112 m long yacht developed by Sinot (Usman, 2022). The yacht, Aqua, runs on liquid hydrogen.

Linde Engineering (2021) anticipates a surge in the demand for liquid hydrogen in the forthcoming years. The company asserts that only three liquefaction plants in Europe can cool hydrogen to -253 ℃.

2.4.3 Hydrogen Storage on (carbon-based) Adsorbents

Hydrogen is also stored using carbon-based adsorbents. This is usually achieved by absorption into the solid materials or by adsorption on the surface of the solid. Carbon is the sixth element of the periodic table, atomic number 6. It is non-metallic and tetravalent, with four electrons available to form covalent chemical bonds. Carbon has the unique ability to bond with itself through sp^2

(diamond-like) or sp^3 (graphite-like) hybridisation (Edwards *et al.*, 2013). A number of resulting structures or allotropes are possible. However, only a few, those consisting mainly of graphitic subunits, are usually studied in carbon science. The structural organisation is classified into two extremes, the graphitisable and non-graphitisable carbons. The graphitisable ones, cokes, are produced from carbonaceous precursors, which pass through a liquid phase on pyrolysis. In contrast, the non-graphitisable chars are produced from those carbonaceous precursors that do not fuse (Edwards *et al.*, 2013).

Three common carbon allotropes are studied: diamond, graphitic, and non-graphitic carbons. Figure 2.8 shows some of these allotropes. Diamond is hard, has an enormously high refractive index and high dispersion of light, and has a regular three-dimensional network of σ-bonds, which lead to rigid and isotropic structures (Zhao, 2012; Edwards *et al.*, 2013). These are the aliphatic types. Graphite is composed of the σ-bond and π-bond bonding regimes, which lead to aromatic types where most of the structures are layered and highly anisotropic (Edwards *et al.*, 2013). Van der Waals forces hold graphitic layers together, and graphite exists naturally or can be made artificially by heating petroleum coke or coal at high temperatures (Zhao, 2012). Non-graphitic or amorphous carbon materials are further subcategorized into carbon blacks, coke, char, and activated carbons (Zhao, 2012).

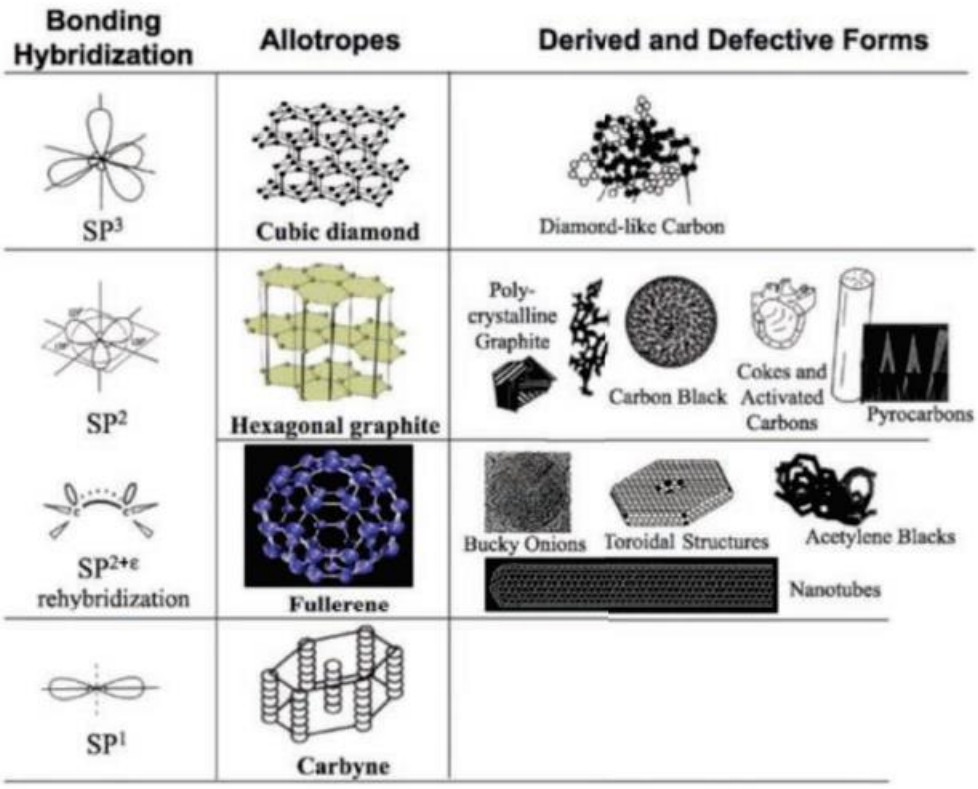

Figure 2.8 Carbon allotropes (Zhao, 2012)

An ideal hydrogen storage solid should have slit-shaped nanopores and a width more than the kinetic diameter of hydrogen, 2.89 Å (Chambers *et al.*, 1998).

2.4.3.1 Single and Multiwalled Carbon Nanotubes

Carbon nanotubes are sp^2 nanocarbon materials of pipe-like structures made of rolled-up graphene sheets (Thomas *et al.*, 2021). They have unique nanostructures and possess incredible properties derived from their graphite nature and one-dimensional aspect (Thomas *et al.*, 2021). They can either be metals or semiconductors, depending on their chirality. Metallic carbon nanotubes can carry an electric current density of over 1000 times that of most metals like copper. Their one-dimensional conductivity gives them their ballistic transport behaviour along the tube, which promotes massive mobility, much higher than observed for most conductors. They reportedly have higher mechanical tensile strength than steel and better thermal conductivity than diamond (Thomas *et al.*, 2021). They also have a high aspect ratio, even higher than 1000, and a surface area larger than 1300 m^2/g. Carbon nanotubes are light, with an average density of about a sixth

of the density of steel. They are also highly chemically stable and do not undergo any chemical alteration unless in high temperature and oxygen (Thomas *et al.*, 2021).

A multiwalled carbon nanotube (MWCNT), as shown in Figure 2.9(a), is made up of concentric cylinders with an interlayer spacing of 3.4 Å and diameters commonly around the 10-20 nm range (Dai, 2002). A single-wall carbon nanotube (SWCNT), shown in Figure 2.9(b), is a graphene sheet rolled over into a cylinder with a diameter commonly around 1.4 nm region (Dai, 2002).

Hydrogen storage in carbon nanotubes is one of the safest ways to store hydrogen as hydrogen interacts with the nanotubes through physisorption or chemisorption. Every carbon atom can be used as a site for the chemisorption of hydrogen atoms, with dissociative chemisorption being the favourable method for carbon nanotubes (Thomas *et al.*, 2021). The hydrogen molecule breaks into two atoms at high pressure, making it possible for the C-H bonds to form, thus leading to the dissociative adsorption of hydrogen. This hydrogen is stored in a number of sites: inside the tubes, outside the tubes, between the tubes, and between shells for MWCNTs. The carbon nanotubes' structure, pretreatment process, geometry, structural defects, operating pressure, and temperature dictate their hydrogen storage capacity (Thomas *et al.*, 2021). Experimental work has achieved a 10 wt% maximum hydrogen storage capacity for SWCNTs. A Monte Carlo simulation predicted 11.2 wt% and higher hydrogen storage capacities of up to 20 wt% and 14 wt%, respectively, are achievable through lithium and potassium doping of MWCNTs (Thomas *et al.*, 2021).

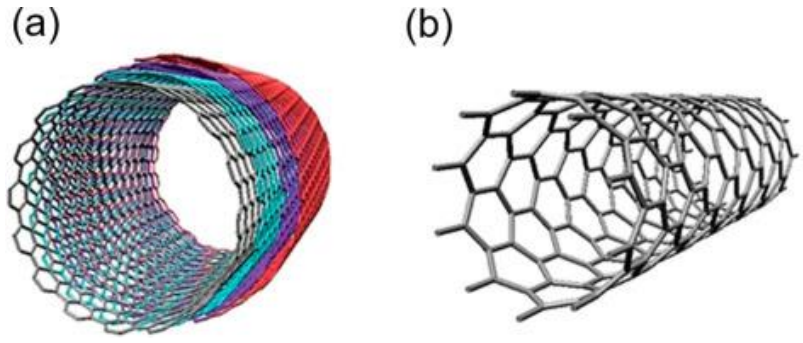

Figure 2.9 Schematic of (a) MWCNT and (b) SWCNT (Thomas *et al.*, 2021)

Other applications of carbon nanotubes are in photocatalytic and catalytic reactions, as adsorbents or extraction agents and membranes, in fuel cells, in solar cells and sensors, in batteries and

supercapacitors, in conductive films, coating, textiles, fabrics, and biomedical uses (Thomas *et al.*, 2021).

2.4.3.2 Nanofibres (Graphite Nanofibres)

Graphite nanofibers are usually between 10 and 100 μm, have cross-sectional areas between 30 and 500 $Å^2$ and were usually produced through catalytic decomposition of carbon-containing gases and their mixtures on surfaces of metals and alloys at 450-750 ℃ (Chambers *et al.*, 1998). These are fibrous solids containing graphite platelets stacked parallel to the precipitating faces of the metal particle, as shown in figure 2.10 (Chambers *et al.*, 1998; Zhao, 2012). Other nanofibers whose platelets have perpendicular or angular arrangements have also been produced by Chambers *et al.* (1998). These layers are separated at distances influenced by the catalyst, gas phase, and reaction conditions. The minimum distance observed is that of single-crystal graphite at 3.35 Å, greater than the hydrogen kinetic diameter (2.89 Å), rendering these nanofibers useful for hydrogen sorption.

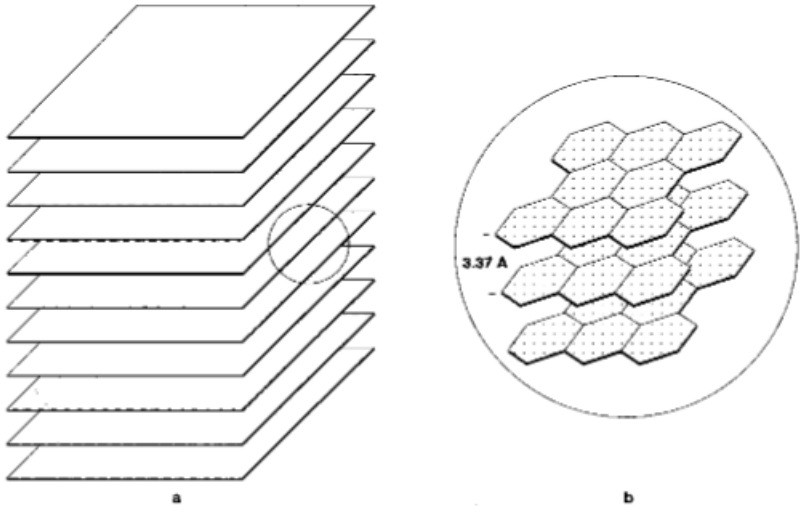

Figure 2.10 (a) Schematic representation of the arrangement of platelets in a catalytically grown graphite nanofiber; (b) an enlarged section showing the detail of the area marked in (a) (Chambers *et al.*, 1998)

Alkali-intercalated graphite was reported to adsorb about 0.137 L of hydrogen per gram of carbon at STP between its layers, with no structural damage after multiple adsorption and desorption

cycles at liquid nitrogen temperature (Chambers *et al.*, 1998). Hydrogen chemisorbed on graphite exhibits a symmetrical $\sqrt{3} \times \sqrt{3}$ superstructure at submonolayer coverage, with an incommensurate triangular phase being prevalent at near monolayer coverage (Chambers *et al.*, 1998). Furthermore, Chambers *et al.* (1998) found that the graphite material they analysed could sorb and retain more than 20 L of hydrogen per gram of carbon when the nanofibers were exposed to hydrogen at 120 atm and 25 °C. This sorption and retention were further eased by the short diffusion path and the weak van der Waals bonding of the platelets that allowed them to sorb hydrogen in multilayer configurations. Releasing the stored hydrogen at room temperature was also easy when the pressure was reduced.

Through electrospinning, Bai *et al.* (2011) synthesised polyacrylonitrile-based carbon nanofibers containing titanium and manganese. Maximum hydrogen storage capacities observed at 303 K and 9 MPa for the Ti and Mn-containing nanofibers were 1.6 and 1.1 wt%, respectively (Bai *et al.*, 2011). Chen *et al.* (2004) reported a hydrogen storage capacity of 1.0 wt% for the partially aligned carbon nanotubes they produced through catalytic decomposition of methane at the surface of water containing oxidized and reduced products of $LaNi_5$ alloy with Ni powder.

2.4.3.3 Graphite and Graphene

Graphene, a 2D crystalline carbon form, is the building block for carbon allotropes such as fullerenes, carbon nanotubes, and graphite (Aliofkhazraei, 2013; Novoselov, 2011). Its carbon atoms are arranged in a planar honeycomb network. A monolayer graphene unit cell is made up of 1.42 Å apart from two carbon atoms with a lattice constant of 2.46 Å (Aliofkhazraei, 2013). Each atom has s, $p_{x,}$ and p_y orbitals and is bonded to three other atoms in the lattice, thus creating the sp^2 atomic network (Aliofkhazraei, 2013). Graphene has an increased binding energy of physisorbed hydrogen, which makes it more advantageous than other carbon materials (Jain and Kandasubramanian, 2020). Graphene is a zero-overlap semimetal whose charge carriers have a linear dispersion relation near the Dirac point (Novoselov, 2011). Figure 2.11 shows the structures of graphene and graphite, and Figure 2.12 shows the energy per atom for the graphene-hydrogen system.

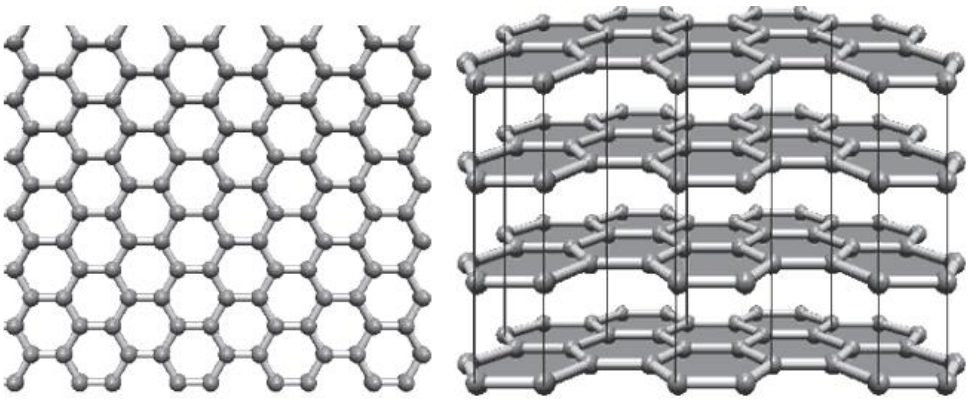

Figure 2.11 Schematic of structures of graphene (left) and graphite (right) (Zhao, 2012)

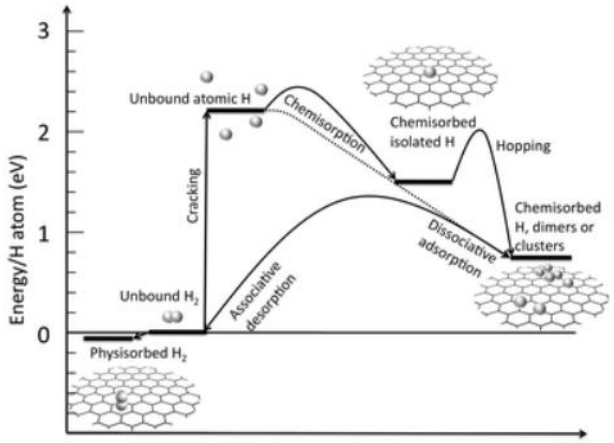

Figure 2.12 energy level diagram for the graphene-hydrogen system (Tozzini and Pellegrini, 2013)

Graphene sheets are light, robust, chemically, and thermally stable. They show incredibly high strength (130 GPa tensile strength), great conductivity (15,000 $cm^2\ V^{-1}\ s^{-1}$), large surface area (2630 m^2/g), biocompatibility, flexibility, and are transparent (Jain and Kandasubramanian, 2020). Graphene can potentially replace silicon-based computer chips, enhance touchscreen performance, create more sensitive biometric sensors, even faster charging, and improve storage in batteries and capacitors (Delgass, 2023). Their excellent properties make them suitable for photonics, gas separation, water treatment, and many other applications (Jain and Kandasubramanian, 2020).

The experimental data of the pure graphene sheet shows a low hydrogen adsorption capacity of about 1 wt% at ambient temperature. However, it exhibits good interaction with other functional

groups that can enhance its adsorption capacity, refer to Table 2.3. Graphene and graphite can potentially be used in hydrogen storage applications (Zhao, 2012).

Table 2.3 Functionalized graphene material with experimental gravimetric capacities (Jain and Kandasubramanian, 2020; Tozzini and Pellegrini, 2013).

Functionalized graphene material	**H2 wt% T (K) /P (bar)**
Graphene nanosheets	1.2 wt% 77 IC/10 bar [Zhao *et al.*, 2011a]
Hierarchical graphene	4.01 wt% 77 K/1.07 bar [Zhao *et al.*, 2011a]
Graphene functionalized with chlorosulphuric acid	1.6 wt% 77 K/2 bar [Zhao *et al.*, 2013]
Graphene functionalized with oleum	1.4 wt% 77 K/2 bar [Zhao *et al.*, 2013]
Graphene oxide	1.4 wt% 298 K/50 bar [Jain and Kandasubramanian, 2020; Tozzini and Pellegrini, 2013]
Graphene oxide -I- MWCNT	2.6 wt% 298 K/50 bar [Jain and Kandasubramanian, 2020; Tozzini and Pellegrini, 2013]
Graphene -I- MWCNT	2.1 wt% 298 K/50 bar [Jain and Kandasubramanian, 2020; Tozzini and Pellegrini, 2013]
Pt-fimctionalized graphene	0.15 wt% 303 K/57 bar [Jain and Kandasubramanian, 2020; Tozzini and Pellegrini, 2013]
Pd-functionalized graphene	0.81 wt% 298 K/40 bar [Iijima, 1991]
Ni (0.83 wt%) and B (1.09 w0/0) doped graphene	4.4 wt% 77 IC/1.06 bar [Dillon, 1996]
N-doped palladium-decorated graphene	2.10 wt% 298 K/20 bar [Jain and Kandasubramanian, 2020; Tozzini and Pellegrini, 2013]
Reduced graphene oxide—Mg nanocomposite	6.5 wt% 473 K/15 bar [Dillon *et al.*, 2002]
Cu-BTC with 9 wt% graphene	3.58 wt% 77 K/43 atm [Marco-Lozar *et al.*, 2012]

2.4.3.4 Activated Carbons

Activated carbons are processed carbons with graphite, crystalline, and amorphous carbon (Mohan *et al.*, 2019). They usually have high surface areas, over 3000 m^2/g, and very small pore diameters, less than 1 nm. They are often produced by dry distillation from carbonaceous materials whose pore volume can be increased by thermal or chemical activation (Mohan *et al.*, 2019). Their hydrogen adsorption capacity depends mainly on their specific surface area and pore volume. Activated carbons are synthesised through the physical or chemical activation of natural materials such as coal, wood, peat, etc. Similar to other carbon materials, ACs have low mass density, and weak van der Waal's forces facilitate the physisorption of hydrogen molecules into the pores of

the ACs through adsorption and diffusion (Zhao, 2012; Mohan *et al.*, 2019). Commercial activated carbons are used for gas or liquid applications (Zhao, 2012).

2.4.4 Current Hydrogen Storage Methods

The preceding sections highlight each hydrogen storage method's inherent advantages and drawbacks. Table 2.4 provides a comparative analysis of various carbon materials, detailing their respective precursors or synthesis processes and their corresponding hydrogen storage capacities.

Despite the potential of the hydrogen economy with its positive indications of sustainable, clean, and highly efficient energy, this study highlights the challenges associated with the expensive production and storage of hydrogen. This is attributed to hydrogen's absence in its elemental form and notably low gravimetric density. Consequently, any developed hydrogen storage method or technology aiming for the commercial and competitive realization of the hydrogen economy must prioritize cost minimization and ease of manufacturing.

Table 2.4: Comparison of different carbon materials (Mohan *et al.*, 2019)

Materials	Precursor/synthesis process	Storage capacity
Activated carbon	Reaction of cokes with (KOH)	2 wt%
Activated carbon	Chemically treated and pyrolysis (973 K)	5.5 wt% at 77 K and low pressures
Graphite nanofiber	Thermal decomposition of acetylene using palladium (Pd) sheets as catalyst	17 wt% at 300 K and 8.1 MPa
Activated carbon	Sucrose as carbon precursor and ammonium-form zeolite-Y as template, impregnation, and chemical vapor deposition	2.4 wt% at 77 K and 10 bar.
Activated carbon	Anthracite of Taisi mine and Pd-doped	53 wt% at 298 K, S MPa
AC (Pt-doped)	Chemically impregnated with 5M nitric acid, chemical reduction method	2.3 wt%
Graphite (Fe-doped)	Ball-milled	3.9 wt%
Graphite (Ni-doped)	Ball-milled	0.92 wt%
Graphite (Cu-doped)	Ball-milled	0.97 wt%
Graphite (Co-doped)	Ball-milled	1.8 wt%

Ni-doped porous graphite	Acid treatment of graphite flakes, metal nanoparticle deposition	4.48 wt% at 298 K, 10 MPa
Al-doped bulk graphite	Density function theory	3.48 wt% at 300 K, 100 MPa
G (Li-doped)	Monte Carlo simulations	6.5 wt%, 298 K, 2 MPa
MWCNT	Microwave plasma-enhanced chemical vapor deposition	1.97 wt% at room temp.
GNP	Reactive ball-milling	0.5 wt%
SWNT	Reactive ball-milling	1 wt%
SWNT	Semi-continuous hydrogen arc discharge method	4.2 wt%, 298 K, 12 MPa
Well-aligned MWCNT	Catalytic pyrolysis of carbon source with quartz glass as substrate	3 wt% at 290 K, 10 MPa

2.5 Hydrogen Storage in Activated Carbons

2.5.1 Activated Carbons

An activated carbon is a processed carbon that is highly porous with a large surface area (Zhao, 2012). Activated carbons are often prepared from materials with high carbon content and low composition of inorganic material. Examples of these include coal, turf/peat, polymeric materials, wood, bamboo, and various agricultural by-products (Zhao, Fan, Gao and Wang 2016; Fierro, Szczurek, Zlotea, Marêché, Izquierdo, Albiniak, Latroche, Furdin and Celzard 2010; Fierro, Zhao, Izquierdo, Aylon and Celzard 2010). They are stable and can be used in large-scale production as they also have fast kinetics (Zhao, Luo, Wang, and Fan 2017). These can also be used in stationary applications, where their weight and volume do not pose issues to the application (Zhao *et al*. 2017).

Activation refers to the process that follows the pyrolysis of the carbonaceous material at high temperatures, often between 500 ℃ and 1000 ℃. Activation of carbon can be physical or chemical. Physical activation usually occurs when the carbon is partially gasified by reacting it with steam, CO_2, or air. The majority of amorphous parts usually burn-off (Zhao, 2012). Chemical activation, on the other hand, is usually characterized by heat treatment of the carbonaceous material with chemical reagents such as alkali material (KOH, NaOH), inorganic acids (H_2SO_4, H_3PO_4), or salts ($ZnCl_2$) in an inert atmosphere between 600 ℃ and 800 ℃ (Zhao, 2012). Chemical activation results in more homogeneous pore structures and is single-stage, whereas physical activation results in varied pore structures and is multi-stage, often preceded by pyrolysis of the material.

Activated carbon is structurally similar to graphite but with larger interlayer spacing and rotated carbons (Thomas *et al.*, 2021).

2.5.1.1 Precursors and Hydrothermal Treatment of Precursors

The raw material for activated carbon production can be any material that contains a high concentration of carbon with low composition of inorganic material. Most industrial activated carbon production processes have their feedstock or precursors as fresh or old biomass. This is usually because these feed materials are cheap and highly carbonaceous. The feed determines the properties of the resulting activated carbons. The activated carbon's performance, surface area, total pore volume, and pore size distribution are all unique for different feed materials.

Over the past decade, products derived from biomass waste have seen profitable daily applications. Waste hazelnut shell was recently used as the precursor to produce highly porous carbonaceous carbon dioxide sorbents (Pang *et al.*, 2020; Serafin *et al.*, 2019). Lotus stalk produced porous carbons with excellent carbon dioxide adsorption, great recyclability, and fast adsorption kinetics. The carbon product electrode demonstrated significant specific capacitance and stability of about 95% retention rate after 5000 cycles, making these biomass-derived products suitable for applications as supercapacitors, too (Li *et al.*, 2021; Serafin *et al.*, 2019).

Activated carbons from biomass waste have been widely studied as hydrogen storage material. They continue to present themselves as good candidates for supercapacitor applications (Sevilla and Mokaya, 2014). In 2021, Ariharan *et al.* (2021) further demonstrated through simple carbonisation that biomass-derived porous carbon is a superior material for both hydrogen storage and supercapacitor usage (Ariharan *et al.*, 2021). Carbon products from biomass pine nutshells showed ultrahigh specific surface area, large pore volume, and "excellent electrochemical performance as supercapacitors" (Lv *et al.*, 2018). These materials' highly developed porous structure makes them attractive for these applications.

Wet biomass has moisture content greater than 30 wt% and dry biomass less than 30 wt%. The biomass conversion technology of choice is based on this classification (Masoumi *et al.*, 2021). Combustion, pyrolysis, and hydrothermal biomass processing lead to different char products, with

pyrolysis and hydrothermal carbonisation producing mainly bio/hydrochars. These processes enhance the organic compounds containing biomass to carbon-rich chars (Lucian *et al.*, 2018). Pyrolysis can occur in three main ways: slow, fast, and pyrolytic gasification and hydrothermal processing of biomass can also occur in three different ways – hydrothermal carbonisation, hydrothermal liquefaction, and hydrothermal gasification – but producing different char products. Hydrothermal carbonisation eliminates the drying stage and has been recorded as the most economical of these processes (Rowlandson, 2018). Thus, it is regarded as the best performing technology for biomass processing and scaling (Hoekman *et al.*, 2013; Cheng and Li, 2018). For these reasons, the HTC process was chosen for pre-treating the avocado waste.

A Berghof stirred pressure reactor, whose contents were stirred at 250 rpm, was used to convert the biomass to hydrochar. The biomass-to-water ratio was kept at 0.125, the reaction temperature varied between 180 ℃ and 240 ℃, and the retention time varied from 2 to 8 hours. These are the optimised conditions, as reported in the literature (Masoumi *et al.*, 2021). The products were cooled; solid and aqueous solutions were dried and stored for analysis.

2.5.1.2 Physical Activation

Physical activation improves the porosity of carbonaceous feedstock through controlled gasification. In physical activation, the carbon precursor is first pyrolyzed in an inert environment at 400-900 ℃ to remove most of the more volatile matter, then partially gasified at 350-1000 ℃ using an oxidizing gas (Sevilla and Mokaya, 2014). In the first step, the active oxygen in the activating agent combusts the tarry pyrolysis off-products trapped in the pores, opening up these pores. As the oxidizing agent burns more of the reactive carbon skeleton, micropores form, and the reaction of the oxidizing agent with the carbon produces CO and CO_2, with the degree of burn-off being determined by the gas used as well as the activation temperature (Sevilla and Mokaya, 2014). Activating agents commonly used are CO_2, air, and steam.

The physical and chemical properties of the resulting physically activated carbon depend on the precursor, the oxidizing agent used, the activation temperature, and the degree of activation (Sevilla and Mokaya, 2014). These factors combined produce activated carbons with moderate to high porosity and varying surface chemistry. Generally, larger porosity is observed for instances

with high activation temperature or activation time and lower porosity for lower activation temperature or shorter activation time. Wider pore size distributions also follow higher porosity.

The reaction of carbon with oxygen is exothermic, so many challenges are experienced when air or oxygen is used as the activating agent. The reaction happens very fast and results in excessive burn-off and lower yield of the activated carbon (Sevilla and Mokaya, 2014). The upside of this is that the high reactivity of oxygen reduces the activation energy requirements, thus being cheaper than when carbon dioxide steam is used.

Feng and Bathia (2003) noticed that the surface area and pore volume increase initially and slowly as carbon converts into air gasification. The surface area and pore volume change for small micropores are not very pronounced with carbon conversion after some point. In contrast, the change for mesopores was proportional to the conversion, increasing with the conversion. In CO_2 gasification, they noted a rapid increase in surface area and pore volume for micropores and other pore sizes as gasification progressed. Air gasification achieved better surface areas and pore volumes than CO_2 gasification (Feng and Bathia, 2003).

Osswald *et al.* (2009) noticed an increase in surface area and pore volume with an increase in activation time and temperature in air gasification. This was about a 10% increase, followed by massive weight loss. Oxygen's reactivity also made the micropores into mesopores. In CO_2 gasification, they observed up to 77% surface area increase and close to doubling the pore volume, achieving a surface area of 3100 m^2/g and pore volume of 1.3–1.4 cm^3/g at 950 °C for 2 h.

As discussed above, it is not a coincidence that steam and carbon dioxide are the preferred activating agents instead of air. Steam is generally seen as more reactive than CO_2, thus requiring lower activation temperatures.

2.5.1.3 Chemical Activation

In chemical activation, the carbon precursor and activating agent mixture is treated in heat at temperatures of 450–900 °C. Compared to physical activation, chemical activation has the

following advantages: (i) it often involves only one step, (ii) it uses lower pyrolysis temperatures, (iii) it yields more carbon than physical activation, (iv) it produces materials with much higher surface areas and (v) the resulting microporosity can be well developed and modified to be somewhat uniform (Sevilla and Mokaya, 2014). Higher surface areas and well developed microporosity are crucial for gas storage applications of the synthesised carbon.

A number of chemical reagents are used in chemical activation. These include alkalis (NaOH, KOH), salts ($ZnCl_2$, $AlCl_3$, $MgCl_2$), inorganic acids (H_3PO_4, H_2SO_4), and many more. Zinc chloride, $ZnCl_2$, phosphoric acid, H_3PO_4, and potassium hydroxide are the most commonly used chemical activation reagents (Sevilla and Mokaya, 2014). KOH acts as an oxidant, whereas $ZnCl_2$ and H_3PO_4 act as dehydrating agents. When the carbon precursor is heated, the activating agent in its particles creates a dehydration effect where cross-linking reactions such as cyclisation and condensation dominate. This dehydration process makes the carbon precursor particles smaller but not more than the size of the activating agent, which remains inside its particles, thus somewhat limiting the microscopy of the carbon precursor to its size.

Additionally, the combination of H3PO4 with organic compounds in the carbon precursor leads to the formation of phosphate and polyphosphate bridges, which connect fragments of biopolymers. This process contributes to the reduction of contraction in the carbon precursor as the activation temperature rises. Consequently, the resulting micropores are heterogeneous in nature due to the presence of a mixture of phosphorous molecules, rather than solely phosphoric acid (Sevilla and Mokaya, 2014). In contrast, zinc chloride or its hydrates are small and produce more small, homogeneous micropores (Molina-Sabio and Rodrıguez-Reinoso, 2004).

KOH and NaOH act as oxidants. A redox reaction occurs, which etches the carbon structure to create pores due to carbon oxidation into carbon ions and the intercalation of potassium compounds, which are removed through washing steps later on. K_2CO_3 decomposition at more than 700 °C can also improve the microporosity of the carbon material through carbon gasification (Teng and Hsu, 1999). It is well observed that the more reactive the carbon precursor is, the lower the temperature required to start gasification and the higher the degree of gasification due to CO_2

released from K_2CO_3, thus producing highly developed pores (Teng and Hsu, 1999; Guan *et al.*, 2009; Bleda-Martínez *et al.*, 2005).

In general, increasing the quantity of activating agent used yields enhanced surface area and pore volume, but with the trade-off of a broader range of pore size distribution (PSD). The initial assessment of porosity growth is conducted using microscopy. However, as the concentration of the activation agent increases, the distribution of pore sizes becomes more varied. The overall porosity achieved is contingent upon the specific activating agent selected. In their study on the influence of chemical activation on carbon porosity, Molina-Sabio and Rodrıguez-Reinoso (2004) observed that the activation of peach stone using KOH resulted in the formation of broader microporosity characterized by a greater degree of heterogeneity in micropore inclination. Conversely, $ZnCl_2$ activation led to the development of both wide micropores and narrow mesopores, while H_3PO_4 activation resulted in the formation of larger mesopores and macropores (Sevilla and Mokaya, 2014).

The development of porosity is subject to a temperature limit. The determination of the optimum temperature is contingent upon the choice of carbon precursor and activating agent. It may be stated that the growth of porosity is enhanced with increasing activation temperature, up until the maximum temperature allowable for the carbon precursor and activating agent. The growth of porosity is diminished when the temperature exceeds a certain threshold, as a result of the carbon structure undergoing collapse (Teng and Hsu, 1999; Suárez-Garcıa *et al.*, 2002; Hsu and Teng, 2000). According to Sevilla and Mokaya (2014), when chemical activation is performed using $ZnCl_2$ or H_3PO_4 at temperatures over 500 °C, it results in a reduction in weight and the deterioration of the carbon structure, leading to a decrease in microporosity. This observation provides additional evidence indicating that the cross-links generated at lower temperatures lack sufficient thermal stability. The structural integrity of the material deteriorates as a result of the rearrangement of carbon fragments, leading to the collapse of the carbon framework when the pores undergo shrinkage. Sevilla and Mokaya (2014) have demonstrated that the optimal temperature range for achieving maximum porosity in KOH is between 700 °C and 900 °C. This implies that the cross-links generated by KOH activation exhibit greater thermal stability compared to those induced by $ZnCl_2$ or H_3PO_4 activation. Yet again, it is seen that when temperature increases, there is a wider variety of pore sizes associated with the formation of

increased porosity. In addition, numerous works have proven that the carbonisation temperature does not significantly impact the distribution of pore sizes in carbon precursors that are activated using either $ZnCl_2$ or H_3PO_4. On the other hand, the pore size distribution of the carbon precursor activated with KOH is notably influenced by temperature, as demonstrated in studies conducted by Hsu and Teng (2000) and Sevilla and Mokaya (2014).

Between 500 and 700 °C, micropores form primarily due to the liberation of volatile matter for KOH activation, but CO_2 released from K_2CO_3, formed during carbonisation, increases, and carbon gasification increases which opens up closed pores and further widen existing micropores, hence a broader PSD (Sevilla and Mokaya, 2014). The metallic potassium formed further intercalates between the structure. It widens the spaces between the carbon atomic layer, thus increasing the pore volume (Sevilla and Mokaya, 2014).

According to Sevilla and Mokaya (2014), porosity development is also affected by (i) the mixing procedure, activation time, the gas flow rate, the type of gas used during heat treatment, and the heating rate.

KOH redox reaction:

$$6KOH + 2C \leftrightarrow 2K + 3H_2 + 2K_2CO_3 \quad (2.4)$$

Another common KOH reaction mechanism is:

$$4KOH + C \rightarrow K_2CO_3 + K_2O + 2H_2 \quad (2.5)$$

The weight ratio of the activating agent to the carbon precursor affects the porosity of the carbon material. Zhao (2012) states that the weight ratio is the most important parameter in KOH chemical activation processes. A higher weight ratio resulted in better nitrogen adsorption in the carbon material. Micropore volume and surface area increased with increasing weight ratio until the optimum weight ratio was reached. The weight ratio also affects the pore size distribution.

The flow rate of the inert gas used during activation. Higher flow rates of the inert gas used during KOH chemical activation increased the adsorption capacities of the resulting activated carbons and enhanced their micropore volumes (Lozano-Castello *et al.*, 2001; Zhao, 2012). Beyond the

optimum gas flow rate, the efficiency of the activation process was reduced, and carbon with a lower surface area and less microporosity was produced (Lozano-Castello *et al.*, 2001). Steam is also reportedly a good environment for activation, either by itself or combined with nitrogen. However, it is not better than pure hydrogen. The inert gas's flow rate has less of an impact in comparison to the temperature and weight ratio. The gas flow rate should not be too high that the gas blows away the reagents or products.

The heating rate during the heat treatment process is another factor influencing the microporosity of the carbon product. Lower heating rates produce higher micropore volumes of activated carbons (Lozano-Castello *et al.*, 2001). This is partly due to the melting point of KOH being 406 °C, meaning that better contact is achieved between carbon and the molten KOH before reaching the reaction temperature (Zhao, 2012). As detailed above, surface oxygen complexes liberated during KOH activation further promote carbon gasification, enhancing microporosity.

Activation time also affects the resulting microporosity. An increase in the activation time increases the surface area and pore volume of the resulting carbon product (Zhao, 2012). However, this parameter does not significantly affect the resulting carbon, only a marginal improvement (Fierro *et al.*, 2007).

Particle size is also seen as an important factor influencing the microporosity of the activated carbon produced. Samples with smaller particle sizes result in carbons with higher surface areas and micropore volumes (Ahmadpour and Do, 1996; Zhao, 2012).

2.5.1.4 Surface Chemistry

The quantity and type of surface groups influence adsorption properties. According to Zhao (2012), surface oxides are on the surface of activated carbons. There are also many heteroatoms on activated carbons, which is one of the reasons activated carbons have heterogeneous surface chemical heterogeneity. The type of heteroatoms present depends on the carbon precursor used for producing activated carbons and the activation agent, activation procedure, and post-treatment (Zhao, 2012). The main heteroatoms present in the activated carbon structure are oxygen, hydrogen, nitrogen, phosphorus, sulphur, and halogens (Valix *et al.*, 2006). Hydrogen bonds to the edge atoms of carbon layers while the other atoms connect to the edges and in-ring inside carbon

layers (El-Sayed and Bandosz, 2004). Boron and nitrogen have similar atomic sizes to carbon, making it easier to intercalate them into the carbonaceous network (Zhao, 2012).

The surface chemistry of the carbon is a major factor influencing its hydrogen adsorption. Hydrogen can be decomposed into atomic hydrogen and then chemisorbed. This depends on pressure, temperature, and local surface structure (Volpe and Cleri, 2003). Equilibrium depends on the competing processes of H_2 dissociation, atomic H chemisorption forming the C-H group, and H abstraction, which happens through either surface diffusion-collision or infringing H atoms from the gas phase (Volpe and Cleri, 2003).

2.5.1.5 Porous Structure

The pore structure of the activated carbon is an important parameter that influences its adsorptive properties. The pore structure is a collective term for the surface area, the pore volume, and pore size distribution.

Specific surface area is the area of solid surface per unit mass of material. Gas adsorption measurements and other methods are used to determine the surface area of a material, with nitrogen adsorption at 77 K being the most popular method. Other types of gases can also be used, with carbon dioxide, methane, krypton, and argon preferred for gas adsorption studies other than nitrogen. The size of the probe molecule, 0.4 nm for nitrogen, determines the smallest pore size that can be investigated. In contrast, the maximum pore size investigated depends on the complexity of determining the quantity of gas adsorbed at high relative pressure. The maximum pore size for nitrogen is 300 nm (Zhao, 2012).

The International Union of Pure and Applied Chemistry has categorised adsorption isotherms into six classes, see Figure 2.13.

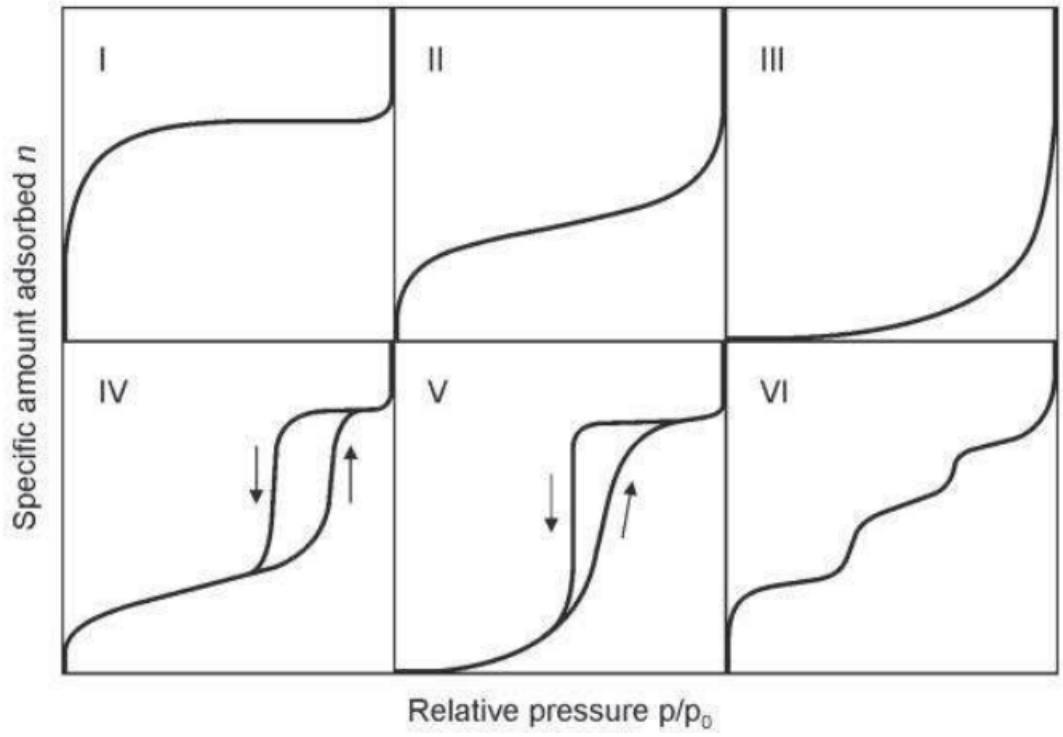

Figure 2.13 Classification of physisorption isotherms (2015 IUPAC) (Zhao, 2012)

Type-I isotherms are for microporous solid materials with small external surfaces (Ng *et al.*, 2017; Rowlandson, 2018). Type-II isotherms are for non-porous, macroporous adsorbents (Ng *et al.*, 2017; Rowlandson, 2018). These have unlimited monolayer-multilayer adsorption (Ng *et al.*, 2017; Rowlandson, 2018). Type III isotherms are for non-porous or macroporous systems where the adsorbate-adsorbate interactions are pronounced, though these are uncommon (Ng *et al.*, 2017; Rowlandson, 2018). Type-IV isotherms are for mesoporous material (Ng *et al.*, 2017; Rowlandson, 2018). The hysteresis loop shows capillary condensation in the mesopores with a limited uptake at higher relative pressures (Ng *et al.*, 2017; Rowlandson, 2018). Type-V isotherms are also for uncommon mesopores (Ng *et al.*, 2017; Rowlandson, 2018). Similar to type III, the adsorbate-adsorbate interactions are pronounced, and similar to type-IV, they exhibit hysteresis (Ng *et al.*, 2017; Rowlandson, 2018). Type-VI isotherms show stepwise multilayer adsorption on uniform, non-porous surfaces (Ng *et al.*, 2017; Rowlandson, 2018).

The pore volume of the activated carbons is mostly determined by nitrogen adsorption at 77 K. The total pore volume is determined at a relative pressure close to unity, 0.99, since the pores of the solid material are completely occupied here.

Activated carbons have different types of pores. Figure 2.14 shows a schematic cross-section of the various types of pores. Area a is composed of closed pores which are not accessible to external fluid and are isolated from their neighbours. These closed pores affect macroscopic characteristics: bulk density, elasticity, mechanical strength, and thermal conductivity. Areas b to f are open pores that are either through pores or blind pores. Pores are characterized by an open channel that starts on one end of the solid surface, passes through the particle, and emerges on the other like the c-e-c or c-e-d channels. Blind or dead-end pores are only open at one end, b and f are good examples of this type of pores. Smaller surface irregularities, such as those in area g, can also be classified as open pores, though they are usually considered separately as surface roughness; they should only be considered pores when they are deeper than their width (Zhao, 2012).

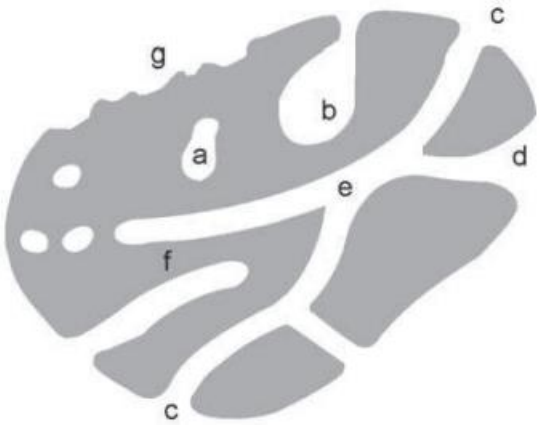

Figure 2.14 Cross-sectional schematic of a porous solid material (Zhao, 2012)

Pores are also grouped into about 5 types depending on their shapes: slit pores, conical pores, interstice pores, spherical pores, and cylindrical pores (Zhao, 2012). Figure 2.15 shows some of the common pore shapes in activated carbons.

Figure 2.15 Common pore shapes in activated carbons

The IUPAC classification of isotherms means that there are fundamentally three types of pores, depending on their width: micropores, mesopores, and macropores. Micropores are smaller than 2 nm, mesopores are between 2 and 50 nm wide, whereas macropores are much wider than 50 nm and up to 2000 nm. Adsorption in micropores occurs through volume filling. These pores have higher adsorption energy than the other pores.

2.5.2 Hydrogen Adsorption on Activated Carbon

2.5.2.1 Hydrogen Storage Mechanisms

Sorption refers to both adsorption and absorption. It is also used when differentiating between adsorption and absorption is difficult or for those processes where both adsorption and absorption are happening simultaneously. Adsorption is a surface process that results in the transfer of a molecule from the bulk fluid to a solid surface (Zarrouk and McLean, 2019). Absorption is not the same as absorption since it is when the fluid engulfs the whole material (Zarrouk and McLean, 2019). On the other hand, desorption is an emission process of chemical substances from a solid surface, effectively the opposite of sorption (Wandelt, K., 2018).

Two types of forces are involved in adsorption: (i) physical forces that are polarisation, dispersive, or short-range repulsive forces, and (ii) chemical forces that are valence forces emanating from the redistribution of electrons between the solid surface and the adsorbed atoms (Zhao,2012). Adsorption can be either physisorption or chemisorption, depending on the effective forces (Zhao,2012).

In physisorption, weak van der Waals forces bound the adsorbate to the surface. In chemisorption, there is an exchange of electrons between the adsorbate molecules and the adsorbent's surface,

leading to a chemical reaction. This forms a chemical bond between the adsorbate and the adsorbent, which is much stronger than the forces in physisorption.

Two critical differences exist between physisorption and chemisorption. The first and most imperative is the amount of energy needed for the adsorption enthalpy of adsorption. The enthalpy of adsorption for physisorption is similar to the heat of liquefaction and rarely exceeds 20 kJ/mol. In contrast, the enthalpy change in chemisorption is between 40-400 kJ/mol (Zhao, 2012). The second difference is the thickness of the adsorbed phase. Physisorption's thickness can be uni- and multimolecular, whereas it is only unimolecular in chemisorption.

Hydrogen storage can occur at the surface and in the bulk fluid of the chemisorption media. Hydrogen is chemically bound to the medium's surface in superficial chemisorption processes. According to Carrington (2009), hydrogen dissociates at the surface and transfers into the bulk fluid through atomic diffusion using interstitial sites for bulk chemisorption. This is where the hydrogen is eventually added to the solid phase of the medium.

Physisorption storage happens mainly through porous and nano-structured media. High surface area-to-volume ratios create conditions for massive uptake, such as when activated carbons are used (Zhao, 2012). Physisorption is also easy to reverse since it does not result in the alteration of the molecules involved. The heat of adsorption for physisorption is also lower since there is no formation of chemical bonds. When temperatures exceed the critical temperature, gases are adsorbed as low-density monolayers on the surface. The heat of adsorption for the second and subsequent layers is smaller than that of the first. Consequently, multilayers are only observed when temperatures decrease to close to or below the critical temperature of the adsorbate. Since hydrogen's boiling point is -252.9 °C and its critical temperature is -240 °C, it is adsorbed as a monolayer at 77 K (-196.15 °C) without any multilayer adsorption, which is observed at 20 K (-253.15 °C) (Zhao, 2012).

Physisorption of hydrogen onto activated carbons leads to type-I isotherms, as shown in Figure 2.16. The amount adsorbed increases linearly with pressure at low pressures, the Henry's law region. As the pressure increases, the monolayer becomes saturated and deviates from linearity.

Suppose the system temperature is near or below the critical temperature of the adsorbate. In that case, multilayer adsorption begins to form following the saturation of the monolayer. The amount of gas adsorbed at higher pressure increases slightly with pressure. Materials with very small pores show very limited multilayer formation, if any, and a horizontal plateau of the isotherm is produced. As the pressure nears the pressure of liquefaction, where the relative pressure is close to 1, the gas in the pores and surroundings liquefies, and massive adsorption is seen.

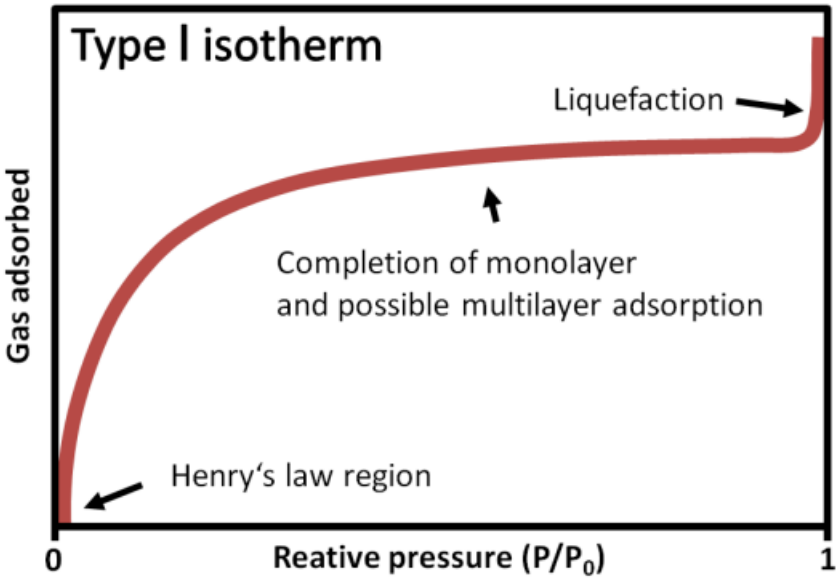

Figure 2.16 Type-I isotherm from the IUPAC classification (Streppel, 2011)

Hydrogen adsorption capacity can be explained in three different ways: excess, absolute, and total adsorption (Zhao, 2012; Streppel, 2011). Figure 2.17 shows a schematic of these adsorption capacities. Excess hydrogen adsorption or storage is characterized by increased adsorption with pressure, which then decreases. Absolute hydrogen storage is characterized by increased adsorption with increased pressure until a horizontal plateau is reached at higher pressure. This curve is above the one for excess adsorption. The total hydrogen adsorption capacity curve is the biggest, showing a continuous rise in hydrogen adsorption even at high pressures.

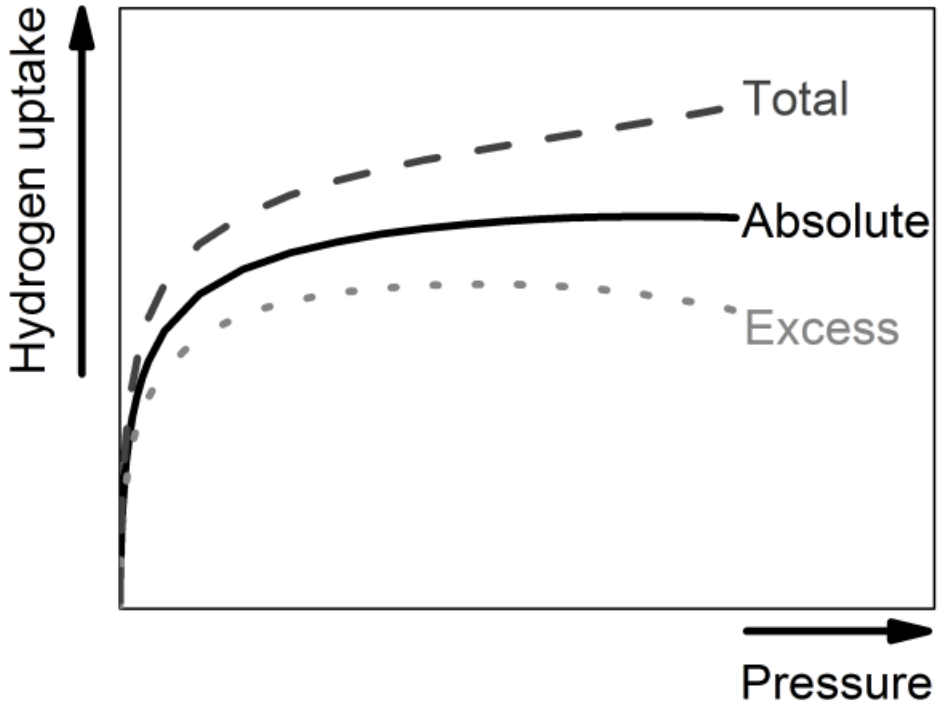

Figure 2.17 Isotherms for excess, absolute, and total hydrogen uptake (Streppel, 2011).

2.5.2.2 Effects of Surface Area and Pore Volume on Adsorption

The specific surface area and the micropore volume are extremely important parameters for hydrogen storage. Numerous research studies have shown that the hydrogen storage capacity of most activated carbons is proportional to their surface area and pore volume (Wang *et al.*, 2009; Panella *et al*., 2005).

Panella *et al*. (2005) conclude their study of different carbonaceous materials that had optimised structures by making the key observation that a linear relation between hydrogen uptake and specific surface area (SSA) was obtained for all samples regardless of the nature of the carbon material used. Other research work found that the hydrogen adsorption capacity of activated carbons increased as the total surface area and micropore volumes increased (Texier-Mandoki *et al.*, 2004).

A linear relationship between maximum hydrogen uptake at 77 K and BET-specific surface area was observed, and a plateau beyond this region due to saturation of the hydrogen storage capacity

(Fierro *et al.*, 2010). Figure 2.18 shows the correlation between S_{BET} and H_2 uptake at 77 K, as reported by various authors. It is very clear that hydrogen storage depends on both highly specific surface areas and well developed pores.

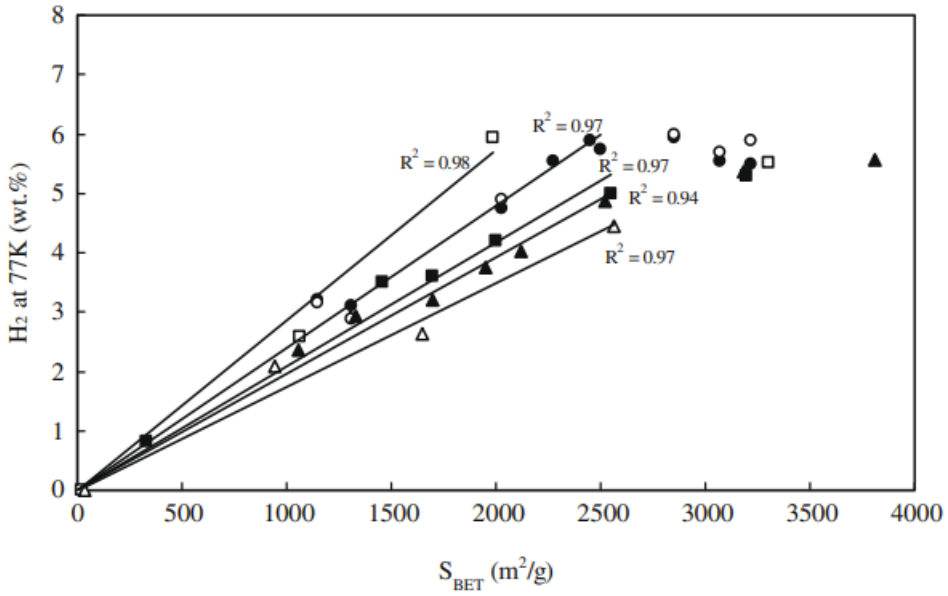

Figure 2.18 Correlation between S_{BET} and H_2 uptake at 77 K reported by various authors, □ (Xu *et al.*, 2007), ■ (Kabbour *et al.*, 2006), Δ (Panella *et al.*, 2005), ▲ (Jordá-Beneyto *et al.* 2007), ◯ (Fierro *et al.*, 2010) and ●(Fierro *et al.*, 2010).

2.5.2.3 Effects of Pore Size Distribution on Adsorption

The pore size, in combination with the specific surface area and pore volume, determines the total amount of hydrogen adsorbed. Several studies that evaluated the optimum pore diameters for hydrogen adsorption suggest diameters in the 0.5-0.7 nm region (Rzepka *et al.*, 1998; Celzard *et al.*, 2007). Cabria *et al.* (2007) suggested pore widths of 0.56 nm for applications at 77 K and any pressure of 0.6 nm for applications at 300 K at 10 Mpa if the DOE targets for hydrogen storage are to be met. According to Rzepka *et al.* (1998), the best pore geometry at room temperature is a slit pore with two graphite platelets whose distance apart should equal about twice the diameter of a hydrogen molecule. The presence of homogeneous microporosity was also shown to be important for hydrogen adsorption and storage (Texier-Mandoki, 2004). Ideal carbon material for hydrogen storage should have well developed microporosity with a small pore dimension.

2.6 The Circular Economy

2.6.1 The circular economy

The notion of the circular economy is a relatively contemporary concept. The concept has been thoroughly defined within several industries that have distinct vested interests. However, the establishment of a broadly agreed definition for this term remains elusive.

Geissdoerfer, Savaget, Bocken, and Hultink (2017) undertook a study to ascertain the current state of the circular economy, and found that it still remains a relatively emerging idea. Europe has been recognized as a leading region in this particular domain. However, it is crucial to acknowledge that many other entities worldwide have also arisen, showcasing noteworthy legislative and strategic objectives (Geissdoerfer *et al.*, 2017).

Stahel and Reday (1976) introduced the notion of a circular economy to elucidate the economic and industrial systems that would facilitate waste reduction, job creation, material minimization, and resource optimization. The contemporary comprehension of the Circular Economy has been broadened to encompass several issues or facets of this self-sustaining system. The aforementioned factors encompass regenerative design, cradle-to-cradle principles, ecological conservation legislation, closed-loop performance economy, industrial ecology, and the utilization of resources in a manner that aligns with existing life forms and biodiversity (Lyle, 1996; Stahel, 2010; Smith-Godfrey, 2016; Lee, Noh, & Khim, 2020).

According to the research conducted by Yuan, Bi, and Moriguichi (2006), the fundamental principle of the circular economy is in the establishment of a closed circular flow of materials, wherein raw materials and energy are utilized in many phases (Geissdoerfer *et al.*, 2017). The circular economy was defined by the Ellen MacArthur Foundation in 2013 as an industrial economy that aims to restore or regenerate its input (Geissdoerfer *et al.*, 2017; Ellen MacArthur Foundation, 2020). According to the Ellen MacArthur Foundation (2020), circular economy is predicated upon three fundamental design principles: the eradication of waste and pollution, the circulation of products and materials, and the regeneration of nature.

The primary focal points in the field of the circular economy encompass closed-loop value and supply chains, closed-loop product design, and closed-loop business strategies aimed at optimizing

resource utilization efficiency (Guide Jr and Van Wassenhove, 2009; Stindt and Sahamie, 2014; Govindan, Soleimani and Kannan, 2015; Bocken, De Pauw, Bakker and Van Der Grinten, 2016). Hence, the circular economy can be defined as a regenerative framework wherein the intentional reduction of raw materials, waste creation, and energy consumption occurs inside a closed-loop system that emulates the principles observed in natural ecosystems. Although the concept of circular economy does not encompass sustainability in its entirety, it holds significant relevance within the broader framework of sustainability.

2.6.2 Circular Economy and Waste Management

Businesses commonly provide reports on their corporate social responsibility (CSR) tasks, which are designed to showcase their contributions to sustainable development. These initiatives are an integral component of their environmental, social, and governance (ESG) practices. Waste management programs typically constitute a significant component of these reports. Nevertheless, there remains a lack of thorough inquiry by businesses about the potential cost-saving and revenue-generating prospects associated with these waste management activities (Romero-Hernández and Romero, 2018). There are emerging possibilities in using waste and repurposing products at the conclusion of their life cycles as inputs for manufacturing new products (Malinauskaite *et al.*, 2017; Romero-Hernández and Romero, 2018). The study conducted by Malinauskaite *et al.* (2017) examined the potential of using municipal waste from Eastern/Central Europe as a source of energy, exploring other methods beyond conventional incineration. According to Malinauskaite *et al.* (2017), waste management based on the principles of circular economy, has the potential to be an appealing investment.

The agricultural sector is recognized as a significant contributor to waste generation. According to a research by the Department of Environment, Forestry and Fisheries (DEFF) and Council for Scientific and Industrial Research (CSIR) in 2019, the annual food waste in South Africa amounts to approximately 10.3 million tonnes. Approximately 34% of the local food production and roughly 45% of the readily available food supply in South Africa can be attributed to this factor, since the country functions as a net food exporter (DEFF and CSIR, 2019; Bega, 2021). The consequences that ensue have significant impacts on both the economy and the environment, with far-reaching ramifications relating to climate change. The largest amount of food waste consists

of agricultural waste. The aforementioned loss implies that the resources used for the production of food, including water, electricity, and the entire supply chain, are likewise wasted (Bega, 2021). The recycling and use of agricultural waste within the framework of the circular economy is thus a viable option.

Avocado waste represents a significant portion of discarded food products, however it possesses considerable untapped potential. The use of waste and by-products derived from the avocado sector holds significant value as feedstock for both food and non-food applications (Colombo and Papetti, 2019). The utilization of starch derived from avocado seeds has been investigated for potential application in the textile industry. The research findings indicate that the extracted starch exhibits a starch content over 90% and demonstrates comparable performance to commercially available starch samples (Tesfaye *et al.,* 2018). The utilization of Supercritical Fluid Extraction (SFE) methods for the extraction of quercetin and catechin from avocado seed and peel waste holds significant implications in the pharmaceutical industry (Restrepo-Serna *et al.,* 2022). The study conducted by Restrepo-Serna *et al.* (2022) shown that the integration of biorefinery techniques in the valorisation of avocado waste resulted in reduced production costs and improved profit margins compared to stand-alone valorisation procedures (Restrepo-Serna *et al.*, 2022). The utilization of avocado peels and seeds in the food and cosmetics industries has been also explored for their bioactive components, particularly phenols (Colombo and Papetti, 2019). According to Colombo and Papetti (2019), carbonaceous material derived from peels and seeds has been used for the purpose of water purification, namely for the removal of pollutants. The utilization of avocado waste has also been explored in several applications, including the manufacture of biofuels and photocatalysis, as well as its usage as adsorbents, modified bio-based sorbents, and precursors for the synthesis of activated carbon adsorbents (Colombo and Papetti, 2019; Karić *et al.*,2022). There is a noticeable gap in the use of avocado waste as an environmentally friendly adsorbent for hydrogen storage purposes.

In recent years, there has been a notable increase in the application of biomass waste-derived products, leading to their widespread adoption in various profitable daily applications. The use of waste hazelnut shells has been recently explored as a precursor for the production of carbonaceous carbon dioxide sorbents, as demonstrated in studies conducted by Pang *et al.* (2020) and Serafin

et al. (2019). The production of porous carbons from lotus stalks has yielded materials with notable attributes, including exceptional carbon dioxide adsorption capabilities, excellent recyclability, and rapid adsorption kinetics. The carbon product electrode exhibited a notable specific capacitance and revealed a high level of stability, with approximately 95% retention rate even after undergoing 5000 cycles. These findings suggest that the biomass-derived products possess favourable characteristics for utilization as supercapacitors (Li *et al.*, 2021; Serafin *et al.*, 2019). Extensive research has been conducted on the utilization of biomass waste for the production of activated carbons, which serve as a promising material for hydrogen storage. Ariharan *et al.* (2021) conducted a study in 2021 to provide additional evidence on the efficacy of biomass-derived porous carbon as a superior material for hydrogen storage and supercapacitor applications (Ariharan *et al.*, 2021). According to Lv *et al.* (2018), carbon products derived from biomass pine nutshells exhibited remarkable characteristics such as an exceptionally high specific surface area, a significant pore volume, and demonstrated good electrochemical performance when used as supercapacitors. The uses of these materials are particularly appealing due to their well-developed porous structure.

2.8 Universal Adsorption Isotherm Model

The thermodynamics of adsorbate-adsorbent interactions are influenced by various factors, including pore size distributions, surface heterogeneity, site energy distribution, and adsorbate properties. Adsorption isotherms typically represent the equilibrium relationship between the quantity of adsorbate that is adsorbed onto the adsorbent and the concentration of the adsorbate in the solution. These isotherms are commonly influenced by several factors, including the adsorbent's chemical composition and surface area.

Prior to 2017, the existing adsorption isotherm models mostly focused on specific vapor intake, lacking a universally applicable model capable of describing the adsorption behaviour of diverse vapors. Table 2.5 presents a concise overview of some widely recognized adsorption isotherm models. In their study, Ng *et al.* (2017) demonstrated the feasibility of constructing a comprehensive model that encompasses the characteristics of various sorption isotherm types. This was achieved by integrating a modified Langmuir model with the concepts of Homotattic Patch Approximation (HPA) and multiple site energy sets, along with their corresponding fractional probability factors.

The sorption phenomena occurring on porous adsorbents have significant applications and attract considerable attention in both industrial and environmental contexts. Physical sorption is a process in which gas molecules are captured by the site energies of porous adsorbents. The pores have the potential to undergo natural or chemical functionalization processes, resulting in the creation of heterogeneous surfaces that possess specific energy locations. The isotherms that arise from heterogeneous surfaces including energy sites with different probability of capturing vapor are essential data for the design of sorption-based process cycles.

Table 2.5 General classifications of some of the adsorption isotherms (Saleh, 2022)

Adsorption Isotherm Models	
Model	**Examples**
Adsorption empirical isotherms	• Linear model (Henry's law) • Freundlich isotherm • Redlich—Peterson (R—P) isotherm • Sips isotherm model • Toth isotherm model • Temkin isotherm
Models based on Polanyi's potential theory	• Dubinin-Radushkevich (D-R) model • Dubinin Astakhov (D-A) model
Chemical adsorption models	• Langmuir model • Volmer isotherm model
Physical adsorption models	• BET model • Aranovich model

Ion exchange isotherm model	• Monovalent ions exchange • Bivalent ions exchange • Homovalent exchanges • Heterovalent exchanges

Popular isotherm models, namely those by Henry, Toth, and Langmuir, have limitations in higher-pressure regions where the Henry region of saturation conditions is invalid. Various scholars, including Jaroniec and Marczewski (1983-1984), modified Toth's approach using a power function but could not accurately model the saturation region (Marczewski and Jaroniec, 1983; Myers and Belfort, 1984; Jaroniec and Marczewski, 1984). Dubinin and Astakhov had around 1971 come up with better isotherm models that modelled the near saturation regions well but struggled in the low-pressure regions (Dubinin and Astakhov, 1971). In 2014, Chakraborty and Sun added the Fermi-Dirac distribution to the Langmuir model. They generated improved isotherms for multi-type adsorptions but could not accurately capture types IV and VI isotherms. In 2013, Yahia *et al.* proposed models for Type-VI isotherms using statistical mechanical formulation.

Ross and Olivier (1964) introduced Homotattic Patch Approximation (HPA), through which the heterogeneous surface of adsorbent is partitioned into finite homogeneous surfaces having constituent site energy that makes up the energy distribution functions over the respective surfaces. Applying the HPA resulted in improved models, but the complexity of the heterogeneous surface rendered some of these improvements applicable to some types only; a global method was still not found.

Ng *et al.* (2017) sought to create a unified approach for the adsorption isotherm model by amalgamating (i) the HPA, (ii) the revised Langmuir model, and (iii) the fractional probability factor for the distribution of site energy sets to create a universal model that simplifies adsorption on the complex heterogeneous porous surface. Figure 2.19 shows adsorption on the complex heterogeneous porous surface that the universal model approximates.

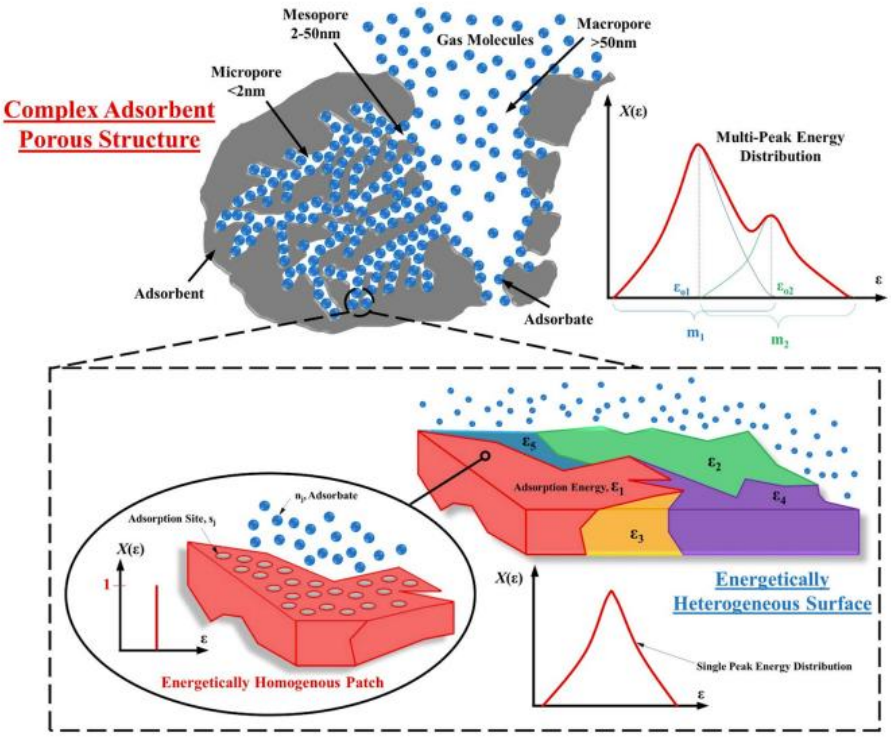

Figure 2.19 Adsorption on Complex Heterogeneous Porous Surface (Ng *et al.*, 2007)

Equations and Parameters of the Universal adsorption isotherm model

Equations of the universal adsorption isotherm model and a discussion on its parameters is included in section 3.8 since they are also the method. Please refer to section 3.8 for a breakdown of the equations and parameters of the universal adsorption isotherm model.

CHAPTER 3: MATERIALS AND METHODS

3.1 Introduction

This chapter details the materials and methods used in the study. It describes the methods of raw materials collection, preparation, and characterization, hydrothermal pretreatment, and activated carbon synthesis. The design of experiments used to investigate the effects of activation temperature and chemical weight ratio on mass yield, pore properties, and hydrogen adsorption is included. Characterization techniques, equipment used, and the modelling design are also featured in this chapter.

3.2 Materials

The avocado waste (peel and seed) used for this work was received from an Avocado Processing Plant in Limpopo, South Africa. Sigma Aldrich supplied 99% KOH and HCl 32% AR (10.18 mol/L). Liquid nitrogen, nitrogen, and hydrogen gas were supplied by Afrox, South Africa.

3.3 Methods

3.3.1 Sample Collection

The avocado waste was collected from the processing plant in an airtight sample bag and was clearly labeled for proper identification. The samples were stored and prepared under laboratory conditions (room temperature).

3.3.2 Sample Preparation

The avocado waste was dried under laboratory conditions for 48 hours. After drying, the sample was ground and sieved to an average 100 – 200 µm particle size. As shown in Figure 3.1, the resulting powder was stored for characterization and hydrothermal carbonisation.

Figure 3.1 Ground avocado waste before hydrothermal carbonisation

3.3.3 Sample Characterization

Proximate analysis of the avocado waste was carried out to determine the sample's moisture, ash, volatile matter, and fixed carbon content using Leco TGA 701. One gram (1g) of the sample was used for the analysis. The moisture content, ash content, and volatile matter were determined analytically, while the fixed carbon was determined by difference.

Ultimate analysis was carried out to determine the elemental composition of the avocado waste sample (total carbon, hydrogen, nitrogen). The percentage of oxygen content was calculated by difference. LECO TruSpec CHN equipment was used for the ultimate analysis, while LECO C & S Analyser was used for the total sulphur.

3.4 Hydrothermal Carbonisation

A Berghof stirred pressure reactor, whose contents were stirred at 250 rpm, was used for converting the avocado waste to hydrochar. The biomass-to-water ratio was kept at 0.125, the reaction temperature varied between 180 ℃, 200 ℃, and 220 ℃, retention time was kept constant at 6 hours (Masoumi *et al.*, 2021). Following the reaction, the reactor was allowed to cool before the content was emptied onto a filter paper and allowed to separate the liquid and solid contents. The solid content was dried and stored for analysis. Figure 3.2 shows the hydrochar produced at 200 ℃ from this process.

Figure 3.2 Hydrochar produced at 200 ℃.

3.5 Synthesis of Activated Carbon

3.5.1 Chemical Activation

Phase 1: Determining the best hydrochar

In the first phase, the three hydrochars produced in the hydrothermal pretreatment phase were respectively chemically activated with potassium hydroxide (KOH) at a 1:3 ratio at 800 ℃ in a furnace (Figure 3.3) in the presence of nitrogen. The samples were heated from room temperature to 800 ℃ at a rate of 15 ℃/min. Once at 800 ℃, the samples were left at this temperature for 2 hours. After 2 hours, the furnace was switched off to allow the samples to cool down in the presence of nitrogen.

Phase 2: Determining the best sample: KOH activation ratio

In the second phase, the hydrochar prepared at 200 ℃ in the pretreatment phase was used to prepare three samples for determining the best activation ratio. Three samples were chemically activated with potassium hydroxide (KOH) at 1:1, 1:2, and 1:3 ratios, respectively, at 800 ℃ in a furnace in the presence of nitrogen. The samples were heated from room temperature to 800 ℃ at a rate of 15℃/min. Once at 800 ℃, the samples were left at this temperature for 2 hours. After 2 hours, the furnace was switched off to allow the samples to cool down in the presence of nitrogen.

Figure 3.3 Horizontal Tube Furnace

Phase 3: Determining the effect of activation temperature

In the third phase, the hydrochar prepared at 200 ℃ in the pretreatment phase was used to prepare three samples for determining the best activation temperature. The three samples were chemically activated with potassium hydroxide (KOH) at a 1:3 ratio, at 700 ℃, 800 ℃, and 900 ℃, respectively, in a furnace in the presence of nitrogen. The samples were heated from room temperature to 700 ℃, 800 ℃, and 900 ℃, respectively, at a rate of 15 ℃/min. Once at the desired temperature, the samples were left for 2 hours. After 2 hours, the furnace was switched off to allow the samples to cool down in the presence of nitrogen. The cooled samples were washed with hydrochloric acid and dried at 90 ℃ in an oven overnight. The resulting activated carbons were stored in airtight glass bottles for characterization and analysis.

3.6 Characterization of Synthesised Activated Carbon

3.6.1 Nitrogen Gas Adsorption

The nitrogen gas adsorption technique measures the average pore size, total pore volume, and surface area of porous materials. The surface area and porosity of many materials are critical physical properties that influence their suitability and thus determine the purposes for which these materials are used.

Using an autosorb iQ Gas Sorption System (Figure 3.4), 0.2g of each sample was measured and degassed at 200 °C for 12 hours in a nitrogen flow to perform the nitrogen adsorption test at 77 K. After that, the samples were moved to the analysis port for nitrogen sorption analysis. The nitrogen adsorption data were used to compute: (i) total pore volume, V_T, determined at a relative pressure of $P/P_o = 0.99$ (Gregg *et al.*, 1967); (ii) surface area, S_{BET}, using the BET method (Brunauer *et al.*, 1938); (iii) pore size was obtained from the desorption data of the N_2 isotherms using the Barrett-Joyner-Halenda (BJH) method (Barrett *et al.*, 1951).

The total pore volume is determined from the plateau of the adsorption isotherm. The plateau of the isotherm represents saturation. The total pore volume V_T is a function of the mass of gas adsorbed m_{ad}, the liquid density at the operational temperature ρ_l, and the total mass of the sample m_T.

$$V_T = \frac{m_{ad}}{\rho_l m_T} \tag{3.1}$$

where V_T is the total pore volume, m_{ad} the mass of gas adsorbed, ρ_l the liquid density at operational temperature and m_T the total mass of the sample.

The specific surface area is determined through the Brunauer-Emmett-Teller (BET) method. The amount of gas required to cover the external and internal pore surfaces of an adsorbent/solid material with a single layer of adsorbate is calculated from the adsorption isotherm. There are two stages in determining the BET surface area: first, determining the monolayer amount, n_m, and secondly, calculating the BET surface area from the molecular cross-sectional area, a_m.

Step1: Determining the monolayer amount, n_m

$$\frac{{}^{p}/_{p_0}}{n_a(1-{}^{p}/_{p_0})} = \frac{1}{n_m C} + \frac{C-1}{n_m C}\frac{p}{p_0} \quad (3.2)$$

Where n_a is the amount of gas adsorbed, ${}^{p}/_{p_0}$ is the relative pressure, and C is the BET parameter. The C parameter corresponds to the C-constant, $C = \exp(q_1 - q_L)/RT$ where q_1 is the heat of adsorption and q_L heat of condensation at the point where the monolayer is formed (Ladavos *et al.*, 2012). It is also related to the heat of adsorption in the first adsorbed layer. It shows the amount of the adsorbent-adsorbate interaction energy. Values for micropore filling are greater than 200. The BET method requires a linear relationship between $({}^{p}/_{p_0})$ / [$n_a(1 - {}^{p}/_{p_0})$] and ${}^{p}/_{p_0}$within the ${}^{p}/_{p_0}$ range of 0.05 to 0.30. Linear regression can be used to determine the monolayer amount, n_m.

Step2: Calculating the BET surface area from the molecular cross-sectional area, a_m

$$S_{BET} = \frac{n_m a_m N_A}{m_{sample}} \quad (3.3)$$

The molecular cross-sectional area a_m of nitrogen at 77 K is 0.162 nm^2. N_A is Avogadro's constant and m_{sample} is the mass of the dry sample.

Figure 3.4 autosorb iQ Gas Sorption System

3.6.2 SEM/EDS Technique

SEM/EDS is a combined technique that uses a scanning electron microscope and energy-dispersive X-ray spectroscopy to analyse the structure and composition of various materials. SEM is used for the imaging or structural analysis, and EDS is used for detection or composition analysis. Scanning electron microscopy (SEM) uses a beam of high-energy electrons to create an optical signal, the image of the sample's morphology (Labmanager, 2023; Rowlandson, 2019). The microscope creates a beam of electrons from an emitter-cathode within an electron gun. The beam is then accelerated and focused by an anode and a series of electromagnetic lenses. It is scanned across the sample's surface, interacting with the atoms in the sample and causing secondary electrons to be emitted from the surface. The emitted secondary electrons then reach the EDS detector. EDS measures this energy to determine the elements present in the sample and their concentrations.

When the beam of primary electrons hits the surface of the sample, bulk solid, the electrons are either reflected or adsorbed, resulting in a number of optical signals. A photomultiplier collects these signals to create an image. The high accelerating voltage is used to increase the resolution of

this image. However, this voltage must not be high enough to change the sample and downgrade the quality of the produced image. Refer to Figure 3.5 for a schematic of this.

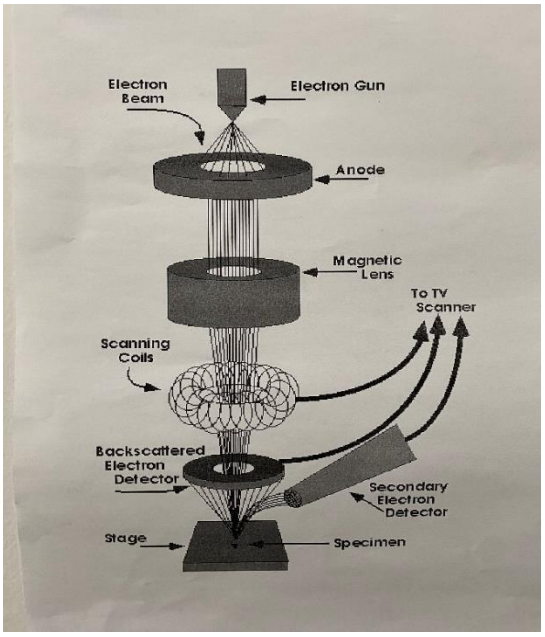

Figure 3.5 Schematic of how the ZEISS Sigma SEM/EDS equipment works

The surface morphology of the activated carbon samples was observed using a Carl Zeiss Sigma Field Emission Scanning Electron Microscope equipped with an Oxford X-act EDS detector (Figure 3.6). Coating of the carbon-containing sample was not necessary due to the conductivity of the carbon samples.

Figure 3.6 ZEISS Sigma SEM/EDS Analysis equipment

3.6.3 X-ray Diffraction (XRD) Technique

Diffraction happens when waves interfere or bend around an obstacle or through a hole and spread out, often resulting in interference between these waveforms. X-ray diffraction (XRD) is a characterization technique that allows us to determine the position of atoms in a sample (Lyman, 1990; Rowlandson, 2019). When a sample is irradiated with a monochromatic beam of X-rays, elastic scattering of the photons can be observed. Constructive interference occurs when the X-rays are in phase and a peak is observed on the spectrum. However, destructive interference occurs when the X-rays are out of phase, and no peak is observed on the spectrum. The diffraction pattern observed is a plot of the intensity against the detector angle, 2θ.

Under favourable conditions, X-rays from a crystalline solid material can constructively interfere and produce a diffracted beam. The structures of crystals and molecules are usually determined using X-ray diffraction. Sir W.H. Bragg and his son Sir W.L. Bragg introduced Bragg's Law, which explains the relationship between an X-ray light incident and its reflection from a crystal surface. The law states that when the X-ray is incident onto a crystal surface, its incidence angle θ will reflect with the same scattering angle, θ and that when the path difference, d, equals to a whole number of wavelengths, n, constructive interference will happen (LibreTexts, n.d.).

Figure 3.7 illustrates this law. Assuming a crystal with lattice planes separated by a distance *d*, having monochromatic X-rays A, B, and C incident on it at angle θ. Atoms X, Y, and Z will be reflected. The path difference between the rays reflected at X and Y is 2YX. Suppose this path difference equals a whole number multiple of the wavelength. In that case, rays A and B (applicable to C) will also arrive at X in the same phase. This means that the scattered radiation will constructively interfere, and the crystal will appear to have reflected the x-radiation. If this is not true, destructive interference occurs.

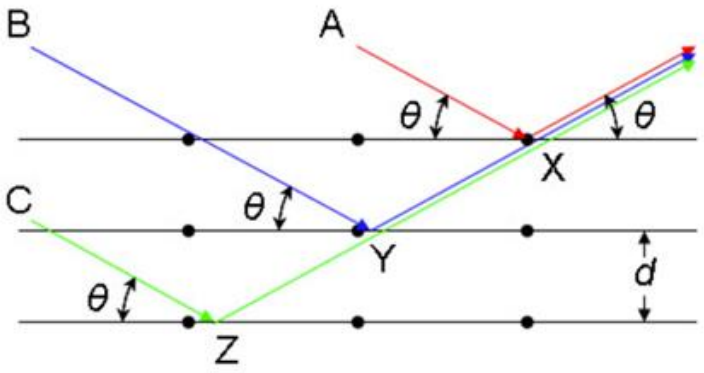

Figure 3.7: Bragg's Law illustration (Libretexts, n.d.)

The principle of Bragg's Law is used in building instruments to analyse the structure of crystals and molecules. The Bragg equation gives the angle at which constructive interference occurs:

$$n\lambda = 2dsin\theta \tag{3.4}$$

Rewritten,

$$sin\theta = \frac{n\lambda}{2d} \tag{3.5}$$

Where λ is the wavelength of the X-ray, *d* is the spacing of the crystal layers (path difference), θ is the incident angle (the angle between the incident ray and the scatter plane), and *n* is an integer. X-ray diffraction (XRD) was used to analyse the structural characteristics of the activated carbon samples. XRD patterns of the samples were observed.

The D2 PHASER Bruker Meas Srv D2-208365 with SSD 160 operated at 30 kV and 10 mA (Figure 3.8) was used to analyse the powdered activated carbon samples' response patterns, purity, and crystallography by X-ray powder diffraction. The DIFFRAC.SUITE Eva software suite, which

enables peak search for phase identification, was then used to compare the diffraction peaks with reference patterns.

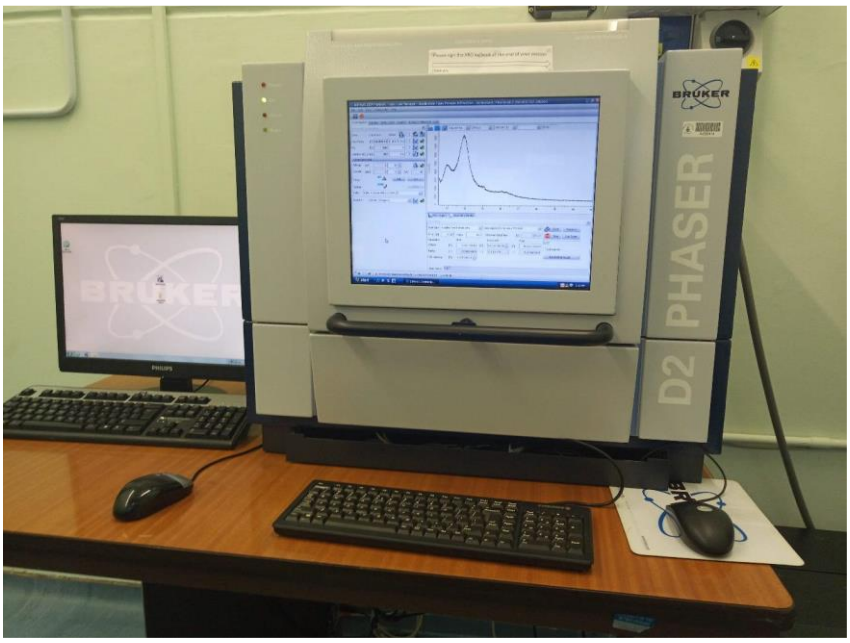

Figure 3.8 Image of Bruker D2 PXRD Phaser

3.6.4 FT-IR Technique

Fourier transform infrared (FTIR) spectroscopy, a popular infrared spectroscopy form, was used to determine the functional groups in the activated carbons (Merck n.d.). Infrared spectroscopies are designed based on the principle that when infrared light is incident on a sample, some radiation passes, and some is absorbed. The radiation passing through the sample is recorded in an infrared spectrum. An infrared spectrum, a plot of infrared light intensity against a property of light, records the specific wavelengths of radiation absorbed by the covalent bonds of the atoms present in the bond to give off the stretching or bending vibrational energy.

It is convention that the high wave number is plotted to the left of the x-axis of an infrared spectrum and the low wave number to the right (Smith, 2011). Absorbance units measure the amount of light absorbed by a sample. Peaks point up, and the highest amount of light absorbed by the sample is reflected at their tops.

The adsorbance spectrum of a sample is calculated from the equation:

$$A = \log\left(\frac{I_0}{I}\right) \tag{3.6}$$

Where A is the absorbance, I_0 intensity in the background spectrum and I the intensity in the sample spectrum. Absorbance is also correlated to the concentration of molecules in a sample, according to the Beer's Law equation (Smith, 2011):

$$A = \varepsilon l c \tag{3.7}$$

Where ε is absorptivity, l the length of the path, and c the concentration of molecules.

The height or area of a peak in an absorbance spectrum is proportional to concentration, and the concentration of molecules in a sample can be found using Beer's Law.

The y-axis of an infrared spectrum is usually plotted in percent transmittance (%T), the percentage of light transmitted by a sample. The following equation determines percentage transmittance (%T) spectra:

$$\%\mathrm{T} = 100 \times \left(\frac{I}{I_0}\right) \tag{3.8}$$

These variables are as defined above. When peaks point downwards, their bottoms show where the sample transmitted significantly less than 100% of the incident infrared light (Smith, 2011).

Absorbance and percentage transmittance are related and can be converted from one to the other, altering the y-axis without changing the peak positions. The equation shows that absorbance has a linear relationship with concentration, so absorbance units should be used on the y-axis for quantitative analysis applications since you can use either unit on the y-axis (Smith, 2011). Absorbance units are also suitable for qualitative analysis applications. Since the peak sizes in such spectra are not linearly proportional to concentration, percentage transmittance (%T) units spectra should not be used for quantitative analysis, spectral subtraction, or library searching.

Infrared spectra are used for a number of applications, the most common being to determine the molecules present in a sample. Peak positions in an infrared spectrum correspond to molecular structure. A number of spectra have been measured in the past, including peak positions of known molecules, which helps us determine molecules present in an unknown sample. These spectra can also be used to identify or compare spectra. The third application is to determine the concentration of molecules in the sample, using Beer's Law above.

FTIR is one of the most preferred infrared spectroscopy methods as it does not destroy the sample, is faster than most old techniques, and is more sensitive and precise (Merck n.d.). FTIR has a number of applications, including organic synthesis, petrochemical engineering, polymer science, food analysis, etc.

In this work, the spectra are recorded on graphs with wave numbers, which are 1/wavelength and give the energy of the vibration of the molecular bonds on the x-axis and percentage transmittance on the y-axis. The spectra were obtained by Perkin Elmer Spectrum 100 (Figure 3.9).

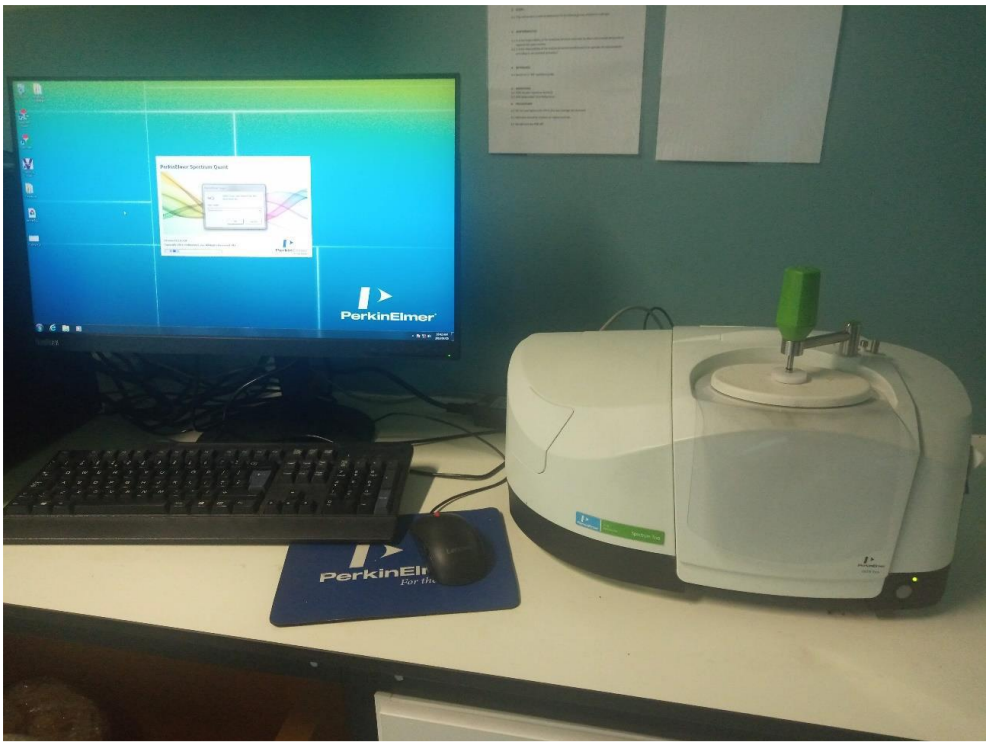

Figure 3.9 Perkin Elmer FTIR Spectrometer

3.7 Measurement of Hydrogen Adsorption on Activated Carbons

Hydrogen adsorption and desorption experiments were conducted under atmospheric pressure at -196 ◦C (77k). Measurements were carried out in an autosorb iQ Gas Sorption System. Prior to the adsorption test, about 2g of each synthesised activated carbon was degassed at 200 ^{o}C for 12 hours.

3.8 Modelling

3.8.1 Universal Adsorption Isotherm Model

The heterogeneous surface of the adsorbent was modelled by smaller homogeneous surfaces that are assumed to have the same energy levels. Each homogeneous surface was defined through the adsorption site energy's energy distribution function (EDF). The higher probability of an adsorption site indicated a higher localised adsorption uptake within a monolayer, whose energy distribution also depended on the types of pores. Multilayer formation also follows the same trend. A fractional probability factor, which represents the fraction of the total surface coverage or energy distribution of each pore size or adsorbate layer in the multilayer formation, was added to deal with variations in the multilayer formation (Ng *et al.*, 2017).

One molecule per adsorption site and homotattic patch approximation was assumed. The local adsorption uptake at a homogeneous patch/surface is:

$$\theta(\varepsilon)_j = \frac{n_j}{s_j} \tag{3.9}$$

Where n_j represents the number of molecules and s_j the local adsorption sites available. As a consequence, the total adsorption uptake available at an adsorbent surface is:

$$\theta_t = \frac{N_a}{S_0} = \sum_{j=1}^{\infty} \theta(\varepsilon)_j \tag{3.10}$$

Where N_a represents the total number of adsorbed molecules and S_o the total number of available sites. Expanding equation 3.10 to show the sum of all local coverage and fractional availability of the individual adsorption sites over the total surface (s_i/S_0):

$$\theta_t = \frac{s_1}{S_0}\theta_1 + \frac{s_2}{S_0}\theta_2 + \frac{s_3}{S_0}\theta_3 + \cdots + \frac{s_\infty}{S_0}\theta_\infty \tag{3.11}$$

The fractional factors are proportional to the energy distribution function X(ε), and their sum over the total adsorption surface equals 1,

$$\frac{s_i}{S_0}(\varepsilon) = X(\varepsilon)d\varepsilon \tag{3.12}$$

And the integral across all sites

$$\int_0^\infty X(\varepsilon)d\varepsilon = \sum_{i=1}^{\infty} \frac{s_i}{S_0}(\varepsilon) = 1 \tag{3.13}$$

It follows that the total adsorption uptake/coverage of the heterogeneous surface made up of the homogeneous patches when the localised adsorption uptake $\theta(\varepsilon)$, and the energy distribution function $X(\varepsilon)$ are know, is

$$\theta_t = \int_0^{\infty}\{\theta(\varepsilon)X(\varepsilon)\}d\varepsilon \tag{3.14}$$

When the rates of adsorption, R_a, and desorption, R_d, are known, the rate of adsorption uptake is given by:

$$\frac{d\theta(\varepsilon)}{dt} = R_a - R_d \tag{3.15}$$

The rate of adsorption and desorption, R_a and R_d, respectively, are given by the classical Absolute Rate Theory (ART):

$$\frac{d\theta(\varepsilon)}{dt} = K_a p(1-\theta) exp\left(\frac{-\varepsilon_a}{RT}\right) - K_d \theta exp\left(\frac{-\varepsilon_d}{RT}\right) \tag{3.16}$$

At equilibrium, the rates of adsorption and desorption are equal, meaning that $\frac{d\theta(\varepsilon)}{dt} = 0$.

To simplify equation 3.16, we let K = K_a/K_d and $\Delta\varepsilon = \varepsilon_d - \varepsilon_a = \varepsilon - h_f$, which gives us the revised Langmuir isotherm equation (3.17)

$$\theta(\varepsilon) = \frac{Kp\ exp\left(\frac{\Delta\varepsilon}{RT}\right)}{\left(1+Kp\ exp\left(\frac{\Delta\varepsilon}{RT}\right)\right)} \tag{3.17}$$

Using $\varepsilon_c = -RTlnKp$, the Langmuir isotherm equation is modified as:

$$\theta(\varepsilon) = \frac{exp\left(\frac{\Delta\varepsilon-\varepsilon_c}{RT}\right)}{\left(1+ exp\left(\frac{\Delta\varepsilon-\varepsilon_c}{RT}\right)\right)} \tag{3.18}$$

We can see from equation 3.18 that the adsorption uptake, $\theta(\varepsilon)$, is dependent on temperature.

Using the condensation approximation (CA), we can break down equation 3.14 to two parts:

$$\theta_t = \int_0^{\varepsilon_c}\{0 \times X(\varepsilon)\}d\varepsilon + \int_{\varepsilon_c}^{\infty}\{1 \times X(\varepsilon)\}d\varepsilon \quad CA: \left[\lim_{T\to 0}\theta(\varepsilon) = \theta_c(\varepsilon) = \begin{Bmatrix} 0\ for\ \Delta\varepsilon \le \varepsilon_c \\ 1\ for\ \Delta\varepsilon \ge \varepsilon_c \end{Bmatrix}\right]$$

$$\theta_t = \int_{\varepsilon_c}^{\infty} X(\varepsilon)d\varepsilon \tag{3.19}$$

Here, we see that the total adsorption uptake (θ_t) depends only on the energy distribution function of the adsorption energy sites, $X(\varepsilon)$. It is essential to accurately quantify the adsorption site distribution on the surface of many heterogeneous surfaces/patches if you are to quantify the adsorption uptake correctly. Multi-peak modelling of energy distribution is quite a useful way to reflect the adsorbent surface heterogeneity. However, a more representative mathematical expression exists to correctly identify and quantify the individual energy distribution function to the combined distribution function.

A Gaussian function can represent the fractional makeup of an adsorbent's total adsorption uptake between micro and macro pores or among multilayer formations. This function uses the probability factor, α, to represent the properties of the energy distribution of adsorption sites of the heterogeneous surface.

$$X(\varepsilon) = \sum_{i=1}^{n} \alpha_i \left\{ \frac{exp\left(\frac{\Delta\varepsilon - \varepsilon_{oi}}{m_i}\right)}{m_i\left[1+exp\left(\frac{\Delta\varepsilon-\varepsilon_{oi}}{m_i}\right)\right]^2} \right\} \tag{3.20}$$

Making equation 3.19

$$\theta_t = \int_{\varepsilon_c}^{\infty} \left[\sum_{i=1}^{n} \alpha_i \left\{ \frac{exp\left(\frac{\Delta\varepsilon-\varepsilon_o}{m}\right)}{m\left[1+exp\left(\frac{\Delta\varepsilon-\varepsilon_o}{m}\right)\right]^2} \right\}_i \right] d\varepsilon \tag{3.21}$$

If we solve the integral and let $\varepsilon_c = -RTlnKp$,

$$\theta_t = \sum_{i=1}^{n} \alpha_i \left\{ \left[1 + exp\left(\frac{-RT\ lnKp-\varepsilon_o}{m}\right)\right]^{-1} \right\}_i \tag{3.22}$$

If we further simplify this by letting the adsorption equilibrium constant K = 1/p_s, where p_s is the saturation pressure at the maximum possible uptake by an adsorbent, the model becomes:

$$\theta_t = \sum_{i=1}^{n} \alpha_i \left\{ \frac{\left(\frac{p}{p_s} exp\left(\frac{\varepsilon_{oi}}{RT}\right)\right)^{\frac{RT}{mi}}}{1+\left(\frac{p}{p_s} exp\left(\frac{\varepsilon_{oi}}{RT}\right)\right)^{\frac{RT}{mi}}} \right\}_i \tag{3.23}$$

A larger value of m indicates high surface heterogeneity, leading to a smaller slope of the isotherm graph. The opposite is also true, as there is a wider spread and low fractional peak of the corresponding energy distribution curve.

The energy distribution of Type-I to type-V has two nominal peaks, meaning that n=2 (Ng *et al.*, 2017). This means that we can further breakdown equation 26 using two probability factors whose sum is one, $\alpha_1 + \alpha_2 = 1$:

$$\theta_t = \alpha_1 \left[\frac{\left(\frac{p}{p_s} exp\left(\frac{\varepsilon_{o1}}{RT} \right) \right)^{\frac{RT}{m1}}}{1+\left(\frac{p}{p_s} exp\left(\frac{\varepsilon_{o1}}{RT} \right) \right)^{\frac{RT}{m1}}} \right] + \alpha_2 \left[\frac{\left(\frac{p}{p_s} exp\left(\frac{\varepsilon_{o2}}{RT} \right) \right)^{\frac{RT}{m2}}}{1+\left(\frac{p}{p_s} exp\left(\frac{\varepsilon_{o2}}{RT} \right) \right)^{\frac{RT}{m2}}} \right] \tag{3.24}$$

As Type-VI isotherm's energy distributions have four peaks, four probability factors are used to express the energy distribution functions, $\alpha_1 + \alpha_2 + \alpha_3 + \alpha_4 = 1$

$$\theta_t = \alpha_1 \left[\frac{\left(\frac{p}{p_s} exp\left(\frac{\varepsilon_{o1}}{RT} \right) \right)^{\frac{RT}{m1}}}{1+\left(\frac{p}{p_s} exp\left(\frac{\varepsilon_{o1}}{RT} \right) \right)^{\frac{RT}{m1}}} \right] + \alpha_2 \left[\frac{\left(\frac{p}{p_s} exp\left(\frac{\varepsilon_{o2}}{RT} \right) \right)^{\frac{RT}{m2}}}{1+\left(\frac{p}{p_s} exp\left(\frac{\varepsilon_{o2}}{RT} \right) \right)^{\frac{RT}{m2}}} \right]$$

$$+\alpha_3 \left[\frac{\left(\frac{p}{p_s} exp\left(\frac{\varepsilon_{o3}}{RT} \right) \right)^{\frac{RT}{m3}}}{1+\left(\frac{p}{p_s} exp\left(\frac{\varepsilon_{o3}}{RT} \right) \right)^{\frac{RT}{m3}}} \right] + \alpha_4 \left[\frac{\left(\frac{p}{p_s} exp\left(\frac{\varepsilon_{o4}}{RT} \right) \right)^{\frac{RT}{m4}}}{1+\left(\frac{p}{p_s} exp\left(\frac{\varepsilon_{o4}}{RT} \right) \right)^{\frac{RT}{m4}}} \right] \tag{3.25}$$

Equations 3.24 and 3.25 are expanded from equation 3.23 to reflect the number of sets of adsorption sites available and their distributions in an isotherm. Two terms for Type-I to type-V isotherms and four terms for Type-VI isotherms, but less or more than four terms can be used for Type-VI isotherms considering the complexity of the multilayer behaviour.

3.9 Summary

The methods of raw materials collection, preparation, and characterization were detailed in this chapter. The avocado waste pretreatment process was elaborated on. The method used to design the experimental setup for activated carbon synthesis was explained. Critical parameters that influence the work and those studied were explained in detail. An explanation of the respective characterization techniques was undertaken. The universal adsorption isotherm model parameters and equations governing the model were expanded.

CHAPTER 4: RESULTS AND DISCUSSION

4.1 SYNTHESIS AND CHARACTERIZATION OF ACTIVATED CARBONS FROM AVOCADO WASTE

4.1.1 Samples Characterization

The avocado used for the production of activated carbons was subjected to characterization in order to assess its composition and ascertain its high level of purity. The determination of the elemental composition of biomass through ultimate analysis, specifically assessing the carbon, hydrogen, nitrogen, oxygen, and sulphur (CHNOS) content, holds significance in the context of its carbonisation and activation conversion processes. The resulting carbonisation or activation product is contingent upon these elemental constituents (Islam *et al.*, 2001). The determination of the elemental composition of biomass plays a crucial role in the development and optimization of energy conversion and storage systems (Nhuchhen, 2016). The concentrations of carbon, hydrogen, nitrogen, sulphur, and oxygen in both the raw avocado waste and the hydrochars obtained during the pretreatment phase were examined to determine whether the hydrothermal process had enhanced the carbon content. Additionally, the suitability of these hydrochars as precursors for the synthesis of activated carbons was assessed. The analysis was conducted using an Elemental Analyser. The percentage weight difference of oxygen content was determined by conducting an elemental analysis of carbon, hydrogen, nitrogen, and sulphur in the samples. The hydrothermal treatment procedure was conducted within the temperature range of 180 to 220°C, following the methodology described in the literature by Aragón-Briceño *et al.* (2021).

According to Table 4.1, the oxygen content of avocado waste was found to be 49.03 wt%, which is somewhat greater than the typical oxygen concentration range of 40-45 wt% observed in woody and herbaceous biomass (Islam *et al.*, 2001). The avocado waste exhibited a notable abundance of oxygen, succeeded by carbon, hydrogen, and nitrogen in descending order of concentration. Since avocado roots and plants wither at low oxygen concentrations, the avocado waste's oxygen content is not surprising (Valoras *et al.*, 1964). Avocado roots exhibit a minimum oxygen diffusion rate of 20 $\mu g\ cm^{-2}\ min^{-1}$, which is essential for facilitating various soil adsorption activities.

It is evident that the carbon content in the avocado waste experienced a rise, rising from an initial value of 43.69 wt% to an average of 65.20 wt% in the hydrochars that were produced using the hydrothermal pretreatment method. The hydrothermal pretreatment method resulted in a weight increase of 21.00%. The determination of a carbon content of 43.69 wt% provides confirmation that avocado waste can be classified as wet biomass, since it surpasses the threshold of 30 wt% carbon, as established by Masoumi *et al.* (2021). The hydrochars subjected to various pretreatment temperatures exhibit minimal differences in their carbon, hydrogen, nitrogen, and oxygen compositions. According to Table 4.1, the hydrothermal treatment method effectively transferred a significant amount of oxygen from the solid fraction to the liquid fraction. As a result, the hydrochar obtained from this process exhibited enhanced stability, making it suitable for subsequent activation procedures.

Table 4.1 CHNS(O) elemental analysis of avocado waste and hydrochars from the hydrothermal process

Sample	Carbon (wt%)	Hydrogen (wt%)	Nitrogen (wt%)	Oxygen (wt%)	Sulphur (wt%)
Avocado waste	43.69	6.17	1.11	49.03	0.00
HC 180	65.11	5.41	1.39	28.09	0.00
HC 200	65.26	5.35	1.44	27.95	0.00
HC 220	65.13	5.3	1.42	28.15	0.00

Table 4.2 shows the ash content of the three hydrochars. The hydrochars show ash content less than 0.5 wt% (average 0.16 wt%). This ash content is similar to what is reported in literature for hydrochars produced from biomass, ranging between 0.1 and 14 wt.% (Ruiz *et al.*, 2015; Chen *et al*., 2016).

Table 4.2 ash content of the hydrochars from the hydrothermal process

Raw Material	Ash Content	
	Char	
	mg	wt.%
Hydrochar at 180℃	0.007045	0.068%
Hydrochar at 200℃	0.02322	0.22%
Hydrochar at 220℃	0.019	0.18%

Figure 4.1 shows the thermal decomposition of hydrochars, produced at 180, 200 and 220 ℃, in an inert atmosphere. The hydrochars decompose over a wide temperature range, up to about 1000 ℃, with five stages of weight loss. Weight loss for hydrochar prepared at 200 ℃ shows negative mass loss and a plateau for temperatures above 1000 ℃. The negative weight loss is an anomaly resulting from the sample overburn. The greater char yield was observed for hydrochar 180 (3.96 wt%), followed by hydrochar 220 (1.45 wt%) and no yield was observed for the hydrochar 200 as explained. Higher yields for this biomass could be realised at temperatures between 600 and 800℃ if degradation occurred in three phases. The yield for both hydrochars would be 41.35 wt% at 740 ℃, which is the first plateau before further erosion of the samples took place. The hydrochars have pronounced thermal stability below 800 ℃ but get weak at higher temperatures. Temperatures higher than 800 ℃ erode the carbon structure and any cross-links present in the carbon structure.

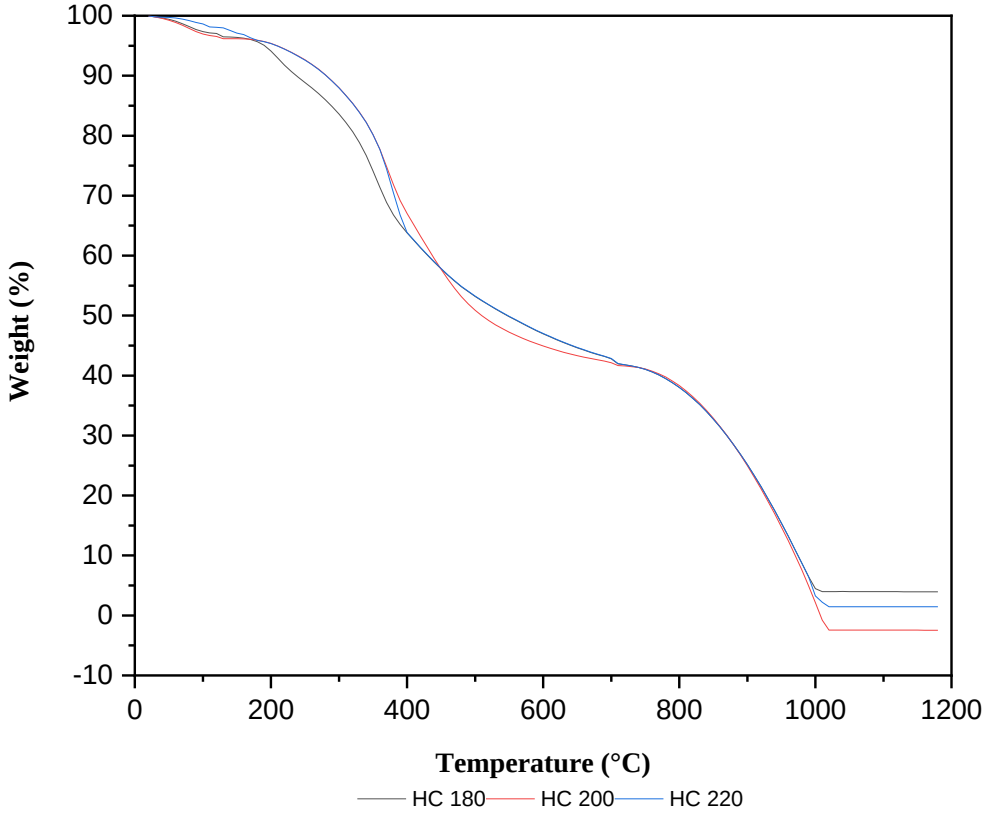

Figure 4.1 Thermogravimetric analysis of hydrochars produced at 180 and 200 ℃

In general, the findings from the characterization of the sample indicate that the avocado waste used underwent effective preparation procedures, including thorough washing and drying, to eliminate any contaminants and extraneous materials. The hydrothermal procedure enhanced the carbon content and ensured the presence of a substantial amount of carbonaceous material for the activation step. The material exhibited a high degree of purity, with minimal ash content and an absence of sulphur. The thermogravimetric curves demonstrate that hydrochar derived from avocado waste has a broad range of decomposition, which is characterized by many sequential steps. Optimal yields are achieved when temperatures are below 800 ℃, whereas total combustion of the samples occurs at temperatures beyond 1000 ℃.

4.2 Activated carbon Characterizations

Thermal stability and the decomposition behaviour of the produced activated carbons was studied through thermogravimetric analysis (TGA) in air. Figure 4.2 shows the weight loss and temperature profiles of the activated carbons derived from the three hydrochars. AC 180 represents the activated carbon produced from hydrochar pretreated at 180℃, AC 200 represents the activated carbon produced from hydrochar pretreated at 200℃ and AC 220 the activated carbon produced from hydrochar pretreated at 220℃. A 10mg sample was used for each TGA analysis. Four decomposition phases were observed in this analysis: phase 1 where the sample's moisture evaporated, phase 2 where the volatile components decomposed, phase 3 where the fixed carbon decomposed and the last phase wherein the ash decomposed or parts thereof. Moisture content evaporation for AC 180 was observed around 94℃, around 90℃ for the AC 200 and around 93℃ for the AC 220. An average of 0.71mg (7.53 wt%) mass is lost in this phase. Phase 2 is completed at around 720℃ for all three samples. An average of 1.05mg (11.18 wt%) of volatiles is lost in this phase. Phase 3 is completed at around 1100℃ for AC 180, 1020℃ for AC 200 and 1075℃ for AC 220. An average of 7.59mg (80.81 wt%) of the fixed carbon content is burnt in this phase. The ash phase was observed to lose an average mass of 0.045mg (0.48 wt%) until 1200℃. The total average mass loss being 9.39mg of the 10mg.

The activated carbons decompose over a much wider temperature range of up to about 1200 ℃. The greatest activated carbon yield was observed for AC 220 (11.26 wt%), followed by AC 200 (7.77 wt%) and the lowest yield for AC 180 (7.59 wt%). Phase 2 happens over quite a wide range, starting from 100 to about 720 ℃. Similar to hydrocars, higher yields for this biomass could be realised at temperatures less than 800℃. The activated carbons produced have much higher thermal stability than their precursors and over a wide range, they have much stronger carbon structures and cross-links due to chemical activation.

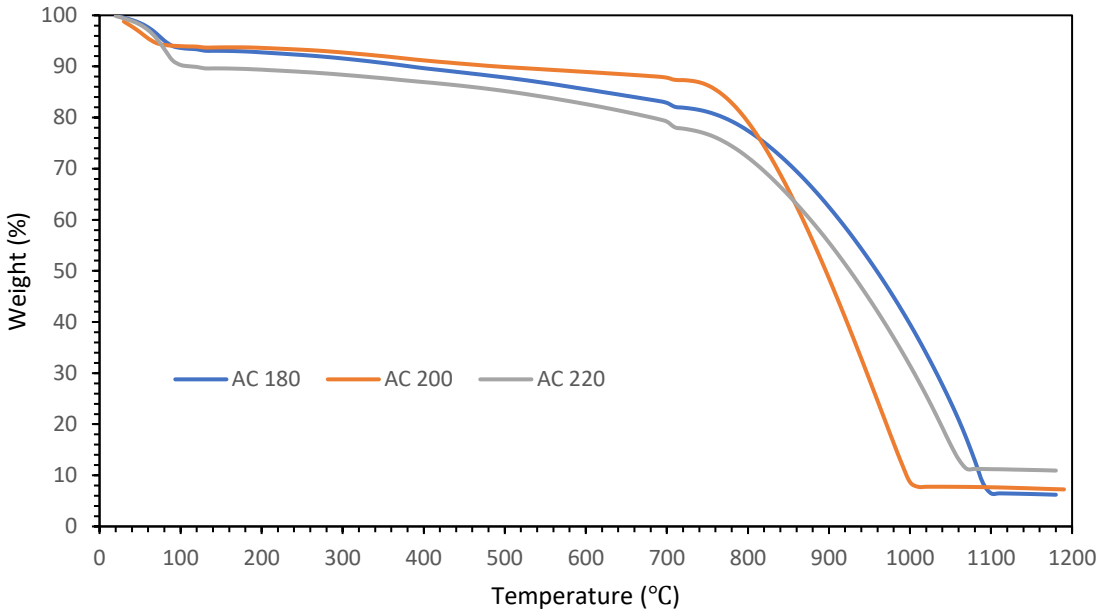

Figure 4.2 Thermogravimetric analysis of activated carbons produced from hydrochars prepared at 180, 200 and 220 ℃

4.2.1 Nitrogen Adsorption Analysis

Nitrogen sorption was used to examine the porosity of avocado waste-derived activated carbons. Figure 4.3 shows nitrogen adsorption isotherms for nitrogen adsorption at 77K. all isotherms show type-IV adsorption behaviour, which is associated with microporous and mesoporous materials. Adsorption happens mostly at low relative pressure and some adsorption happens in the mesopores once the micropores are saturated and further adsorption is observed at relative pressures close to 1, in the highly developed mesoporous and macroporous regions.

Figure 4.3 was used to derive properties of the adsorption, to create figure 4.4. The maximum amount of nitrogen adsorbed ($Q_{ad,\ max}$) was taken from the isotherm. The total pore volume, BET surface area and t-plot derived micropore volume and micropore area (V_{micro} and A_{micro}) were calculated. The pore size distribution, determined using the 2D-NLDFT model, was used to obtain the volume-weighted average pore width (W_{avg}).

Figures 4.3 and 4.4 show that all the activated carbons produced from the avocado waste have improved adsorptive properties with increasing burn-off. The highest burn-off was observed for AC 180, as well as the largest surface area, pore size and other adsorptive properties. This was followed by AC 200, then AC 220, AC 1:2, AC 1:1 and finally AC 700 showing the lowest burn-off and the worst adsorptive properties of the activated carbons.

Overall, the adsorptive properties were enhanced due to the widening of existing pores and the creation of new pores as burn-off increased.

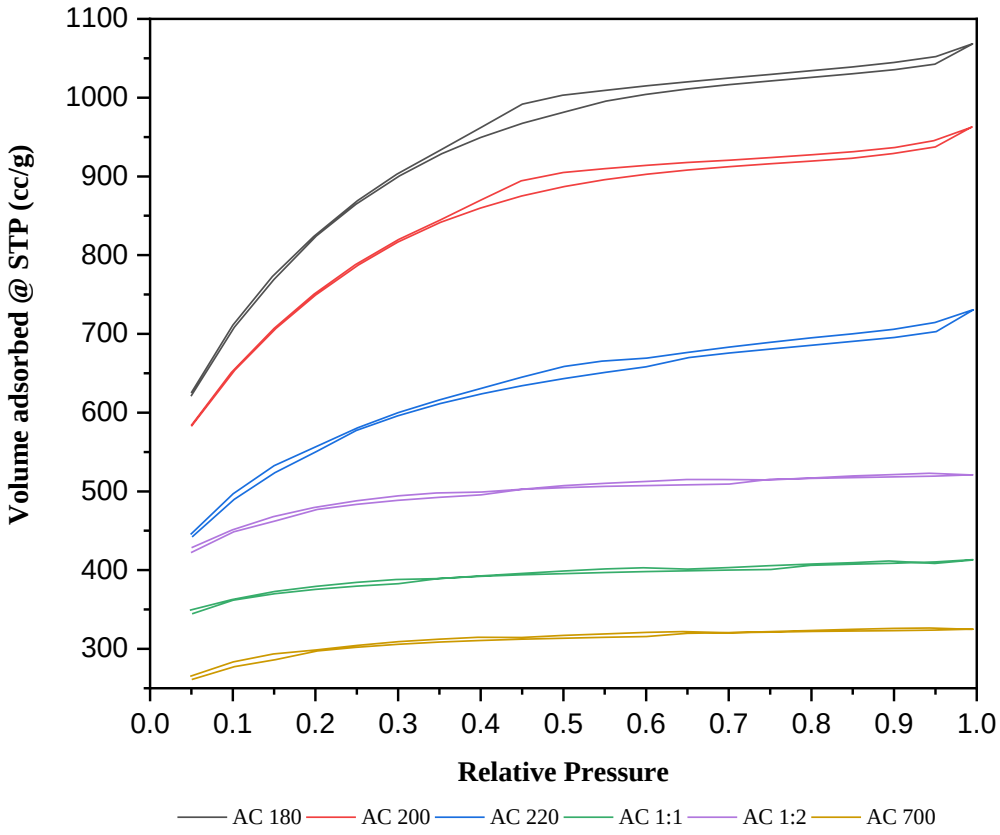

Figure 4.3 Nitrogen sorption isotherms at 77 K on a linear scale for activated carbons

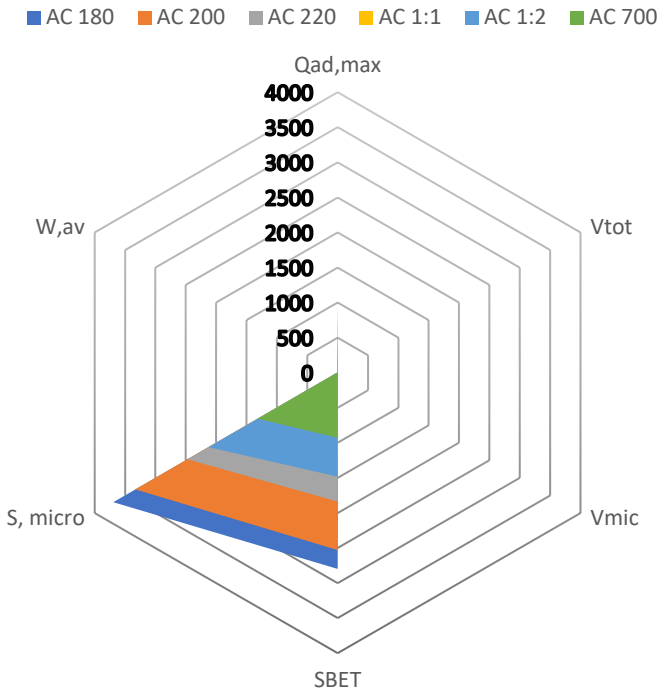

Figure 4.4 comparison of maximum amount of nitrogen adsorbed ($Q_{ad,max}$), the total pore volume (V_{tot}), the micropore volume (V_{mic}), the BET surface area (S_{BET}), the micropore surface area (S_{mic}) and the volume-weighted average pore size (W_{avg}) for activated carbons AC 180, AC 200, AC 220, AC 1:1, AC 1:2 and AC 700

4.2.1.1 Pore Size Distribution (PSD)

The microporosity of the activated carbons produced was further evaluated through a comparison of the micropore volume against the micropore surface area for all the activated carbons. Figure 4.5 shows these comparisons next to each other. The micropore volume of all activated carbons contributes 80.73 to 94.09 % to the total pore volume, V_{tot}. This shows that there are mostly micropores in the activated carbons, though with some really small mesopores but no macropores in the materials. The micropore surface areas of all the activated carbons also contribute between 68.01 and 75.91 % to the BET surface area. Considering burn-off, AC 180 and AC200 with similar burn-off, have similar contributions to the total pore volume and BET surface area from micropores (micro- and mesopores). The AC with lower burn-off: AC 1:1, AC 1:2 and AC 700 make a little bit more of a contribution to the total pore volume and BET surface area through their

micropores (94.09 % and 68.01 %, respectively for AC 1:1). A similar pattern is followed by these activated carbons: higher burn-off results in wider micropores. Burn-off is not a major consideration for these activated carbons.

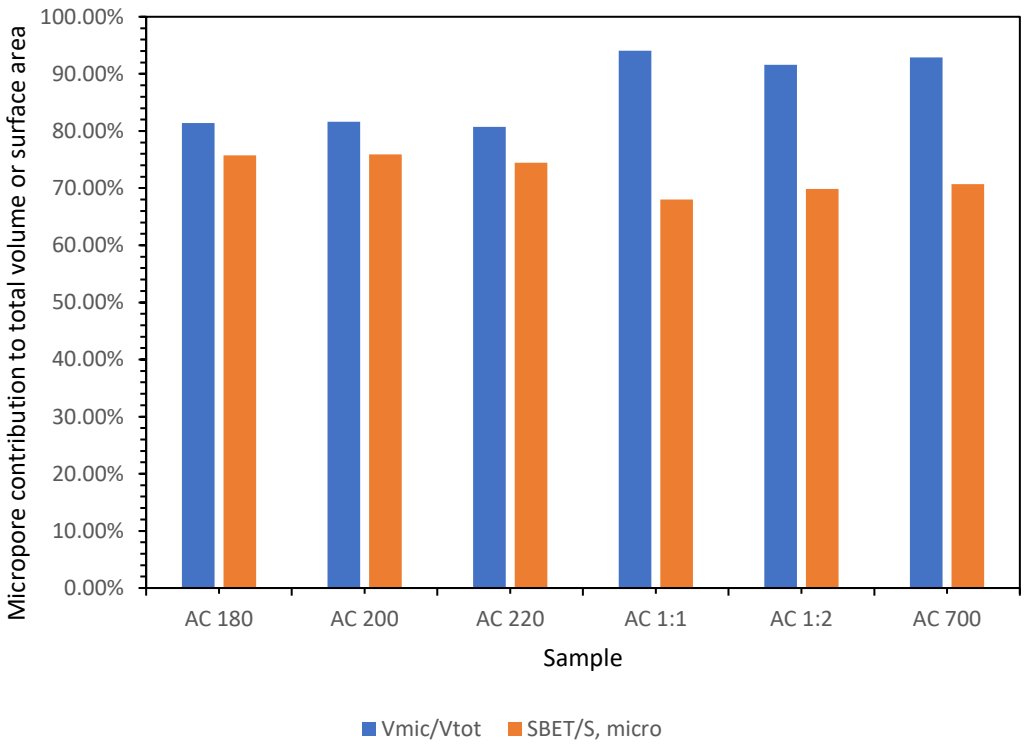

Figure 4.5 Comparison of micropore volume and micropore surface area relative to the total pore volume and BET surface area, respectively.

The behaviour of these activated carbons exhibits similarities, with the majority of the pore volume being attributed to micropores measuring less than 1.15 nm (80%). The activated carbons exhibit slight variations that can be attributed to the methods used in their preparation. The data demonstrates a positive correlation between the concentration of KOH employed in chemical activation and the degree of burn-off. Additionally, it is apparent that increasing the activation temperature, while still below the point of complete burn-off, results in more well defined porosity. AC 180 exhibits a notable contribution (80 wt%) of micropores with a diameter below 1.33 nm, but without any macropores.

The widening of micropores due to burn-off is part to blame for the reduced contribution of ultramicropores (Rowlandson, 2018). In all, the adsorptive properties of the produced activated carbons are quite satisfactory and render activated carbons an attractive adsorbent. High surface areas were obtained. These activated carbons have really high surface areas and narrow porosity.

Figure 4.6 shows the cumulative pore volume and pore volume at STP distributions of the activated carbons, respectively. It can be seen from both curves that the activated carbons have a widespread distribution of pore widths. The pore width ranges between 0.4 nm and 1.98 nm, indicating the presence of micropores only. AC 180 has pore width in the 0.44-1.57 nm range, with more than 20% of its micropores being well developed enough to adsorb nitrogen in the excess of 6000 cm^3/g up to 15 600 cm^3/g. AC 200 has pore width in the 0.41-1.58 nm range, and similar to AC 180, more than 20% of its micropores are well developed enough to adsorb nitrogen in the excess of 6000 cm^3/g up to 14 800 cm^3/g. In fact, its smallest micropores can adsorb relatively more nitrogen than the other activated carbons. AC 220 has pore width in the 0.40-1.58 nm range, with about 50 % of its pore being developed to adsorb more than 8 000 cm^3/g up to 10 872 cm^3/g, unlike AC 180 and AC 200 which have higher distributions of pores that can adsorb that volume. AC 1:1, AC 1:2 and AC 700 show a wider pore width ranging from 0.4 to 1.98 nm, with some of their micropores close to being mesoporous (2 nm). Most of the pores of these three activated carbons can only adsorb just over 5 000 cm^3/g, with AC 1:1's pores peaking at 6 750 cm^3/g, AC 1:2's pores peaking at 9 047 cm^3/g and at 5 645 cm^3/g for AC 700.

A

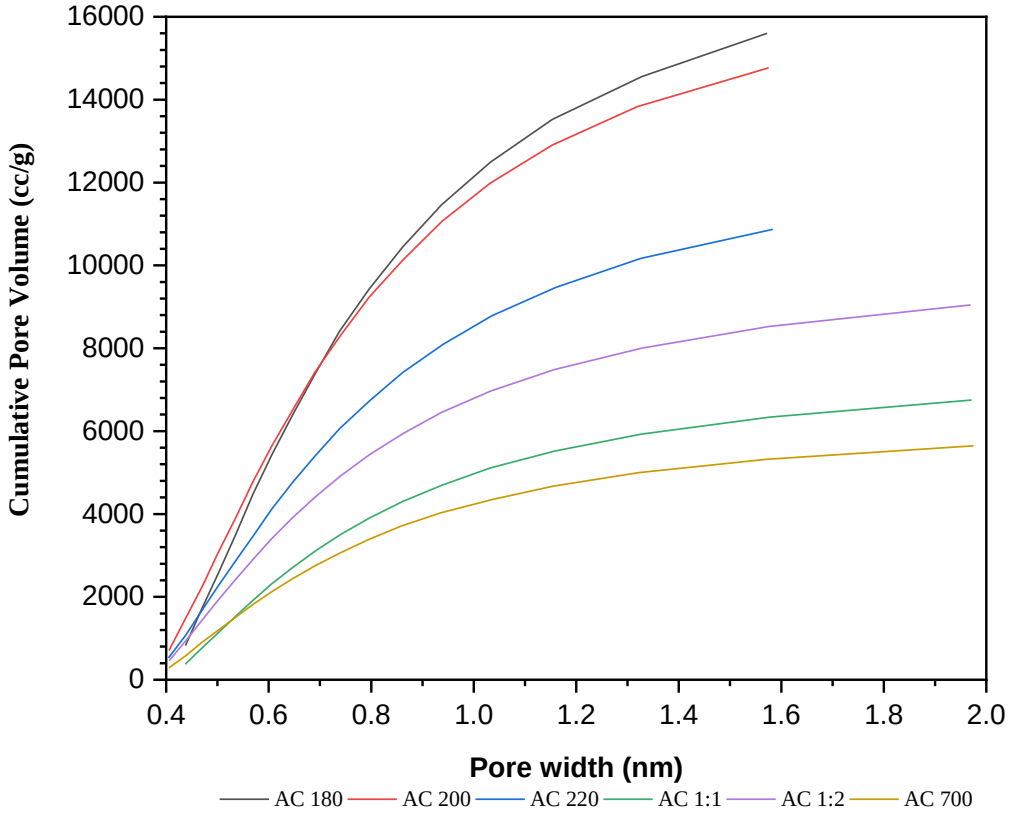
Cumulative Pore Volume (cc/g)
16000
14000
12000
10000
8000
6000
4000
2000
0
0.4
0.6
0.8
1.0
1.2
1.4
1.6
1.8
2.0
Pore width (nm)
AC 180
AC 200
AC 220
AC 1:1
AC 1:2
AC 700

B

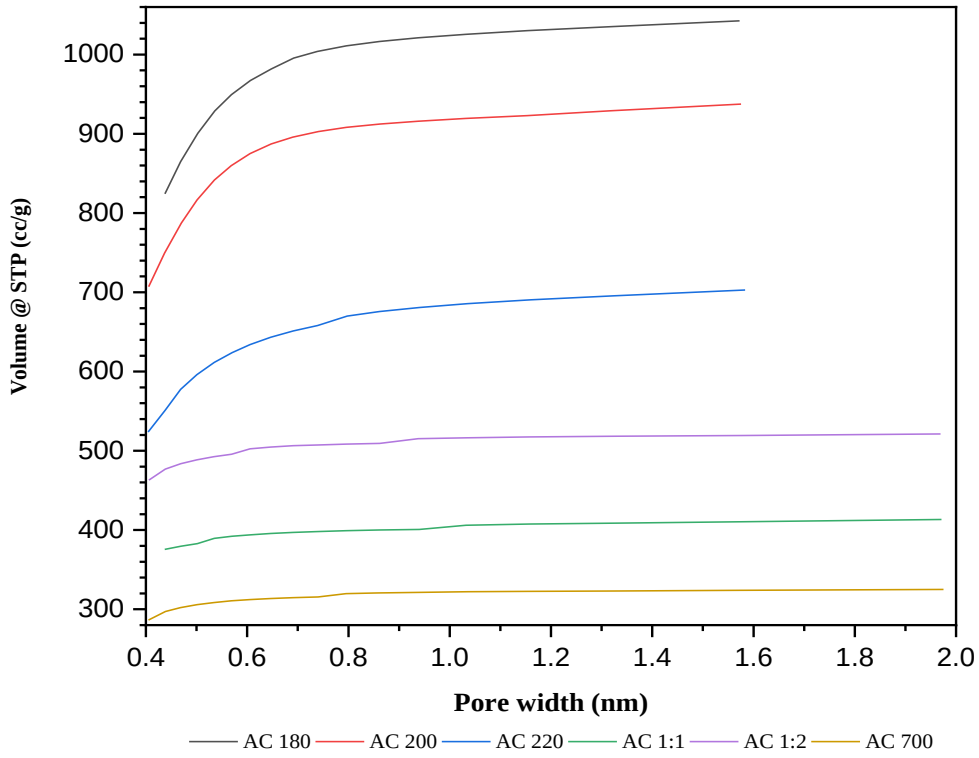

Figure 4.6 (A) cumulative pore volume and (B) volume at STP views of pore size distributions of activated carbons

Most, if not all, of the pores are micropores. Some mesoporous behaviour is observed for AC 1:1, AC 1:2 and AC700. This shows the influence of KOH activation ratio since lower activation ratios were used for AC 1:1 and AC 1:2 than the other AC that were chemically activated at 1:3 ratio. It also clear that activation temperature plays a crucial role in the development of pores since the activated carbon produced at 700 showed less developed micropores than those produced at higher temperatures, 800 ℃ since the sample at 900 ℃ burnt completely.

4.2.2 SEM/EDS Analysis

Figure 4.7 shows an image of hydrochar produced at 200 ℃ and the activated carbon produced from it, this is to visualize the morphology. The scanning electron micrographs of the hydrochars which were used to produce the activated carbons are shown in figure 4.8 and the micrographs of the synthesised activated carbons are in figure 4.9. These micrographs are useful in our analysis

of the shape, size and morphology of the samples. The hydrochars appear to be much smoother than the activated carbons, which also have smooth surfaces with more coarse areas especially in the pores. Figure 4.8 shows somewhat uniform size distribution, clear ornamentation and ridges in the hydrochars. The hydrochars show really small circular voids which are not too obvious. This, according to Rowlandson (2018), indicates a relatively mild synthesis procedure. The pores of the hydrochars are mostly really large, round and well defined. They have pore sizes ranging between 19.95 to about 41.54 μm, with much larger pores being evident. This shows a significant presence of mesopores and somewhat macropores. The hydrothermal pretreatment process improved the pore structure of the avocado waste feed as seen in the resulting hydrochars. However, the pores are not small enough for hydrogen storage applications.

Rough areas, mostly in the pores, are seen for the activated carbons as well. These rough surfaces show that there was void formation in the HTC process (Rowlandson, 2018). Figure 4.9 shows that the pores of the activated carbons produced are much smaller and well developed than those of the hydrochars from which they were produced, and this can be attributed to the chemical activation by potassium hydroxide (Tay *et al.*, 2009). It is evident that higher HC/KOH activation ratios (a-c) lead to larger pores and more improved overall burn-off (Rowlandson, 2019). The samples lost their shape after the activation process, the activated carbons appear irregular and bulky.

Graphitisation is also evident in the activated carbons produced at higher activation ratios and higher temperatures. According to Chung (2016), the increased degree of graphitisation is brought about by tensile or compressive stress acting at the fiber-matrix boundary. However, this graphitisation is not too big to cause a decrease in the specific surface area as we saw in the BET results, thus the pores formed are medium and large enough for storage purposes. Graphitisation also increases the electrical conductivity of the activated carbons produced (Rowlandson, 2019).

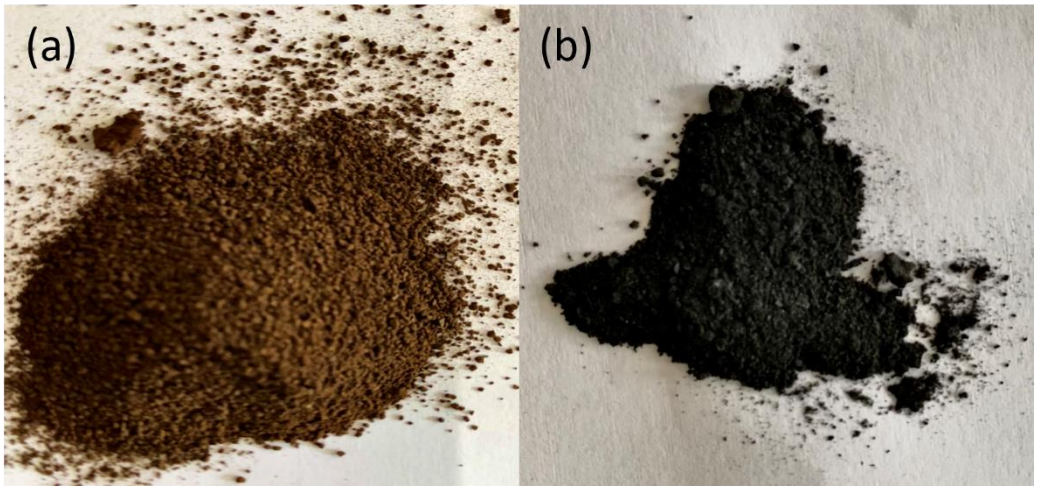

Figure 4.7 An image of the (a) hydrochar produced at 200 ℃ and (b) activated carbon produced from this hydrochar.

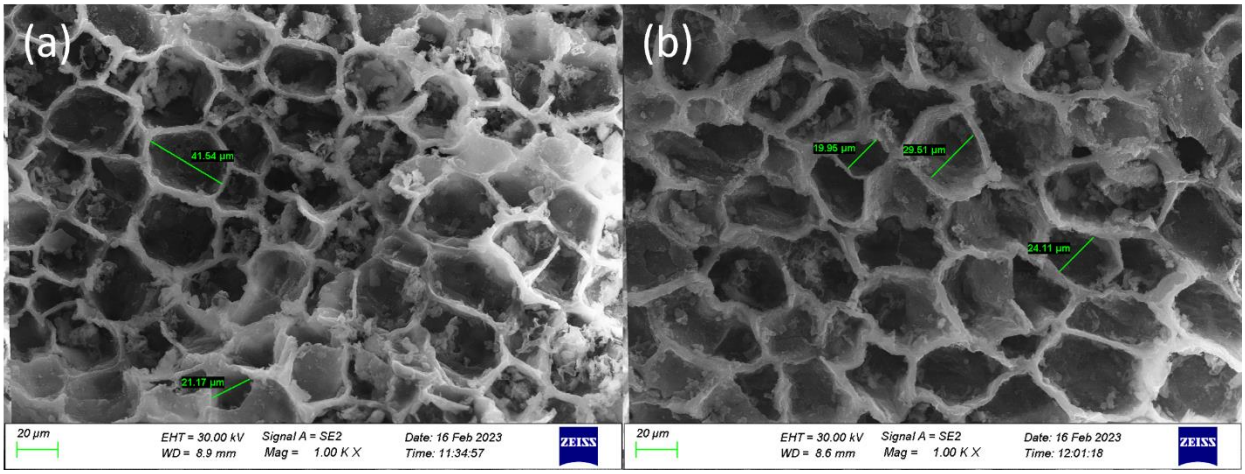

Figure 4.8 SEM images of (a) hydrochar produced at 180 ℃ and (b) hydrochar produced at 200 ℃

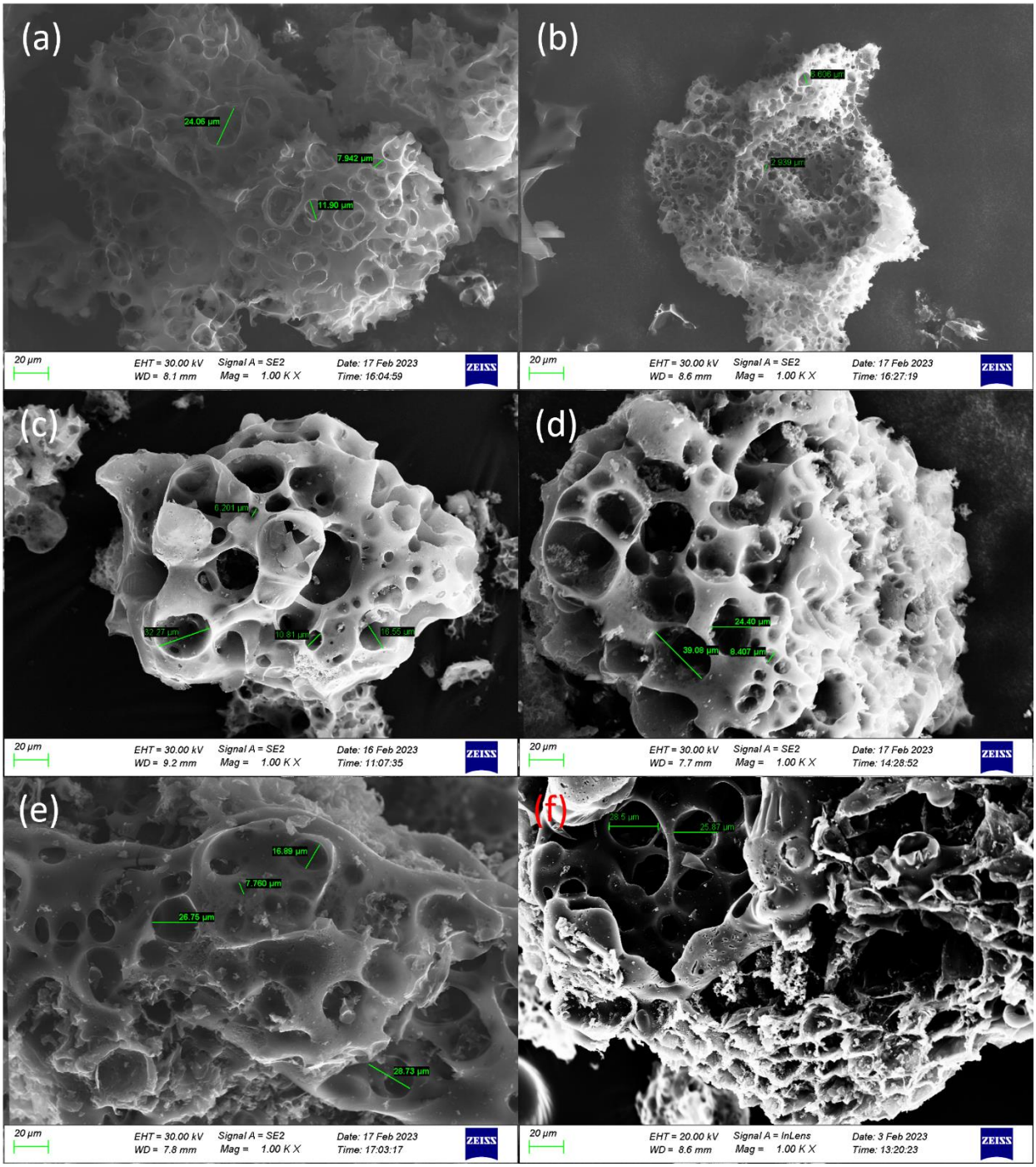

Figure 4.9 SEM images of activated carbons (a) HC 180, (b) HC 200, (c) HC 220, (d) HC 1:1, (e) HC 1:2 and (f) HC 700

4.2.3 XRD Analysis

The activated carbons' structures were evaluated using X-ray diffraction. The XRD profiles of the activated carbons from each phase are represented in figures 4.10, 4.11 and 4.12.

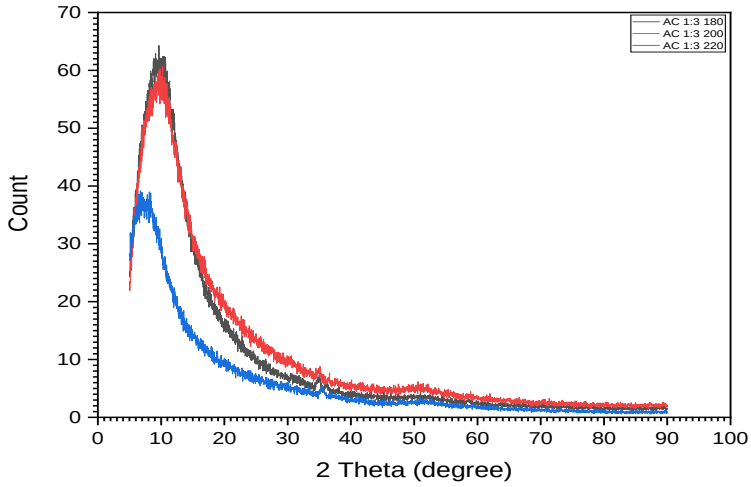

Figure 4.10 XRD profiles of activated carbons produced from different hydrochars at the same KOH ratio and activation temperature, AC 180, AC 200 and AC 220

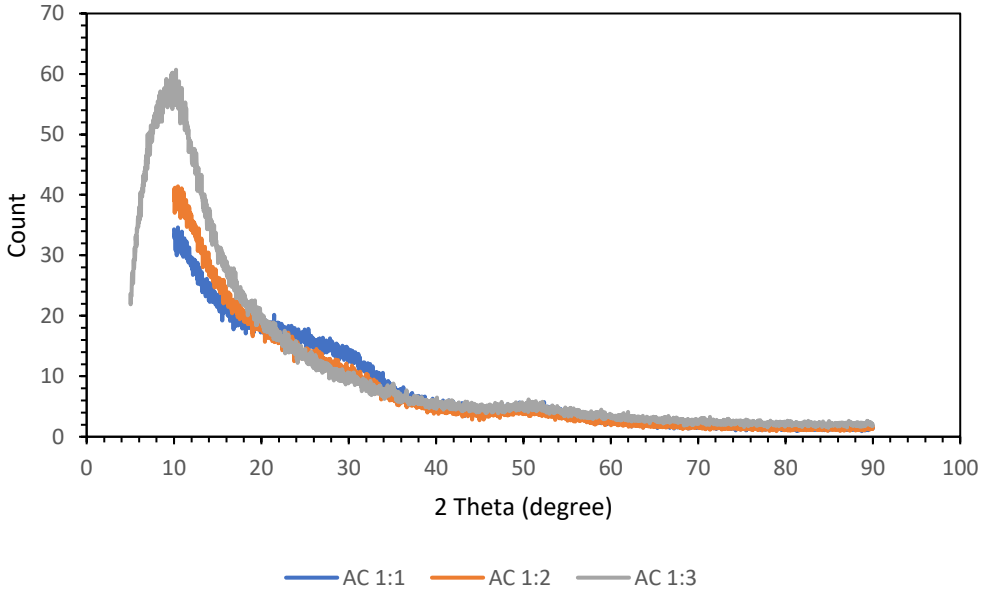

Figure 4.11 XRD profiles of activated carbons produced at different KOH activation ratios (1:1, 1:2 and 1:3) AC 1:1, AC 1:2 and AC 200. AC 200 is the same as AC 1:3

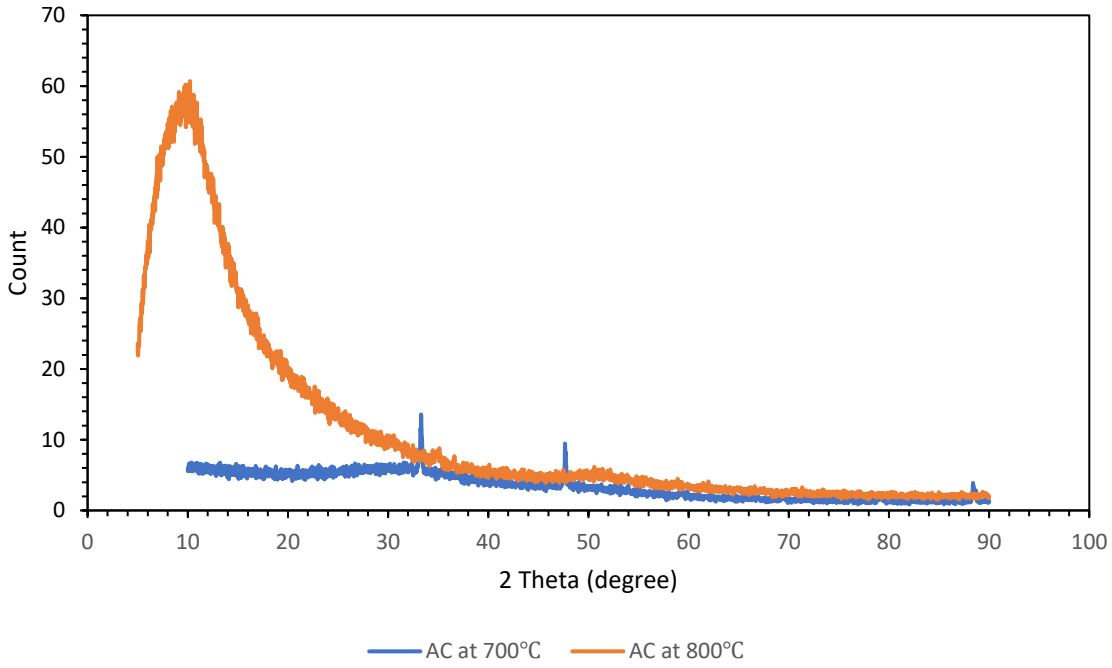

Figure 4.12 XRD profiles of activated carbons produced at different activation temperatures; 700°C and 800°C

In the activated carbons, figures 4.10 to 4.12, the reflection bands are seen to 2θ at three sites:10°, 36° and 51°, respectively. The sharp peak at 2θ = 10° shows a highly graphitised sample part and the broader peaks at 2θ = 36° and 51° show the disordered amorphous carbon form (Girgis *et al.*, 2007: Karakehya, 2023). High intensity or count is seen at 10°, reflecting the highest number of molecules in this phase, with the spacing. The sharp peak also indicates some level of graphitisation (Rowlandson, 2019). Reflection bands are observed to 2θ at 33° and 47° for AC 700. These bands reflect a more amorphous carbon. The activated carbon at 700 °C was not fully activated and its porosity is not well developed.

The XRD profiles for hydrochar pretreated at 200 °C and the activated carbon produced from it at 1:3 KOH activation ratio at 800 °C were smoothed to determine the FWHMs. The COD (R^2) value obtained for the hydrochar after 19 convergence iterations is 0.98, which is close to 1. The COD (R^2) value obtained for the activated carbon prepared from the same hydrochar after 35

convergence iterations is 0.9944, which is close to 1. Eight peaks were identified and fitted for the hydrochar whereas only three peaks were identified and fitted for the activated carbon. The Scherrer equation was used to calculate the crystalline size:

$$D = \frac{K\lambda}{\beta \cos\theta} \quad (1)$$

Where D is the crystallites size (nm), K represents 0.9 (Scherrer constant), $\lambda = 1.78899\dot{A} = 0.178899\, nm$ (wavelength of the X-ray source), $\beta =$ is the FWHM (radians) and θ represents peak position (radians)

The peak position and FWHM was determined from the XRD data. Tables 4.3 and 4.4 show the peak positions and FWHM data used to calculate the crystallite sizes, for the hydrochar and activated carbon, respectively. The average crystallites size of the hydrochar before activation is 32.23 nm. The average crystallites size of the activated carbon is 0.79 nm.

Table 4.3 Peak position, FWHM and crystallite size data for the hydrochar prepared at 200°C

Peak position (2 Theta)	**FWHM**	**Crystallite size D (nm)**
52.2206	0.2504	41.0303
61.0856	0.3737	28.6637
22.3553	0.6639	14.1636
45.0819	0.5609	17.8090
46.9776	0.1827	55.0584
38.6485	0.2686	36.3998
69.8815	0.3258	34.5427
74.4142	0.3834	30.2090

Table 4.4 Peak position, FWHM and crystallite size data for the activated carbon produced at 1:3 KOH ratio, at 800℃ from the HC prepared at 200℃

Peak position (2 Theta)	FWHM	Crystallite size D (nm)
9.6432	7.4103	1.2493
13.2952	27.5859	0.3367

The diffraction peaks of the activated carbons are more asymmetrical in comparison to those of the avocado waste or hydrochar. As the crystallite size decreases, Misture and Snyder (2001) noted that destructive interference near the Bragg angle decreases and the diffraction peak widens. Another important observation is that the major diffraction peaks for AC 180 and AC 200 had higher counts of about 62, AC 220 had a count of about 38, AC 1:1 a count of 32, AC 1:2 a count of 40 and AC 700 a count of 12. The higher count or intensity for AC 180 and AC 200 reflect the increased porosity while the lower intensity reflects less developed porosity. It should also be noted that the peaks are not very sharp, indicating that the activated carbons produced from avocado waste are mostly amorphous.

4.2.4 FTIR Analysis

The FTIR spectra of the activated carbons produced are presented in figure 4.13. It can be seen that the activated carbons produced at similar KOH activation ratio, 1:3, show similar patterns and bands thus indicating similar functional groups (AC 180, AC 200 and AC 220). The activated carbons produced at 1:1 (AC 1:1), 1:2 (AC 1:2) KOH ratios as well as that produced at 1:3 KOH ratio but at 700 ℃ (AC 700) show different functional groups. In the case for KOH activation at lower ratios, 1:1 and 1:2, the patterns are similar to each other and reflect less clearer bands though similar to those for higher KOH activation ratios.

In the similar patterns and bands shown by AC 180, AC 200 and AC 220, the band at 2850 cm^{-1} represents the N-H stretching vibration group, 1750 cm^{-1} peak represents C=O stretching vibration, 1600 cm^{-1} peak represents the C=C stretching vibration, 1500 cm^{-1} peak represents the N-O

stretching vibration, 1450 cm^{-1} peak represents the C-H bending vibration, the 1300 cm^{-1} and 1100 cm^{-1} peaks represent the C-O stretching vibration, the 700 cm^{-1} peak represents the C=C bending vibration (Tay *et al.*, 2009; Gao *et al.*, 2015; Feng *et al.*, 2021). The 1500 cm^{-1} and 2850 cm^{-1} peaks which represent the N-O stretching vibration and the N-H stretching vibration group, respectively, are observed for AC 1:1 and AC 1:2, though not very clear. AC 700 also shows the presences of N-O stretching vibration. The peaks for these samples are not well defined, clearly visible peaks but we can still see the functional groups from these profiles.

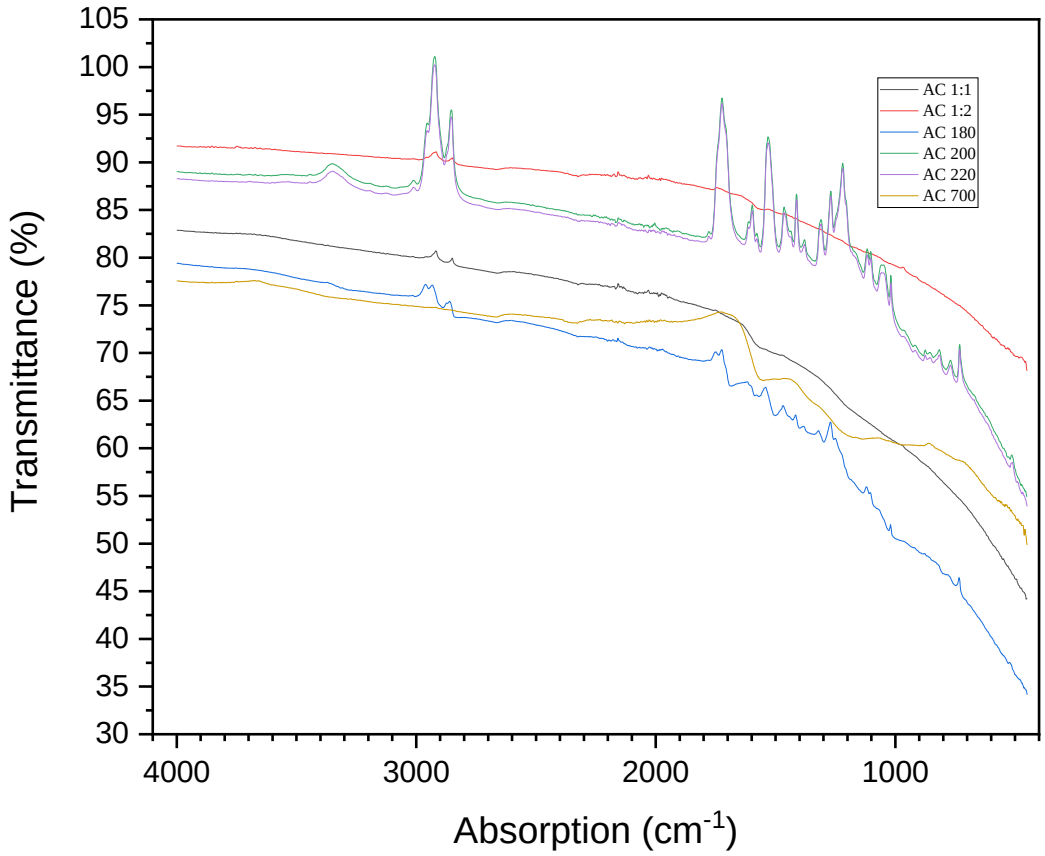

Figure 4.13 FTIR profiles of activated carbons.

The FTIR analysis confirmed the presence of oxygen containing groups; C=O, N-O, and C-O which act as the active sites that interact with molecules nearby and aid in hydrogen adsorption

(Gao *et al.*, 2015; Feng *et al.*, 2021). The activated carbons have a higher proportion of C=C stretching and bending vibrations, but most of the functional groups are stretching.

4.3 ADSORPTION PROPERTIES OF HYDROGEN ONTO THE ACTIVATED CARBONS

4.3.1 Measurement of Adsorbents Properties, adsorption isotherms and isotherm model

Hydrogen storage capacity of activated carbons was evaluated by analysing the hydrogen uptake of the activated carbons at 77 K up to 1 bar. The results were compared to analysis of industrial activated carbons in literature. The volumetric uptake of hydrogen is shown in figures 4.14 and 4.15, and table 4.5 shows the uptake values. Figure 4.14 shows the data for all the activated carbons in mol/kg and figure 4.15 in cc/g. Hysteresis between adsorption and desorption branches of the isotherms is observed for the synthesised activated carbons. This means that hydrogen adsorption is irreversible. The activated carbons show uptake values of between 0.16 and 9.59 mol/kg, which translates to between 3.5 and 25.00 wt%. The volumetric uptake of AC 180 is higher than that of all activated carbons produced but its gravimetric uptake is less than that of AC 200 and some of the activated carbons. According to Rowlandson (2018), the uptake of industrially produced TE7 was 2 wt%, which was similar to then reported hydrogen uptake values for it.

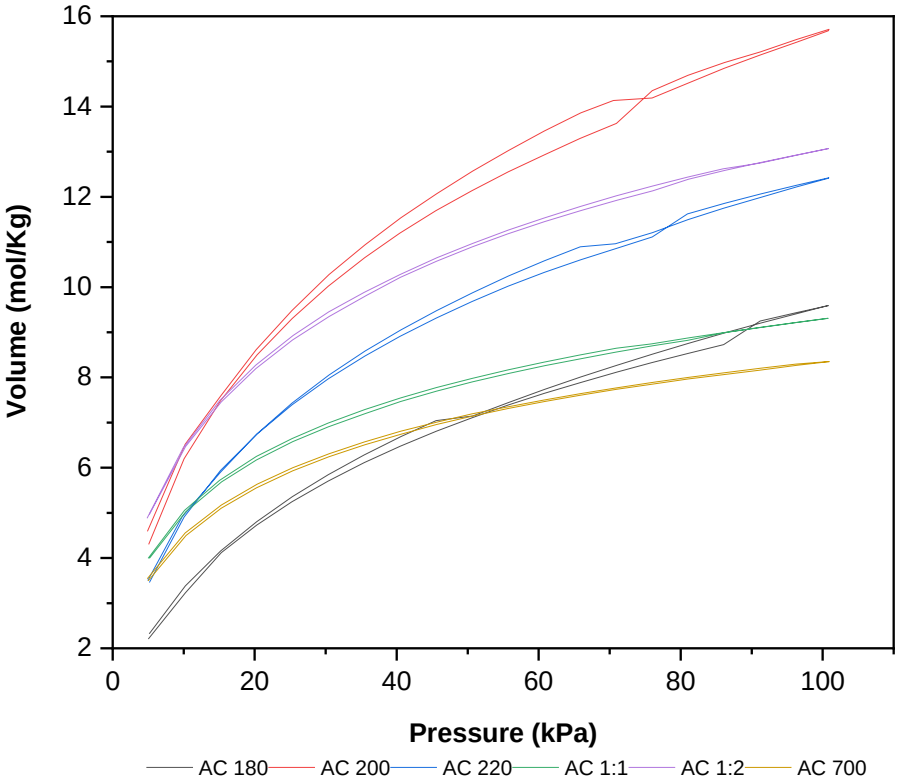

Figure 4.14 Hydrogen sorption isotherms showing the volumetric (mol/kg) uptake at 77 K in AC180, AC 200, AC 220, AC1_1, AC1_2 and AC700

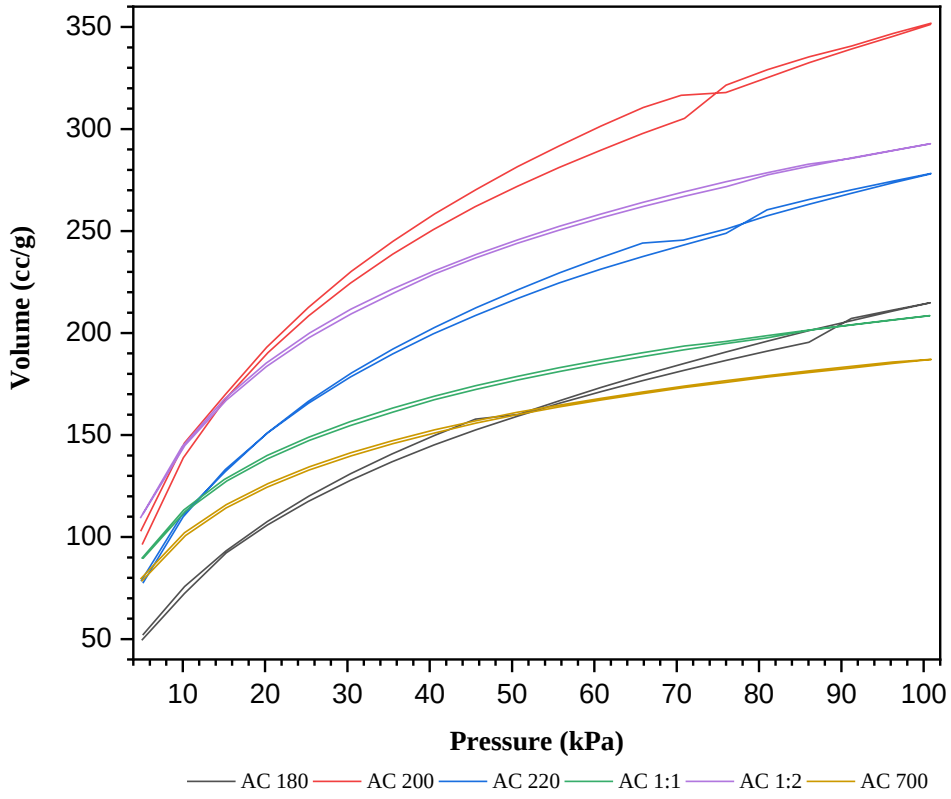

Figure 4.15 Hydrogen sorption isotherms showing the volumetric uptake at 77 K in AC180, AC 200, AC 220, AC1_1, AC1_2 and AC700

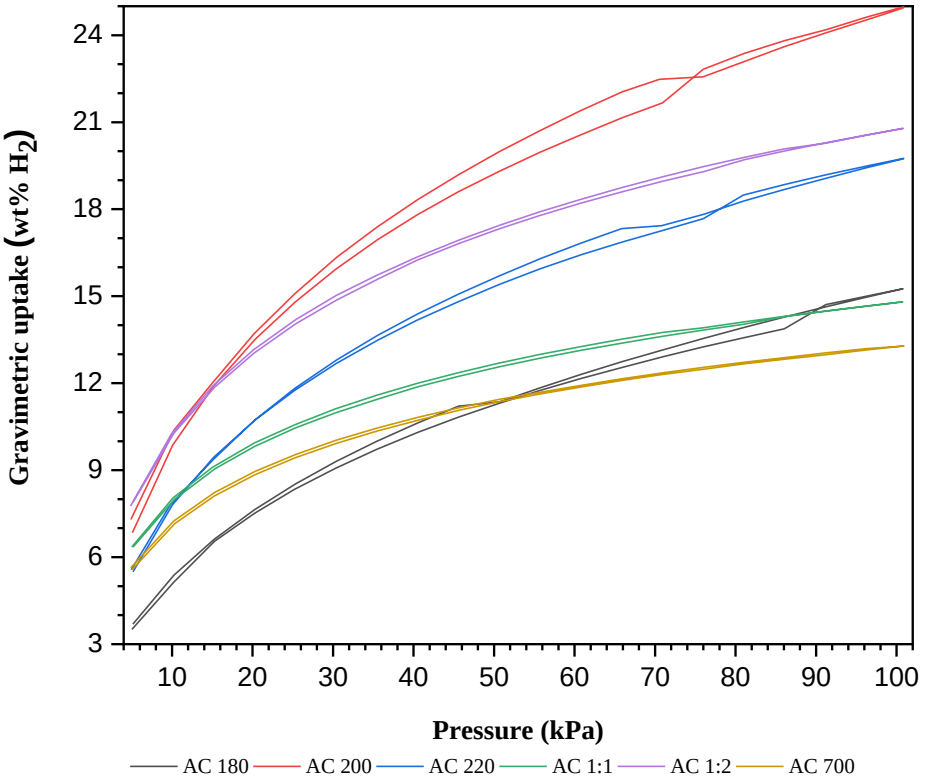

Figure 4.16 Hydrogen sorption isotherms showing the gravimetric uptake at 77 K in AC180, AC 200, AC 220, AC1_1, AC1_2 and AC700

Minimal variance is observed among activated carbons obtained from various hydrochars, however considerable variation is noticeable for those produced from the same hydrochar but subjected to varied activation conditions. The samples exhibiting minimal variance in hydrogen uptake demonstrate similar interactions between hydrogen molecules and their respective pore structures. The main reason for this can be attributed to the comparable pore size distributions, as depicted in figure 4.6, and the similar proportions of micropores, with diameters smaller than 4.00 nm, in relation to the overall pore volume. The hydrogen adsorption isotherms shown in this study align with the findings reported in nitrogen sorption experiments, indicating that the activated carbons formed from different hydrochars exhibit similar porosities. Certain differences are discernible, however lacking in significant intensity.

AC 200 has the highest gravimetric hydrogen uptake. This is in part due to the well-developed micropores seen in the PSD. This activated carbon also has the highest micropore surface area and pore volume in comparison to activated carbons produced under different conditions. The maximum gravimetric uptake of each activated carbon sample as well as its micropore volume and surface area are shown in figure 4.17 for comparison. AC 200 has the highest surface area and micropore volume, thus the highest hydrogen uptake, though AC 180 has higher micropore volume and micropore surface area contributions. AC 700 which has the lowest adsorptive properties has, similarly, the lowest hydrogen uptake at 77 K.

Figure 4.18 shows a comparison of the gravimeric hydrogen uptake at 77 K and 1 bar for all activated carbons against their surface areas. It can be seen that these surface areas are relatively higher than those observed for activated carbons that were produced without KOH chemical activation (Rowlandson, 2018). A comparison between AC 1:1, AC 1:2 and AC 200 (same as AC 1:3) shows that KOH activation produces ultrahigh surface areas since the surface area of AC 1:1 is smaller than that of AC 1:2 which is also smaller than that of AC 200. These are activated carbons produced at varying KOH weight ratios, 1:1, 1:2 and 1:3, respectively. The micropores of the activated carbons produced at higher KOH concentrations are also relatively more well developed than those of the activated carbons produced at lower KOH concentrations. The highest hydrogen uptake (24.98 wt%) is observed for AC 200, which is the one that was chemically activated with the highest KOH concentration (1:3).

Some of the hydrogen uptake data recorded in literature for activated carbons include lignin hydrochars produced by Sangchoom and Mokaya (2015), which had a maximum surface area of 3235 m^2/g. This was the highest recorded for lignin-derived activated carbons (Rowlandson, 2018). Hydrogen uptake between 3.2 and 5.2 wt% at 20 bar was recorded for this sample (Sangchoom and Mokaya, 2015). The activated carbons produced in this study have much higher gravimetric uptake.

Table 4.5 Adsorptive properties reported in literature (Rowlandson, 2018; Sangchoom and Mokaya, 2015; Cheng *et al.*, 2008)

Activated Carbon	Gravimetric H_2 uptake (wt%)
RLAC	1.7 ± 0.2
FLAC	1.7 ± 0.2
HLAC	1.6 ± 0.2
ELAC	1.8 ± 0.2
TE7	2.0 ± 0.1
Lignin-derived (a)	3.2
Lignin-derived (b)	5.2

The broadening of pore size distribution was attributed as the primary reason for a reduced hydrogen uptake efficiency by Cheng *et al.* (2008). They further noted that the high surface area of the carbons nullified this microporosity reduction.

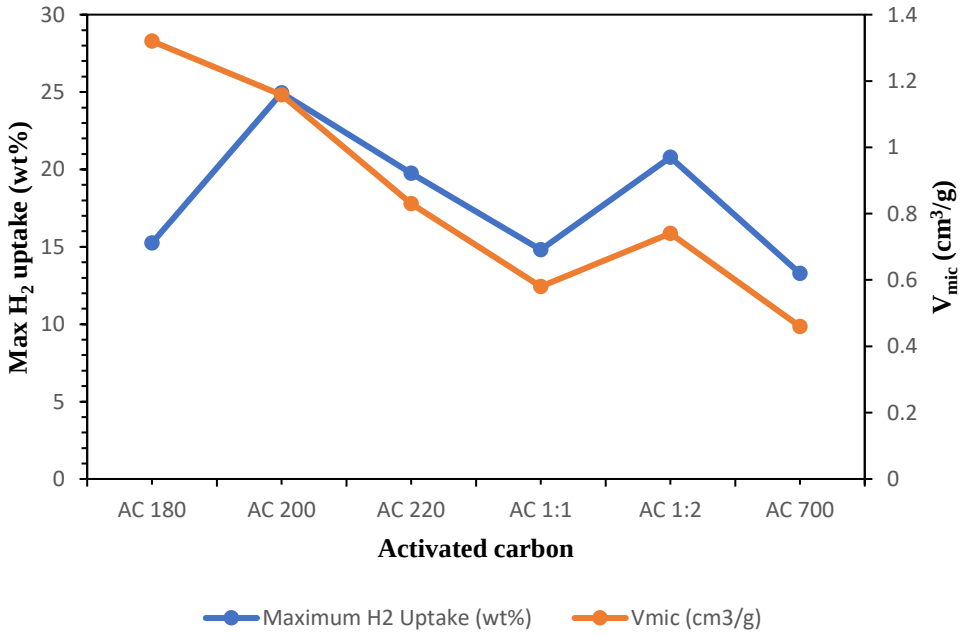

Figure 4.17 Maximum gravimetric hydrogen uptake vs micropore volume for AC 180, AC 200, AC 220, AC 1:1, AC 1:2 and AC 700

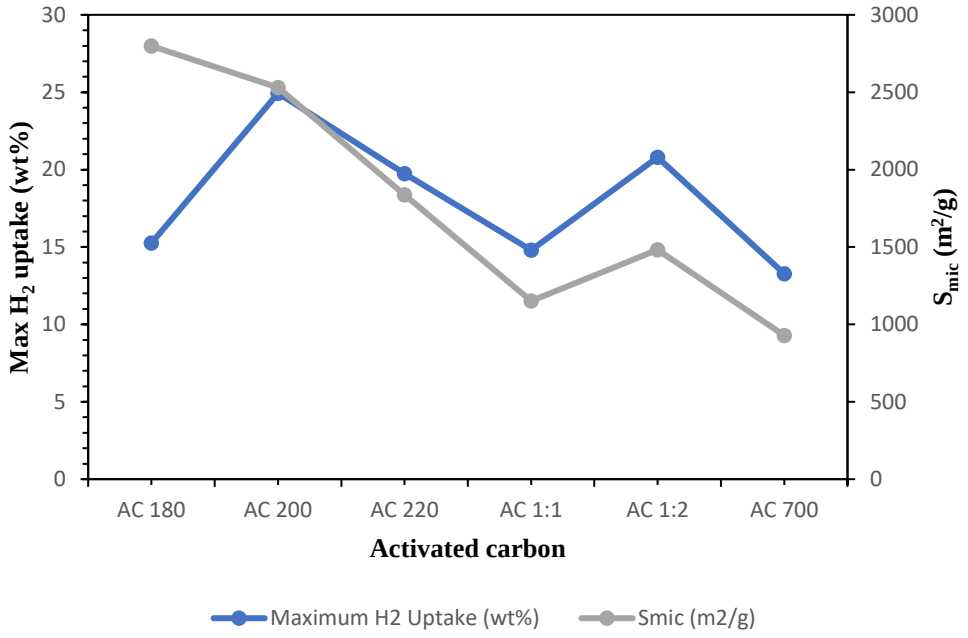

Figure 4.18 Maximum gravimetric hydrogen uptake vs micropore surface area for AC 180, AC 200, AC 220, AC 1:1, AC 1:2 and AC 700

Figures 4.17 and 4.18 show that there is a correlation between maximum hydrogen uptake and micropore volume as well as micropore surface area for the activated carbons. These maximum gravimetric uptake values are generally higher than those reported in literature as per table 4.5. They are also in line with the DOE requirements.

4.4 MODELLING OF HYDROGEN ADSORPTION ONTO ACTIVATED CARBON

4.4.1 Model Development

The development of the universal adsorption isotherm model by Ng *et al.* (2017) was motivated by the limitations of current models, which were unable to universally represent gas adsorption for all materials while also considering their energy locations. The efficacy of popular models lies in their ability to effectively describe and portray specific regions of adsorption isotherms or gas behaviour. However, many models exhibit limitations in capturing behaviour that falls outside of these regions, such as the Henry's Law region. Further elaboration regarding this topic can be found in section 2.8.

4.4.2 Model Assumptions

The model assumes a number of homogenous sites to characterize the heterogeneous surface. The heterogeneous surface of the adsorbent was modelled by smaller homogeneous surfaces that are assumed to have the same energy levels. Each homogeneous surface was defined through the adsorption site energy's energy distribution function (EDF).

4.4.3 Governing Equations

The equations governing this model and the significance of the parameters are covered under section 2.8.

4.4.4 Discussion

The universal isotherm model is a type of Monte Carlo simulation developed for sorption modelling. It is also used to calculate the energy of adsorption for each site. Experimental data obtained from the experimental work done and discussed in the previous sections was used to evaluate the model.

A number of isotherm models were tested using the experimental data but a few challenges were experience in that some of the models that could predict the adsorption isotherms were not robust enough for complex regions and did not give the energy of adsorption for each site. The universal isotherm model for 3 sites, UNIV4, was used. This was also seen as appropriate based on other analysis carried out in terms of hydrogen sorption.

Hydrogen heat of vaporisation used in this model is 449.36 J/mol. Two-terms were used for modelling all activated carbons (Ng *et al.*, 2007).

AC 180

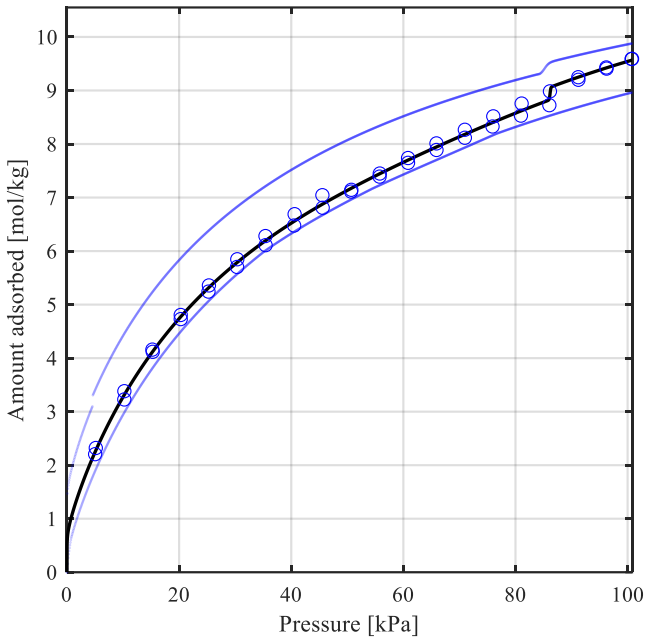

(a)

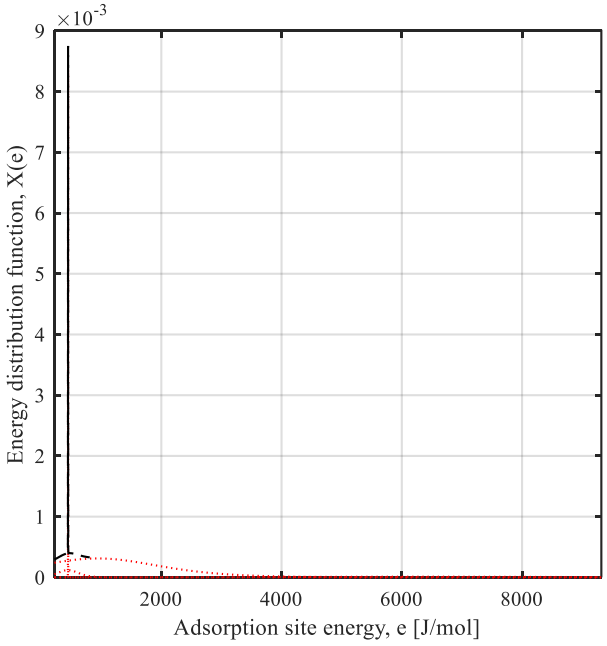

(b)

Figure 4.19 Predicted and measured data for AC 180 (a) adsorption isotherm and (b) the corresponding adsorption sites energy distribution. The curve with rings in (a) shows the

experimental data points while the blue lines without rings show the universal isotherm model predictions.

Figure 4.19 (a) shows that AC 180 exhibits type-IV isotherm. This isotherm is characterized by a rapid increase in the amount of hydrogen adsorbed between 0 and about 86 kPa as the pressure increases, with almost two saturation points or levels being reached. The first pseudo-saturation would be observed between 60 and 80 kPa. Thereafter, we can see a rapid rise or shift in adsorption at pressures above 85 kPa. This shows the multilayer formation during adsorption at this pressure for AC 180. Due to the pressure used in this analysis, we cannot see the actual saturation points. This indicates a well developed porosity if the pores are still able to adsorb so much hydrogen at such pressures. Only a fraction of the mesopores seems to be evident here, the majority of adsorption occurs at the micropores. The curve with rings shows the experimental data points while the blue lines without rings show the universal isotherm model predictions.

The energy distribution function, figure 4.19 (b) shows a non-symmetrical single peak which is something only seen in type-IV adsorption according to Ng *et al.* (2017). Most of the surface coverage occurs at low pressures, with this region having the highest probability distribution of energy sites. It is also clear that these sites do not require a lot of energy for hydrogen sorption, requiring less than 2000 J/mol for most parts of the gas sorption and slightly above the 300-400 J/mol being the most dominant energy site requirements. The apparent mesoporous layer in the multilayer formation does not seem to require much adsorption energy and does not have a significant energy site distribution. This could indicate that these are not true mesopores but micropores with higher pore widths as seen in the PSD.

AC 200

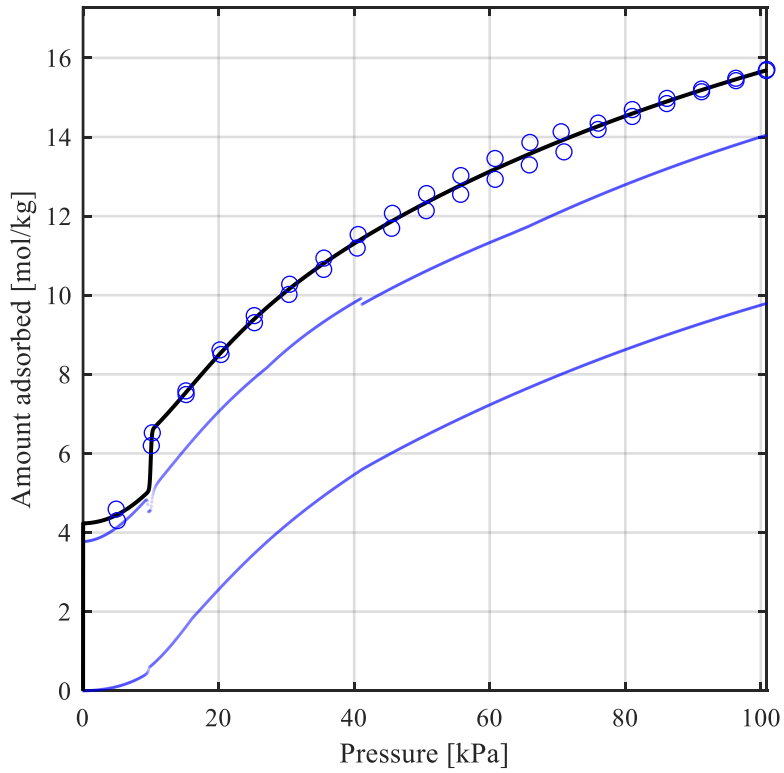
Amount adsorbed [mol/kg]
Pressure [kPa]
0
2
4
6
8
10
12
14
16
0
20
40
60
80
100

(a)

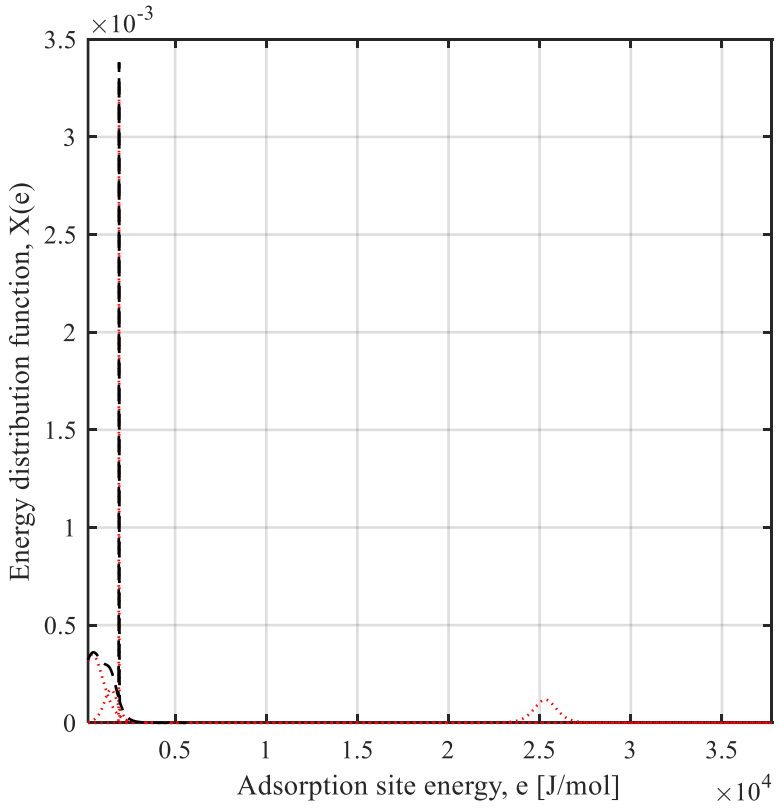

(b)

Figure 4.20 Predicted and measured data for AC 200 (a) adsorption isotherm and (b) the corresponding adsorption sites energy distribution. The curve with rings in (a) shows the experimental data points while the blue lines without rings show the universal isotherm model predictions.

Figure 4.20 (a) shows that AC 200 exhibits type-V isotherm. This isotherm has a unique S-shape. It is characterized by three different uptake rates. There is a smooth uptake at low pressures, between 0 and about 10 kPa, followed by a rapid horizontal increase in the amount of hydrogen adsorbed at 10 kPa and a subsequent steep increase of adsorption with increasing pressure, though not as steep as at 10 kPa. This subsequent uptake then goes on to level off at higher pressures, but we cannot see that saturation due to the pressures used in this research. This also indicates a well developed porosity if the pores are able to adsorb so much hydrogen at such pressures.

Figure 4.20 (b) shows a type-V characteristic energy distribution function with higher probability peak of the energy distribution function seen at lower energy sites which also indicate most surface coverage occurs at lower concentrations (Ng *et al.*, 2017). It is also interesting to note that there are two apparent peaks with the last peak showing very small probability of energy sites, though an important amount of adsorption site energy of about 25 000 J/mol at higher pressures.

AC 220

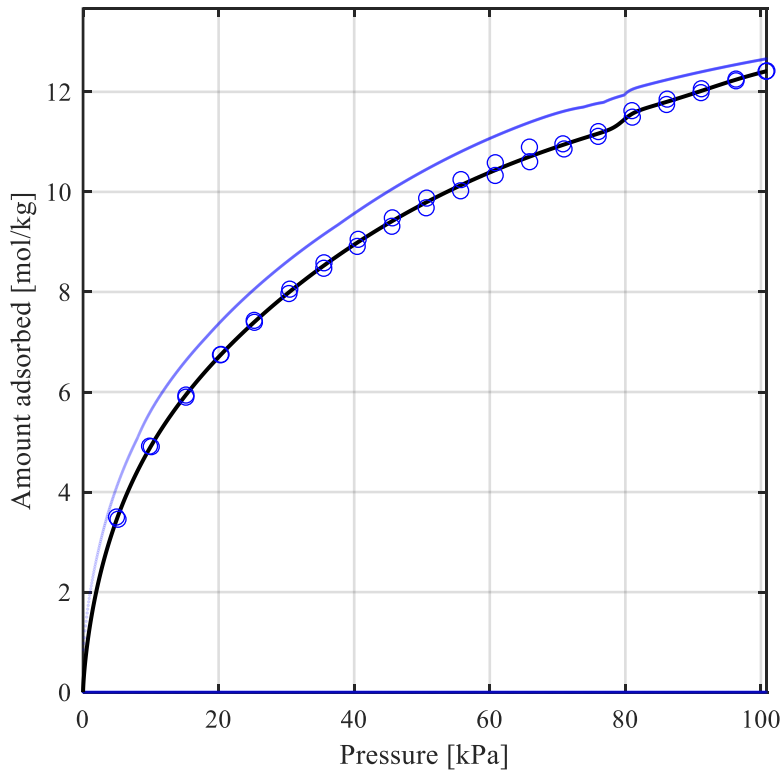

(a)

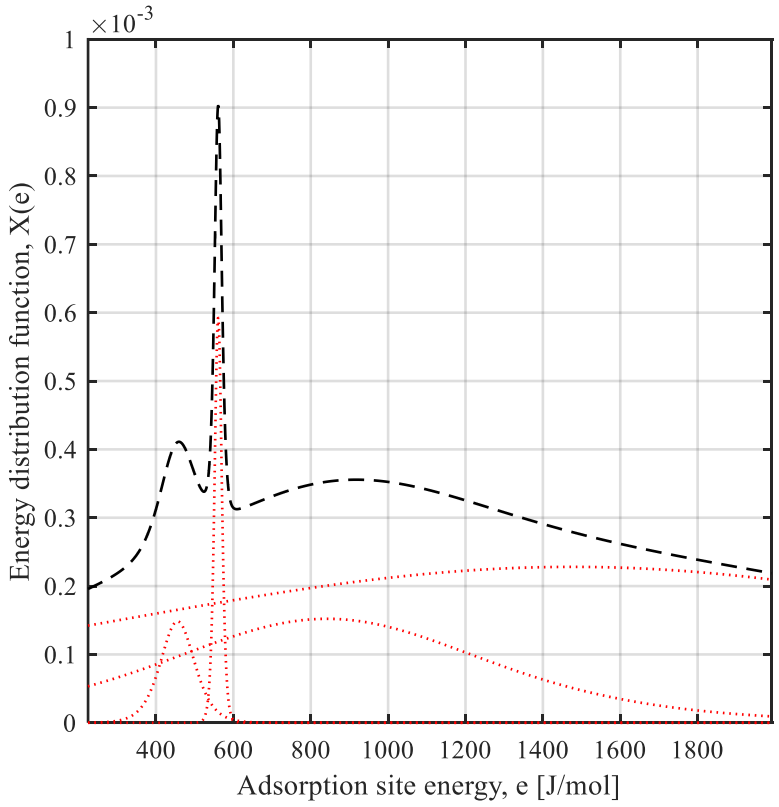

(b)

Figure 4.21 Predicted and measured data for AC 220 (a) adsorption isotherm and (b) the corresponding adsorption sites energy distribution. The curve with rings in (a) shows the experimental data points while the blue lines without rings show the universal isotherm model predictions.

Figure 4.21 (a) here shows that AC 220 exhibits type-IV isotherm, similar to AC 180. There is a rapid increase in the amount of hydrogen adsorbed between 0 and about 77 kPa as the pressure increases, with almost two saturation points or levels being reached as well. The first pseudo-saturation would be observed between 60 and 78 kPa. Thereafter, we can see a rapid rise in adsorption at pressures above 82 kPa. This shows the multilayer formation during adsorption at this pressure for AC 220. This indicates a well-developed porosity with only a fraction of the mesoporous layer contributing to hydrogen adsorption, the majority of adsorption occurs at the micropores. It could also indicate wider micropores and not a real mesoporous layer.

The energy distribution function in figure 4.21 (b) shows a rather interesting non-symmetrical peak at the lower concentration/pressure end of the distribution. We can see that lower adsorption energy sites exist for this AC overall, ranging between 0 and just over 1800 J/mol. Adsorption happens easily in the lower pressure region for this activated carbon.

AC 1:1

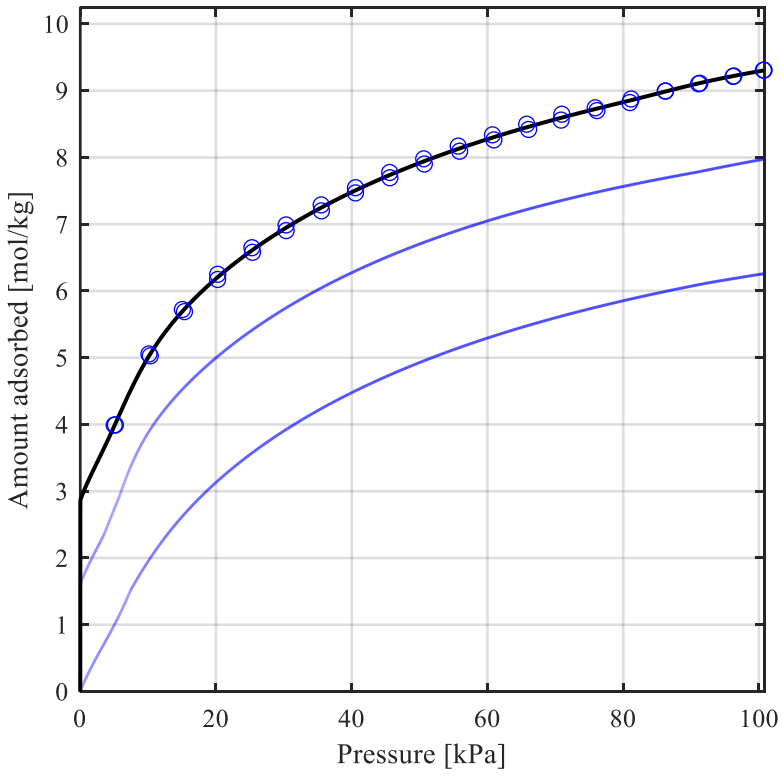

(a)

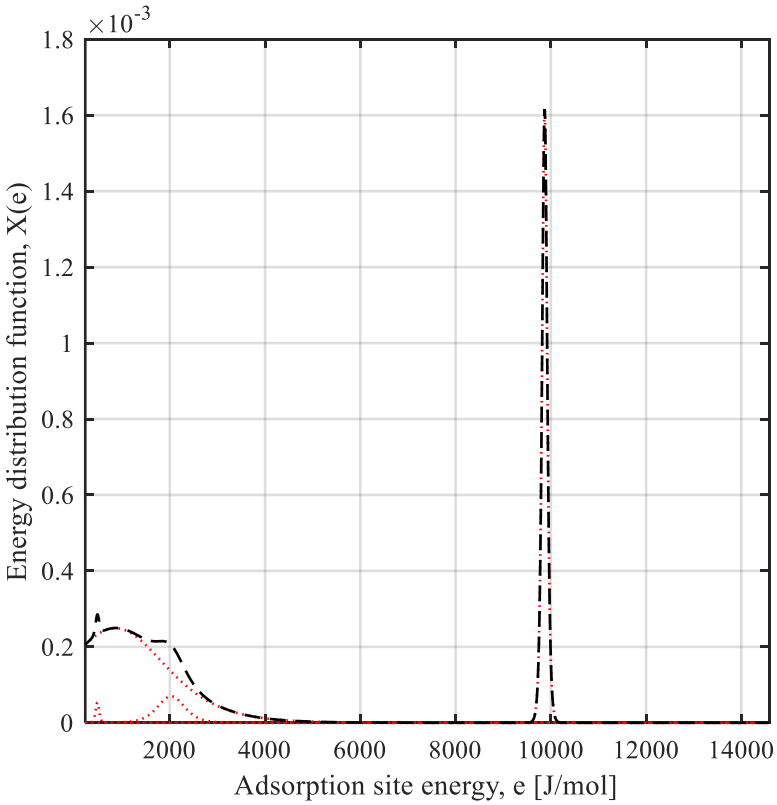

(b)

Figure 4.22 Predicted and measured data for AC 1:1 (a) adsorption isotherm and (b) the corresponding adsorption sites energy distribution. The curve with rings in (a) shows the experimental data points while the blue lines without rings show the universal isotherm model predictions.

AC 1:1's hydrogen adsorption results depict a type-IV isotherm with much of the area that looks like a type-I isotherm dominating, refer to figure 4.22 (a). There is a rapid increase in hydrogen uptake with increase in pressure up to about 20 kPa, then a slightly smoother though still steep uptake until higher pressures, 100 kPa. The change in hydrogen adsorption somewhat depicts saturation in one layer and most of the adsorption occurring in the multilayer. This is not entirely surprising as we saw wider pores for AC 1:1 from the PSD. This can also be attributed to the lower KOH activation ratio used in producing this activated carbon.

The energy distribution function, figure 4.22 (b), indicates a single probability peak at higher concentrations/pressures of about 10 000 J/mol adsorption site energy. This is also not surprising since the pores of the synthesised AC 1:1 are much wider and not as well developed as those of the other activated carbons, though still better than most ACs reported in literature. Most of the energy sites are in the higher-pressure areas for this AC, possibly indicating a stronger influence of the mesopores in adsorption.

AC 1:2

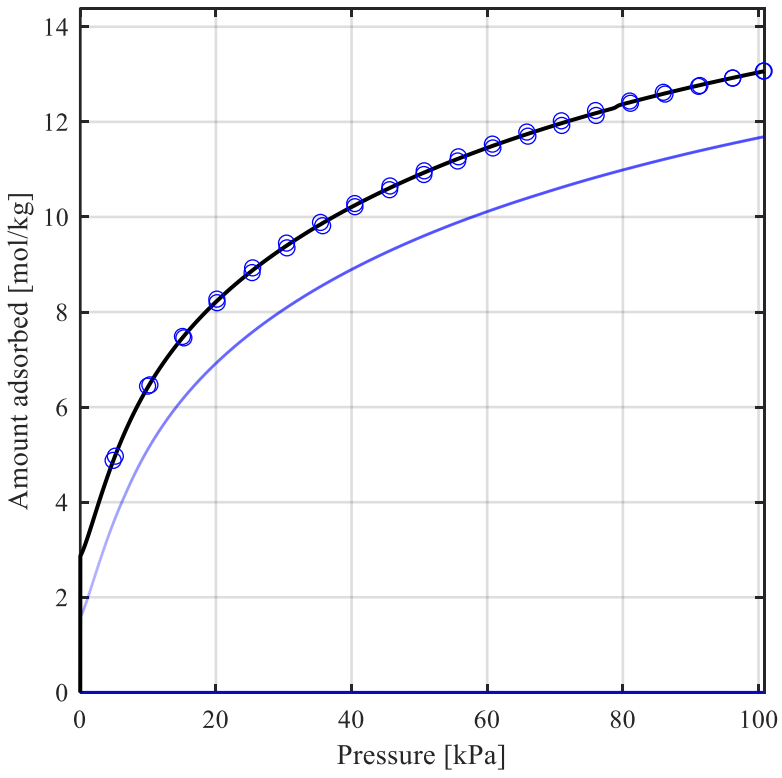

(a)

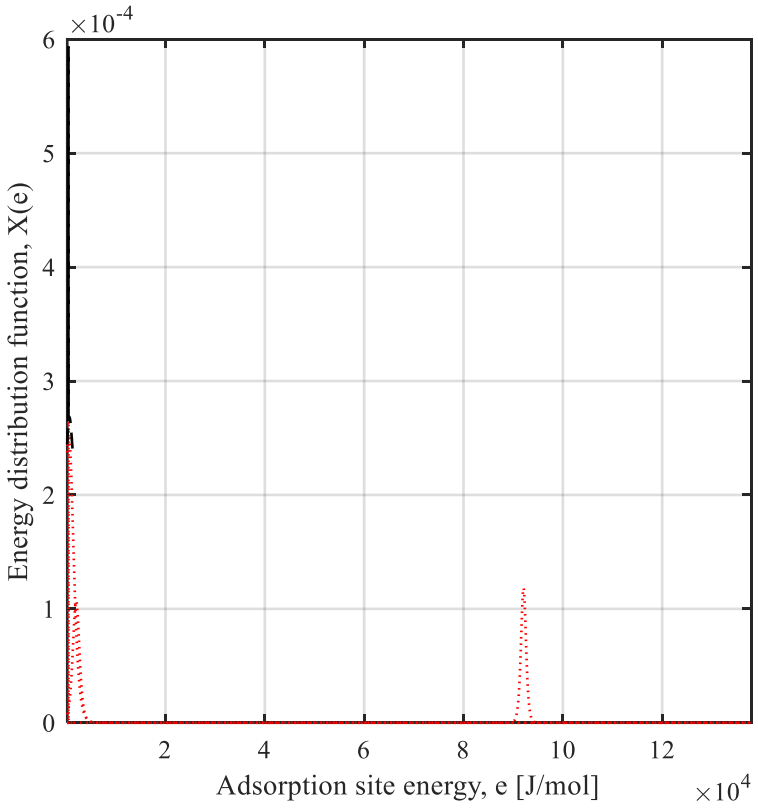

(b)

Figure 4.23 Predicted and measured data for AC 1:2 (a) adsorption isotherm and (b) the corresponding adsorption sites energy distribution. The curve with rings in (a) shows the experimental data points while the blue lines without rings show the universal isotherm model predictions.

Similar to AC 1:1, AC 1:2's hydrogen adsorption results depict a type-IV isotherm with much of the area looking like a type-I isotherm, figure 4.23 (a). There is a rapid increase in hydrogen uptake with increase in pressure up to about 28 kPa, then a slightly smoother uptake until higher pressures are reached. The change in hydrogen adsorption somewhat depicts saturation in one layer and most of the adsorption occurring in the multilayer. This is also not surprising as we saw wider pores for AC 1:2 from the PSD as well. This can also be attributed to the lower KOH activation ratio used in producing this activated carbon.

On the other hand, the energy distribution function, figure 4.23 (b), indicates a dual probability peaks at lower concentrations/pressures close to zero and another one at higher concentration, of about 92 000 J/mol adsorption site energy. The second peak energy site is quite high though it is also not surprising since the pores of the synthesised AC 1:2 are much wider and not as well developed as those of the other activated carbons in this study. Most of the energy sites are in the lower pressure area with another high concentration of energy sites at higher-pressure areas for this AC, indicating somewhat of an influence from small micropores and very wide micropores or of the mesopores in adsorption. The energy sites are not equally distributed but concentrated at lower and higher pressures, respectively, not so much in between.

AC 700

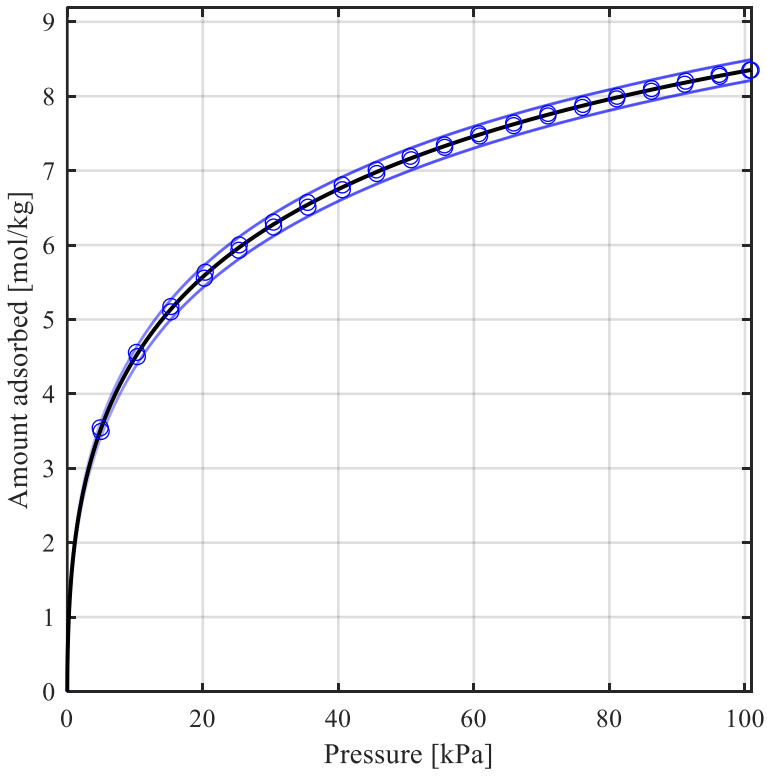

(a)

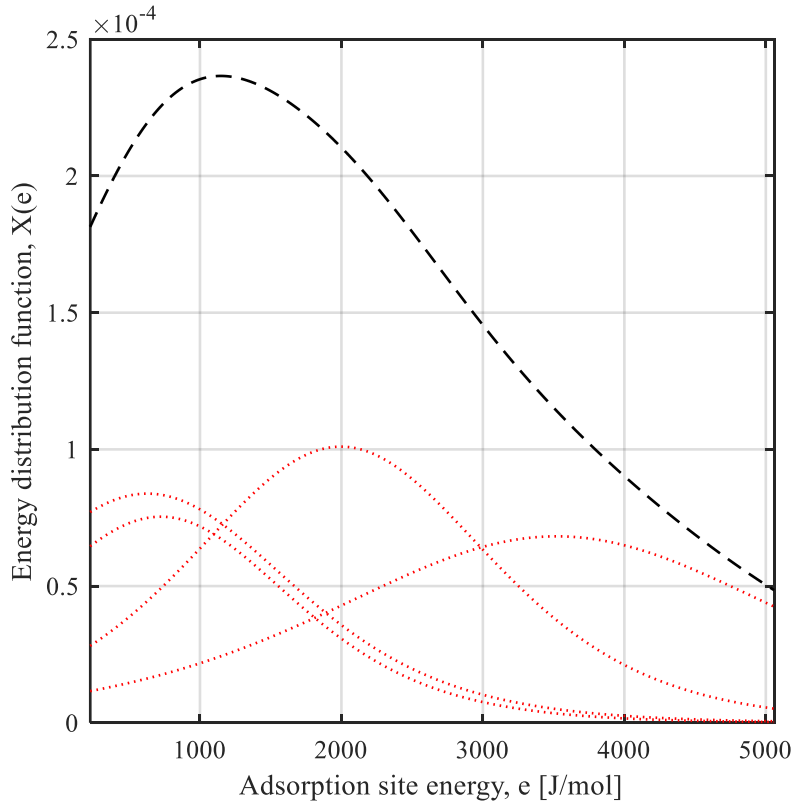

(b)

Figure 4.24 Predicted and measured data for AC 700 (a) adsorption isotherm and (b) the corresponding adsorption sites energy distribution. The curve with rings in (a) shows the experimental data points while the blue lines without rings show the universal isotherm model predictions.

Figure 4.24 (a) depicts type-II adsorption isotherm. This could indicate the part of type-IV isotherm S-shape that behaves like a type-II isotherm, making this a type-IV isotherm at lower pressures. Unlike the lower pressure type-I like behaviour of type-IV isotherm, the hydrogen uptake continues rapidly as pressure increases, without any 'plateau' or saturation point being observed. This figure shows a steep slope at lower pressures, indicating massive adsorption in this region.

The adsorption uptake for available adsorption sites, figure 4.24 (b), shows a pseudo-peak at lower concentrations. The available adsorption sites seem to be distributed across a wide range and not just at lower concentrations or higher concentrations as seen for some activated carbons. Most of the energy sites are still at lower concentrations, with adsorption site energies in the 300-2200 J/mol

The universal adsorption isotherm model, blue lines without rings, accurately predicted the experimental data for all of the activated carbons studied. Due to the experimental data being for hydrogen adsorption run at lower pressures, we cannot see the saturation points but the models are quite accurate nevertheless.

4.5 Summary

This chapter centered on the characterization of the samples used for the synthesis of the activated carbons. It investigated the produced activated carbons in greater depth. An evaluation was carried out on the adsorption capacities, porosity, and pore width distributions of the activated carbons. An examination was also conducted on the morphologies and functional groups of these activated carbons in order to identify crucial structural elements and functional groups that influence their efficacy in gas adsorption, specifically hydrogen adsorption. Additionally, each activated carbon's behaviour was predicted using the universal adsorption isotherm model.

CHAPTER 5: CONCLUSIONS AND RECOMMENDATIONS

5.1 Introduction

This chapter highlights the major findings from this research project and gives recommendations for future work based on key findings from the research project. The main aim of this research project was to synthesise activated carbons that are highly porous, from avocado waste, for hydrogen storage.

5.2 Major Findings of this Research

The application of hydrothermal carbonisation as a pretreatment method for avocado waste resulted in the production of hydrochars that exhibit favourable porosity characteristics. The majority of the pores seen within the hydrochars are primarily mesopores, with a smaller proportion of macropores present. The hydrothermal method enhanced the carbon content and ensured the presence of highly carbonaceous material for the activation step. The material produced also indicated a high level of purity, with minimal ash content and complete absence of sulphur.

The results of the scanning electron microscopy (SEM) study indicated that the activated carbons exhibit significantly smaller and more well-developed pores compared to the hydrochars from which they were derived. This observation can be attributed to the chemical activation process involving potassium hydroxide. After undergoing the activation procedure, the samples had a loss of their original shape, resulting in the activated carbons exhibiting irregular and bulky characteristics. Graphitisation occurs in activated carbons that are formed at elevated activation ratios and temperatures. Graphitisation and certain disordered amorphous carbon structures were detected through the presence of wider peaks in the X-ray diffraction (XRD) examination. The hydrochar's average crystallite size before to activation measures 32.23 nm. The mean size of the activated carbon crystallites is 0.79 nm.

The results of Fourier Transform Infrared (FTIR) analysis indicated that activated carbons synthesised with comparable KOH activation ratios exhibit identical functional groups. The activated carbons exhibit many functional groups, including the N-H stretching vibration group, C=O stretching vibration, C=C stretching vibration, N-O stretching vibration, C-H bending vibration, C-O stretching vibration, and the C=C bending vibration. The presence of oxygen-containing groups, namely C=O, N-O, and C-O, was confirmed using FTIR analysis. These groups play a crucial role as active sites, facilitating interactions with adjacent molecules and promoting hydrogen adsorption. Activated carbons have a greater abundance of C=C stretching and bending vibrations, while the majority of functional groups primarily undergo stretching motions.

The pore size distribution investigations revealed that the activated carbons synthesised exclusively possessed micropores, with no presence of meso- or macropores. A marginal contribution from the micropores, which have a width that is nearly comparable to mesopores, was detected. This observation suggests that there is a limited involvement of this particular pore type, as evidenced by the adsorption models. The activated carbons exhibited a variety of pore widths, specifically between 0.4 nm and 1.98 nm, suggesting the exclusive presence of micropores.

The nitrogen adsorption isotherms obtained at a temperature of 77K exhibit type-IV adsorption characteristics, which are often observed in microporous and mesoporous materials. Adsorption predominantly occurs at low relative pressures, with additional adsorption occurring in the mesopores once the micropores have reached saturation. Furthermore, further adsorption is found at relative pressures nearing 1, namely in the broader micropores that exhibit characteristics similar to mesopores. The presence of these broader micropores was predominantly found in activated carbons that were generated using lower chemical activation ratios or lower activation temperatures.

The activation of KOH resulted in the generation of surface areas that were very high. Specifically, the chemically activated carbons exhibited bigger surface areas when the activation ratio was higher, compared to those synthesised at lower activation ratios.

The experimental data for activated carbon derived from avocado waste was well modelled by the universal adsorption isotherm model, indicating that a majority of the activated carbon produced exhibited Type-IC adsorption isotherms.

In summary, the utilization of avocado waste has resulted in the production of activated carbons that exhibit a high degree of porosity. The activated carbons possess the capability to effectively store hydrogen gas. The hydrogen sorption data demonstrates that the activated carbons produced in this study successfully fulfill the hydrogen storage targets set by the Department of Energy (DOE).

5.3 Recommendations for Future Research

Further investigation is warranted to assess the potential application of the universal adsorption isotherm model in alternative hydrogen storage systems, with the aim of enhancing the efficiency of hydrogen storage design. It is recommended that a pilot research project be conducted in order to evaluate the feasibility of commercializing these activated carbons for hydrogen storage purposes.

References

Abdalla, A.M., Hossain, S., Nisfindy, O.B., Azad, A.T., Dawood, M. and Azad, A.K., 2018. Hydrogen production, storage, transportation and key challenges with applications: A review. *Energy conversion and management*, *165*, pp.602-627.

Abe, J.O., Popoola, A.P.I., Ajenifuja, E. and Popoola, O.M., 2019. Hydrogen energy, economy and storage: Review and recommendation. *International journal of hydrogen energy*, *44*(29), pp.15072-15086.

Ahmadpour, A. and Do, D.D., 1996. The preparation of active carbons from coal by chemical and physical activation. *Carbon*, *34*(4), pp.471-479.

Aliofkhazraei, M. ed., 2013. *Advances in graphene science*. BoD–Books on Demand.

Andersen, M.S., 2007. An introductory note on the environmental economics of the circular economy. *Sustainability science*, *2*(1), pp.133-140.

Anglo American, 2022, *Driving the Hydrogen Economy in South Africa*, viewed on 02 November 2023 from

https://www.angloamerican.com/our-stories/innovation-and-technology/driving-the-hydrogen-economy-in-south-africa#:~:text=The%20results%20of%20the%20independently,and%20indirect%20jobs%20per%20year

Aragón-Briceño, C.I., Pozarlik, A.K., Bramer, E.A., Niedzwiecki, L., Pawlak-Kruczek, H. and Brem, G., 2021. Hydrothermal carbonization of wet biomass from nitrogen and phosphorus approach: A review. *Renewable energy*, *171*, pp.401-415.

Ariharan, A., Ramesh, K., Vinayagamoorthi, R., Rani, M.S., Viswanathan, B., Ramaprabhu, S. and Nandhakumar, V., 2021. Biomass derived phosphorous containing porous carbon material for hydrogen storage and high-performance supercapacitor applications. *Journal of Energy Storage*, *35*, p.102185.

Azargohar, R., 2009. *Production of activated carbon and its catalytic application for oxidation of hydrogen sulphide* (Doctoral dissertation).

Bai, B.C., Kim, J.G., Naik, M.U.D., Im, J.S. and Lee, Y.S., 2011. The hydrogen storage capacity of metal-containing polyacrylonitrile-based electrospun carbon nanofibers. *Carbon letters*, *12*(3), pp.171-176.

Bega, S., 2021, 'South Africa wastes 10mn tons of food a year', in *Mail & Guardian*, viewed 23 September 2022, from

https://mg.co.za/environment/2021-08-21-south-africa-wastes-10-million-tons-of-food-a-year/

Begashaw, B., 2020, 'Strategies to deliver on the Sustainable Development Goals in Africa', in *Brookings*, viewed 17 September 2022, from

https://www.brookings.edu/research/strategies-to-deliver-on-the-sustainable-development-goals-in-africa/

Bering, B.P., Gordeeva, V.A., Dubinin, M.M., Efimova, L.I. and Serpinskii, V.V., 1971. Development of concepts of the volume filling of micropores in the adsorption of gases and vapors by microporous adsorbents: Communication 4. Differential heats and entropies of adsorption. *Bulletin of the Academy of Sciences of the USSR, Division of chemical science*, *20*, pp.17-22.

Bhatia, S.K. and Myers, A.L., 2006. Optimum conditions for adsorptive storage. *Langmuir*, *22*(4), pp.1688-1700.

Blackman, J.M., 2005. *High pressure hydrogen storage on carbon materials for mobile applications* (Doctoral dissertation, University of Nottingham).

Bleda-Martínez, M.J., Maciá-Agulló, J.A., Lozano-Castelló, D., Morallon, E., Cazorla-Amorós, D. and Linares-Solano, A., 2005. Role of surface chemistry on electric double layer capacitance of carbon materials. *Carbon*, *43*(13), pp.2677-2684.

Bocken, N.M., De Pauw, I., Bakker, C. and Van Der Grinten, B., 2016. Product design and business model strategies for a circular economy. *Journal of industrial and production engineering*, *33*(5), pp.308-320.

BP, 2011, *BP Energy Outlook 2030*, viewed 25 January 2022, from

https://www.bp.com/content/dam/bp/business-sites/en/global/corporate/pdfs/energy-economics/energy-outlook/bp-energy-outlook-2011.pdf

BP Global 2021, *bp study confirms feasibility of large-scale production of green hydrogen and green ammonia using renewable energy in Australia*, viewed 30 August 2021, from https://www.bp.com/en/global/corporate/news-and-insights/press-releases/bp-study-confirms-feasibility-of-large-scale-production-of-green-hydrogen-and-green-ammonia-using-renewable-energy-in-australia.html

Cabria, I., López, M.J. and Alonso, J.A., 2007. The optimum average nanopore size for hydrogen storage in carbon nanoporous materials. *Carbon*, *45*(13), pp.2649-2658.

Carrington, K.R., 2009. *Fabrication and optimization of nano-structured composites for energy storage*. University of California, Berkeley.

Celzard, A., Fierro, V., Marêché, J.F. and Furdin, G., 2007. Advanced preparative strategies for activated carbons designed for the adsorptive storage of hydrogen. *Adsorption Science & Technology*, *25*(3-4), pp.129-142.

Center for Strategic and International Studies (CSIS), 2022, *South Africa's Hydrogen Strategy*, viewed on 17 September 2023, from

https://www.csis.org/analysis/south-africas-hydrogen-strategy#:~:text=The%20country's%20vision%20is%20guided,of%20hydrogen%20annually%20by%202030

Chambers, A., Park, C., Baker, R.T.K. and Rodriguez, N.M., 1998. Hydrogen storage in graphite nanofibers. *The journal of physical chemistry B*, *102*(22), pp.4253-4256.

Chen, P., Wu, X., Lin, J. and Tan, K.L., 1999. High H_2 uptake by alkali-doped carbon nanotubes under ambient pressure and moderate temperatures. *Science*, *285*(5424), pp.91-93.

Chen, X., Zhang, Y., Gao, X.P., Pan, G.L., Jiang, X.Y., Qu, J.Q., Wu, F., Yan, J. and Song, D.Y., 2004. Electrochemical hydrogen storage of carbon nanotubes and carbon nanofibers. *International Journal of Hydrogen Energy*, *29*(7), pp.743-748.

Chen, D., Chen, X., Sun, J., Zheng, Z. and Fu, K., 2016. Pyrolysis polygeneration of pine nut shell: quality of pyrolysis products and study on the preparation of activated carbon from biochar. *Bioresource technology*, *216*, pp.629-636.

Cheng, F., Liang, J., Zhao, J., Tao, Z. and Chen, J., 2008. Biomass waste-derived microporous carbons with controlled texture and enhanced hydrogen uptake. *Chemistry of Materials*, *20*(5), pp.1889-1895.

Cheng, F. and Li, X., 2018. Preparation and application of biochar-based catalysts for biofuel production. *Catalysts*, *8*(9), p.346.

Chung, D.D., 2016. Carbon composites: composites with carbon fibers, nanofibers, and nanotubes. Butterworth-Heinemann.

Colombo, R. and Papetti, A., 2019. Avocado (Persea americana Mill.) by-products and their impact: from bioactive compounds to biomass energy and sorbent material for removing contaminants. A review. *International Journal of Food Science & Technology*, *54*(4), pp.943-951.

Conserve Energy Future, 2015, *Pros and Cons of Fossil Fuels*, viewed 28 September 2021, from https://www.conserve-energy-future.com/pros-and-cons-of-fossil-fuels.php

Dai, H., 2002. Carbon nanotubes: opportunities and challenges. *Surface science*, *500*(1-3), pp.218-241.

Dai, S. and Seol, Y., 2014. Water permeability in hydrate-bearing sediments: A pore-scale study. *Geophysical Research Letters*, *41*(12), pp.4176-4184.

Daud, W.M.A.W. and Houshamnd, A.H., 2010. Textural characteristics, surface chemistry and oxidation of activated carbon. *Journal of Natural Gas Chemistry*, *19*(3), pp.267-279.

Delgass, I, 2023, ScIU, *Graphene: A single-layer magic material*, accessed on 02 November 2023, viewed from

https://blogs.iu.edu/sciu/2023/09/16/graphene-magic-material/

Department of Environment, Forestry and Fisheries (DEFF), and Council for Scientific and Industrial Research (CSIR), 2019, *Food waste prevention & management: A guideline for South Africa*, 1st edn, DEFF & CSIR, Pretoria, viewed 01 October 2022, from

https://wasteroadmap.co.za/wp-content/uploads/2020/09/17-CSIR-Final_Technical-report_Food-waste-guideline.pdf

Dillon, A.C., 1996. Storage Of Hydrogen In Single-walled Carbon Nanotubes. *Nature*, *386*, p.147.

Dillon, A., Jones, K.M., Bekkedahl, T.A., Kiang, C.H., Bethune, D.S. and Heben, M.J., 1997. Storage of hydrogen in single-walled carbon nanotubes. *Nature*, *386*(6623), pp.377-379.

Dillon, A.C., Gilbert, K.E.H., Parilla, P.A., Alleman, J.L., Hornyak, G.L., Jones, K.M. and Heben, M.J., 2002. Hydrogen storage in carbon single-wall nanotubes. In *Proceedings of the 2002 US DOE Hydrogen Program review* (pp. 1-18).

Dubinin, M.M. and Astakhov, V.A., 1971. Development of the concepts of volume filling of micropores in the adsorption of gases and vapors by microporous adsorbents: Communication 1. Carbon adsorbents. *Bulletin of the Academy of Sciences of the USSR, Division of chemical science*, *20*, pp.3-7.

Durbin, D.J. and Malardier-Jugroot, C., 2013. Review of hydrogen storage techniques for on board vehicle applications. *International journal of hydrogen energy*, *38*(34), pp.14595-14617.

Edwards, I.A., Marsh, H. and Menendez, R., 2013. *Introduction to carbon science*. Butterworth-Heinemann.

El-Sayed, Y. and Bandosz, T.J., 2004. Adsorption of valeric acid from aqueous solution onto activated carbons: role of surface basic sites. *Journal of colloid and interface science*, *273*(1), pp.64-72.

Ellen MacArthur Foundation, 2020, *Circular economy introduction*, viewed 15 September 2022, from

https://ellenmacarthurfoundation.org/topics/circular-economy-introduction/overview

Energy.gov, 2009, *Targets for Onboard Hydrogen Storage Systems for Light-Duty Vehicles*, viewed 06 May 2021, from

https://www1.eere.energy.gov/hydrogenandfuelcells/storage/pdfs/targets_onboard_hydro_storage_explanation.pdf.

Energy.gov, 2021, *Hydrogen Production: Electrolysis*, viewed on 02 November 2023, from

https://www.energy.gov/eere/fuelcells/hydrogen-production-electrolysis#:~:text=In%20a%20polymer%20electrolyte%20membrane,the%20PEM%20to%20the%20cathode.

Eriksson, L., Johansson, E., Kettaneh-Wold, N., Wikström, C. and Wold, S., 2000. Design of experiments. *Principles and Applications, Learn ways AB, Stockholm*.

Fan, Z., Zhang, Z., Zhang, G., Qin, L., Fang, J. and Tao, P., 2022. Phosphoric acid/FeCl3 converting waste mangosteen peels into bio-carbon adsorbents for methylene blue removal. *International Journal of Environmental Science and Technology*, *19*(12), pp.12315-12328.

FAO, 2021,*Other products*, viewed 21 October 2021 from https://www.fao.org/3/cb5332en/Other.pdf

Feng, B. and Bhatia, S.K., 2003. Variation of the pore structure of coal chars during gasification. *Carbon*, *41*(3), pp.507-523.

Feng, J., Zhu, H., Xu, Y., Jiang, J. and Pan, H., 2021. Preparation and characterization of high-performance activated carbon from papermaking black-liquor at low temperature. Journal of Analytical and Applied Pyrolysis, 159, p.105292.

Fierro, V., Torné-Fernández, V. and Celzard, A., 2007. Methodical study of the chemical activation of Kraft lignin with KOH and NaOH. *Microporous and Mesoporous Materials*, *101*(3), pp.419-431.

Fierro, V., Szczurek, A., Zlotea, C., Marêché, J.F., Izquierdo, M.T., Albiniak, A., Latroche, M., Furdin, G. and Celzard, A., 2010. Experimental evidence of an upper limit for hydrogen storage at 77 K on activated carbons. *Carbon*, *48*(7), pp.1902-1911.

Fierro, V., Zhao, W., Izquierdo, M.T., Aylon, E. and Celzard, A., 2010. Adsorption and compression contributions to hydrogen storage in activated anthracites. *international Journal of hydrogen energy*, *35*(17), pp.9038-9045.

Figueiredo, J.L., Pereira, M.F.R., Freitas, M.M.A. and Orfao, J.J.M., 1999. Modification of the surface chemistry of activated carbons. *carbon*, *37*(9), pp.1379-1389.

Gao, Y., Huang, H., Tang, W., Liu, X., Yang, X. and Zhang, J., 2015. Preparation and characterization of a novel porous silicate material from coal gangue. Microporous and Mesoporous Materials, 217, pp.210-218.

Geissdoerfer, M., Savaget, P., Bocken, N.M. and Hultink, E.J., 2017. The Circular Economy–A new sustainability paradigm?. *Journal of cleaner production*, *143*, pp.757-768.

Georgiev, P.A., Ross, D.K., Albers, P. and Ramirez-Cuesta, A.J., 2006. The rotational and translational dynamics of molecular hydrogen physisorbed in activated carbon: a direct probe of microporosity and hydrogen storage performance. *Carbon*, *44*(13), pp.2724-2738.

Girgis, B.S., Temerk, Y.M., Gadelrab, M.M. and Abdullah, I.D., 2007. X-ray diffraction patterns of activated carbons prepared under various conditions. *Carbon letters*, *8*(2), pp.95-100.

Govindan, K., Soleimani, H. and Kannan, D., 2015. Reverse logistics and closed-loop supply chain: A comprehensive review to explore the future. *European journal of operational research*, *240*(3), pp.603-626.

Goyal, M., Rattan, V.K., Aggarwal, D. and Bansal, R.C., 2001. Removal of copper from aqueous solutions by adsorption on activated carbons. *Colloids and Surfaces A: Physicochemical and Engineering Aspects*, *190*(3), pp.229-238.

Guan, C., Wang, K., Yang, C. and Zhao, X.S., 2009. Characterization of a zeolite-templated carbon for H2 storage application. *Microporous and Mesoporous Materials*, *118*(1-3), pp.503-507.

Guide Jr, V.D.R. and Van Wassenhove, L.N., 2009. OR FORUM—The evolution of closed-loop supply chain research. *Operations research*, *57*(1), pp.10-18.

Guo, J. and Lua, A.C., 1999. Effect of surface chemistry on gas-phase adsorption by activated carbon prepared from oil-palm stone with pre-impregnation. *Separation and Purification Technology*, *18*(1), pp.47-55.

Hayashi, J.I., Kazehaya, A., Muroyama, K. and Watkinson, A.P., 2000. Preparation of activated carbon from lignin by chemical activation. *Carbon*, *38*(13), pp.1873-1878.

Hesas, R.H., Arami-Niya, A., Daud, W.M.A.W. and Sahu, J.N., 2015. Microwave-assisted production of activated carbons from oil palm shell in the presence of CO_2 or N2 for CO_2 adsorption. *Journal of Industrial and Engineering Chemistry*, *24*, pp.196-205.

Hoekman, S.K., Broch, A., Robbins, C., Zielinska, B. and Felix, L., 2013. Hydrothermal carbonization (HTC) of selected woody and herbaceous biomass feedstocks. Biomass Conversion and Biorefinery, 3, pp.113-126.

Hsu, L.Y. and Teng, H., 2000. Influence of different chemical reagents on the preparation of activated carbons from bituminous coal. *Fuel Processing Technology*, *64*(1-3), pp.155-166.

IEA, 2023a, World Energy Outlook 2023, viewed on 20 October 2023, from

https://iea.blob.core.windows.net/assets/66b8f989-971c-4a8d-82b0-4735834de594/WorldEnergyOutlook2023.pdf

IEA, 2023, Government Energy Spending Tracker, viewed on 10 October 2023, from

https://www.iea.org/reports/government-energy-spending-tracker-2

IEA, World electricity final consumption by sector, 1974-2019, IEA, Paris

https://www.iea.org/data-and-statistics/charts/world-electricity-final-consumption-by-sector-1974-2019, IEA. Licence: CC BY 4.0

Iijima, S., 1991. Helical microtubules of graphitic carbon. *nature*, *354*(6348), pp.56-58.

International Monetary Fund (IMF), 2023, *World Economic Outlook (October 2023)*, viewed 20 October 2023, from

https://www.imf.org/external/datamapper/datasets/WEO

Islam, M.R., Nabi, M.N. and Islam, M.N., 2001, December. Characterization of biomass solid waste for liquid fuel production. In *Proc. of* (Vol. 4, pp. 77-82).

Jain, V. and Kandasubramanian, B., 2020. Functionalized graphene materials for hydrogen storage. *Journal of Materials Science*, *55*(5), pp.1865-1903.

Jaroniec, M. and Marczewski, A.W., 1984. Physical adsorption of gases on energetically heterogeneous solids I. GeneralizedLangmuir equation and its energy distribution. *Monatshefte Für Chemie/Chemical Monthly*, *115*(8), pp.997-1012.

Jaroniec, M. and Marczewski, A.W., 1984. Physical adsorption of gases on energetically heterogeneous solids II. Theoretical extension of a generalizedLangmuir equation and its application for analysing adsorption data. *Monatshefte für Chemie/Chemical Monthly*, *115*(8), pp.1013-1038.

Jordá-Beneyto, M., Suárez-García, F., Lozano-Castello, D., Cazorla-Amorós, D. and Linares-Solano, A., 2007. Hydrogen storage on chemically activated carbons and carbon nanomaterials at high pressures. *Carbon*, *45*(2), pp.293-303.

Kabbour, H., Baumann, T.F., Satcher, J.H., Saulnier, A. and Ahn, C.C., 2006. Toward new candidates for hydrogen storage: high-surface-area carbon aerogels. *Chemistry of Materials*, *18*(26), pp.6085-6087.

Kajama, M.N., Nwogu, N.C. and Gobina, E., 2015. Hydrogen permeation using nanostructured silica membranes. *Sustain Dev Plan*, *7*(193), pp.447-456.

Karakehya, N., 2023. Effects of one-step and two-step KOH activation method on the properties and supercapacitor performance of highly porous activated carbons prepared from Lycopodium clavatum spores. Diamond and Related Materials, 135, p.109873.

Karić, N., Maia, A.S., Teodorović, A., Atanasova, N., Langergraber, G., Crini, G., Ribeiro, A.R. and Đolić, M., 2022. Bio-waste valorisation: Agricultural wastes as biosorbents for removal of (in) organic pollutants in wastewater treatment. *Chemical Engineering Journal Advances*, *9*, p.100239.

Ladavos, A.K., Katsoulidis, A.P., Iosifidis, A., Triantafyllidis, K.S., Pinnavaia, T.J. and Pomonis, P.J., 2012. The BET equation, the inflection points of N2 adsorption isotherms and the estimation

of specific surface area of porous solids. *Microporous and Mesoporous Materials*, *151*, pp.126-133.

Lee, Y.J., Uchiyama, Y. and Radovic, L.R., 2004. Effects of boron doping in low-and high-surface-area carbon powders. *Carbon*, *42*(11), pp.2233-2244.

Lee, K.H., Noh, J. and Khim, J.S., 2020. The Blue Economy and the United Nations' sustainable development goals: Challenges and opportunities. *Environment international*, *137*, p.105528.

Libretexts n.d., *Bragg's Law*, viewed 15 October 2023, from

https://chem.libretexts.org/Bookshelves/Analytical_Chemistry/Supplemental_Modules_(Analytical_Chemistry)/Instrumentation_and_Analysis/Diffraction_Scattering_Techniques/Bragg's_Law

Lillo-Ródenas, M.A., Cazorla-Amorós, D. and Linares-Solano, A., 2003. Understanding chemical reactions between carbons and NaOH and KOH: an insight into the chemical activation mechanism. *Carbon*, *41*(2), pp.267-275.

Linde Engineering, 2021, The Entire Value Chain of Hydrogen, viewed 15 November 2022, from https://www.linde-engineering.com/en/index.html

Li, Q., Lu, T., Wang, L., Pang, R., Shao, J., Liu, L. and Hu, X., 2021. Biomass based N-doped porous carbons as efficient CO_2 adsorbents and high-performance supercapacitor electrodes. *Separation and Purification Technology*, *275*, p.119204.

Lobato-Peralta, D.R., Duque-Brito, E., Ayala-Cortés, A., Arias, D.M., Longoria, A., Cuentas-Gallegos, A.K., Sebastian, P.J. and Okoye, P.U., 2021. Advances in activated carbon modification, surface heteroatom configuration, reactor strategies, and regeneration methods for enhanced wastewater treatment. *Journal of Environmental Chemical Engineering*, *9*(4), p.105626.

Lozano-Castello, D., Lillo-Ródenas, M.A., Cazorla-Amorós, D. and Linares-Solano, A., 2001. Preparation of activated carbons from Spanish anthracite: I. Activation by KOH. *Carbon*, *39*(5), pp.741-749.

Lucian, M., Volpe, M., Gao, L., Piro, G., Goldfarb, J.L. and Fiori, L., 2018. Impact of hydrothermal carbonisation conditions on the formation of hydrochars and secondary chars from the organic fraction of municipal solid waste. Fuel, 233, pp.257-268.

Lv, L., Huang, Y. and Cao, D., 2018. Nitrogen-doped porous carbons with ultrahigh specific surface area as bifunctional materials for dye removal of wastewater and supercapacitors. *Applied Surface Science*, *456*, pp.184-194.

Lyle, J.T., 1996. *Regenerative design for sustainable development*. John Wiley & Sons.

Lyman, C.E., 1990. *Scanning electron microscopy, X-ray microanalysis, and analytical electron microscopy: a laboratory workbook*. Springer Science & Business Media.

Malinauskaite, J., Jouhara, H., Czajczyńska, D., Stanchev, P., Katsou, E., Rostkowski, P., Thorne, R.J., Colon, J., Ponsá, S., Al-Mansour, F. and Anguilano, L., 2017. Municipal solid waste management and waste-to-energy in the context of a circular economy and energy recycling in Europe. *Energy*, *141*, pp.2013-2044.

Marbán, G. and Valdés-Solís, T., 2007. Towards the hydrogen economy?. *International journal of hydrogen energy*, *32*(12), pp.1625-1637.

Marco-Lozar, J.P., Juan-Juan, J., Suárez-García, F., Cazorla-Amorós, D. and Linares-Solano, A., 2012. MOF-5 and activated carbons as adsorbents for gas storage. *International Journal of Hydrogen Energy*, *37*(3), pp.2370-2381.

Marczewski, A.W. and Jaroniec, M., 1983. A new isotherm equation for single-solute adsorption from dilute solutions on energetically heterogeneous solids. *Monatshefte für Chemie/Chemical Monthly*, *114*(6), pp.711-715.

Masoumi, S., Borugadda, V.B., Nanda, S. and Dalai, A.K., 2021. Hydrochar: A review on its production technologies and applications. Catalysts, 11(8), p.939.

Merck n.d., *What is FTIR Spectroscopy?*, viewed 20 June 2023, from

https://www.sigmaaldrich.com/ZA/en/technical-documents/technical-article/analytical-chemistry/photometry-and-reflectometry/ftir-spectroscopy

Misture, S.T. and Snyder, R.L., 2001. Encyclopedia of Materials. Science and Technology, 10, pp.9799-9809.

Mohan, M., Sharma, V.K., Kumar, E.A. and Gayathri, V., 2019. Hydrogen storage in carbon materials—A review. *Energy Storage*, *1*(2), p.e35.

Molina-Sabio, M. and Rodrıguez-Reinoso, F., 2004. Role of chemical activation in the development of carbon porosity. *Colloids and Surfaces A: Physicochemical and Engineering Aspects*, *241*(1-3), pp.15-25.

Møller, K.T., Jensen, T.R., Akiba, E. and Li, H.W., 2017. Hydrogen-A sustainable energy carrier. *Progress in Natural Science: Materials International*, *27*(1), pp.34-40.

Moradi, R. and Groth, K.M., 2019. Hydrogen storage and delivery: Review of the state of the art technologies and risk and reliability analysis. *International Journal of Hydrogen Energy*, *44*(23), pp.12254-12269.

Myers, A.L. and Belfort, G., 1984. *Fundamentals of adsorption* (No. CONF-8305159-). Engineering Foundation, New York, NY.

Nevskaia, D.M., Castillejos-Lopez, E., Guerrero-Ruiz, A. and Munoz, V., 2004. Effects of the surface chemistry of carbon materials on the adsorption of phenol–aniline mixtures from water. *Carbon*, *42*(3), pp.653-665.

Nhuchhen, D.R., 2016. Prediction of carbon, hydrogen, and oxygen compositions of raw and torrefied biomass using proximate analysis. *Fuel*, *180*, pp.348-356.

Novoselov, K.S., 2011. Graphene: the magic of flat carbon. *The Electrochemical Society Interface*, *20*(1), p.45.

Okman, I., Karagöz, S., Tay, T. and Erdem, M., 2014. Activated carbons from grape seeds by chemical activation with potassium carbonate and potassium hydroxide. *Applied Surface Science*, *293*, pp.138-142.

Osswald, S., Portet, C., Gogotsi, Y., Laudisio, G., Singer, J.P., Fischer, J.E., Sokolov, V.V., Kukushkina, J.A. and Kravchik, A.E., 2009. Porosity control in nanoporous carbide-derived carbon by oxidation in air and carbon dioxide. *Journal of Solid State Chemistry*, *182*(7), pp.1733-1741.

Oyedepo, S.O., 2012. On energy for sustainable development in Nigeria. *Renewable and sustainable energy reviews*, *16*(5), pp.2583-2598.

Panella, B., Hirscher, M. and Roth, S., 2005. Hydrogen adsorption in different carbon nanostructures. *Carbon*, *43*(10), pp.2209-2214.

Pang, R., Lu, T., Shao, J., Wang, L., Wu, X., Qian, X. and Hu, X., 2020. Highly efficient nitrogen-doped porous carbonaceous CO_2 adsorbents derived from biomass. *Energy & Fuels*, *35*(2), pp.1620-1628.

Pearce, D.W., Turner, R.K. and Turner, R.K., 1990. *Economics of natural resources and the environment*. Johns Hopkins University Press.

Pederson, M.R. and Broughton, J.Q., 1992. Nanocapillarity in fullerene tubules. *Physical Review Letters*, *69*(18), p.2689.

Power Engineering International (PEI), 2023, *Green hydrogen projects blazing a trail in South Africa*, viewed on 17 September 2023, from

https://www.powerengineeringint.com/hydrogen/green-hydrogen-projects-blazing-a-trail-in-south-africa/

Przepiórski, J., 2006a. Activated carbon filters and their industrial applications. In *Interface Science and Technology* (Vol. 7, pp. 421-474). Elsevier.

Przepiórski, J., 2006b. Enhanced adsorption of phenol from water by ammonia-treated activated carbon. *Journal of hazardous materials*, *135*(1-3), pp.453-456.

Qin, Z., Gao, Q., Zhang, S. and Li, J., 2014. Surface free energy and dynamic wettability of differently machined poplar woods. *BioResources*, *9*(2), pp.3088-3103.

Ren, J., Musyoka, N.M., Langmi, H.W., Swartbooi, A., North, B.C. and Mathe, M., 2015. A more efficient way to shape metal-organic framework (MOF) powder materials for hydrogen storage applications. *international journal of hydrogen energy*, *40*(13), pp.4617-4622.

Restrepo-Serna, D.L., Solarte-Toro, J.C. and Cardona-Alzate, C.A., 2022. A Biorefinery Approach for an Integral Valorisation of Avocado Peel and Seeds Through Supercritical Fluids. *Waste and Biomass Valorisation*, pp.1-16.

Romero-Hernández, O. and Romero, S., 2018. Maximizing the value of waste: From waste management to the circular economy. *Thunderbird International Business Review*, *60*(5), pp.757-764.

Rouquerol, J., Llewellyn, P. and Rouquerol, F.J.S.S.S.C., 2007. Is the BET equation applicable to microporous adsorbents. *Stud. Surf. Sci. Catal*, *160*(07), pp.49-56.

Rowlandson, J., 2019. Development of Nanoporous Carbons from Renewable Lignin Feedstocks for Sustainable Applications (Doctoral dissertation, University of Bristol).

Ruiz, B., Ruisánchez, E., Gil, R.R., Ferrera-Lorenzo, N., Lozano, M.S. and Fuente, E., 2015. Sustainable porous carbons from lignocellulosic wastes obtained from the extraction of tannins. *Microporous and Mesoporous Materials*, *209*, pp.23-29.

Ryoo, R., Joo, S.H., Kruk, M. and Jaroniec, M., 2001. Ordered mesoporous carbons. *Advanced Materials*, *13*(9), pp.677-681.

Rzepka, M., Lamp, P. and De la Casa-Lillo, M.A., 1998. Physisorption of hydrogen on microporous carbon and carbon nanotubes. *The Journal of Physical Chemistry B*, *102*(52), pp.10894-10898.

Saleh, T.A., 2022. *Surface Science of Adsorbents and Nanoadsorbents: Properties and Applications in Environmental Remediation*. Academic Press.

Salmenperä, H., Pitkänen, K., Kautto, P. and Saikku, L., 2021. Critical factors for enhancing the circular economy in waste management. *Journal of cleaner production*, *280*, p.124339.

Sangchoom, W. and Mokaya, R., 2015. Valorisation of lignin waste: carbons from hydrothermal carbonisation of renewable lignin as superior sorbents for CO_2 and hydrogen storage. *ACS Sustainable Chemistry & Engineering*, *3*(7), pp.1658-1667.

Sarwar, A., Ali, M., Khoja, A.H., Nawar, A., Waqas, A., Liaquat, R., Naqvi, S.R. and Asjid, M., 2021. Synthesis and characterization of biomass-derived surface-modified activated carbon for enhanced CO_2 adsorption. *Journal of CO_2 Utilization*, *46*, p.101476.

Serafin, J., Baca, M., Biegun, M., Mijowska, E., Kaleńczuk, R.J., Sreńscek-Nazzal, J. and Michalkiewicz, B., 2019. Direct conversion of biomass to nanoporous activated biocarbons for high CO_2 adsorption and supercapacitor applications. *Applied Surface Science*, *497*, p.143722.

Sethia, G. and Sayari, A., 2016. Activated carbon with optimum pore size distribution for hydrogen storage. *Carbon*, *99*, pp.289-294.

Sevilla, M. and Mokaya, R., 2014. Energy storage applications of activated carbons: supercapacitors and hydrogen storage. *Energy & Environmental Science*, *7*(4), pp.1250-1280.

Shahzad, U., 2012. The need for renewable energy sources. *energy*, *2*, pp.16-18.

Smith, B.C., 2011. *Fundamentals of Fourier transform infrared spectroscopy*. CRC press.

Smith-Godfrey, S., 2016. Defining the blue economy. *Maritime affairs: Journal of the national maritime foundation of India*, *12*(1), pp.58-64.

Stahel, W., 2010. *The performance economy*. Springer.

Stahel, W. and Reday, G., 1976. Report The Potential for Substituting Manpower for Energy. *Geneva Research Centre: Geneva, Switzerland*.

Statista, 2021, *Avocado production worldwide from 2000 to 2019*, viewed 04 October 2021, from https://www.statista.com/statistics/577455/world-avocado-production/

Stindt, D. and Sahamie, R., 2014. Review of research on closed loop supply chain management in the process industry. *Flexible Services and Manufacturing Journal*, *26*(1), pp.268-293.

Streppel, B., 2011. Hydrogen adsorption on metal-organic frameworks.

Suárez-Garcıa, F., Martınez-Alonso, A. and Tascón, J.D., 2002. Pyrolysis of apple pulp: chemical activation with phosphoric acid. *Journal of Analytical and Applied Pyrolysis*, *63*(2), pp.283-301.

Tay, T., Ucar, S. and Karagöz, S., 2009. Preparation and characterization of activated carbon from waste biomass. Journal of Hazardous Materials, 165(1-3), pp.481-485.

Teng, H. and Hsu, L.Y., 1999. High-porosity carbons prepared from bituminous coal with potassium hydroxide activation. *Industrial & engineering chemistry research*, *38*(8), pp.2947-2953.

Tesfaye, T., Gibril, M., Sithole, B., Ramjugernath, D., Chavan, R., Chunilall, V. and Gounden, N., 2018. Valorisation of avocado seeds: extraction and characterization of starch for textile applications. *Clean Technologies and Environmental Policy*, *20*(9), pp.2135-2154.

Texier-Mandoki, N., Dentzer, J., Piquero, T., Saadallah, S., David, P. and Vix-Guterl, C., 2004. Hydrogen storage in activated carbon materials: role of the nanoporous texture. *Carbon*, *12*(42), pp.2744-2747.

The World Bank, 2020, 'The African Continental Free Trade Area', viewed 09 October 2022, from

https://www.worldbank.org/en/topic/trade/publication/the-african-continental-free-trade-area

The world counts, n.d., *Global energy consumption only going up*, viewed October 05 2023, from

https://www.theworldcounts.com/challenges/climate-change/energy/global-energy-consumption

Thomas, S., Sarathchandran, C., Ilangovan, S.A. and Moreno-Pirajan, J.C. eds., 2021. *Handbook of carbon-based nanomaterials*. Elsevier.

Tomić, T. and Schneider, D.R., 2020. Circular economy in waste management–Socio-economic effect of changes in waste management system structure. *Journal of environmental management*, *267*, p.110564.

Tozzini, V. and Pellegrini, V., 2013. Prospects for hydrogen storage in graphene. *Physical Chemistry Chemical Physics*, *15*(1), pp.80-89.

UNFCCC, 2020, *The Paris Agreement*, viewed 30 January 2022, from

https://unfccc.int/process-and-meetings/the-paris-agreement/the-paris-agreement#:~:text=The%20Paris%20Agreement%20is%20a,force%20on%204%20November%202016

Üner, O., Geçgel, Ü. and Bayrak, Y., 2019. Preparation and characterization of mesoporous activated carbons from waste watermelon rind by using the chemical activation method with zinc chloride. *Arabian Journal of Chemistry*, *12*(8), pp.3621-3627.

Usman, M.R., 2022. Hydrogen storage methods: Review and current status. *Renewable and Sustainable Energy Reviews*, *167*, p.112743.

Valix, M., Cheung, W.H. and Zhang, K., 2006. Role of heteroatoms in activated carbon for removal of hexavalent chromium from wastewaters. *Journal of Hazardous Materials*, *135*(1-3), pp.395-405.

Valoras, N., Letey, J., Stolzy, L.H. and Frolich, E.F., 1964. The oxygen requirements for root growth of three avocado varieties. In *Proc. Amer. Soc. Hort. Sci* (Vol. 85, pp. 172-178).

Volpe, M. and Cleri, F., 2003. Role of surface chemistry in hydrogen adsorption in single-wall carbon nanotubes. *Chemical physics letters*, *371*(3-4), pp.476-482.

Wandelt, K., 2018. *Encyclopedia of interfacial chemistry: surface science and electrochemistry*. Elsevier.

Wang, H., Gao, Q. and Hu, J., 2009. High hydrogen storage capacity of porous carbons prepared by using activated carbon. *Journal of the American Chemical Society*, *131*(20), pp.7016-7022.

Wazir, A.H., Haq, I.U., Manan, A. and Khan, A., 2022. Preparation and characterization of activated carbon from coal by chemical activation with KOH. International Journal of Coal Preparation and Utilization, 42(5), pp.1477-1488.

Worldometer, 2023, *World Population by Year*, viewed 20 June 2023, from

https://www.worldometers.info/world-population/world-population-by-year/

Xu, W.C., Takahashi, K., Matsuo, Y., Hattori, Y., Kumagai, M., Ishiyama, S., Kaneko, K. and Iijima, S., 2007. Investigation of hydrogen storage capacity of various carbon materials. *International Journal of Hydrogen Energy*, *32*(13), pp.2504-2512.

Yagub, M.T., Sen, T.K., Afroze, S. and Ang, H.M., 2014. Dye and its removal from aqueous solution by adsorption: a review. *Advances in colloid and interface science*, *209*, pp.172-184.

Yahya, M.A., Al-Qodah, Z. and Ngah, C.Z., 2015. Agricultural bio-waste materials as potential sustainable precursors used for activated carbon production: A review. *Renewable and Sustainable Energy Reviews*, *46*, pp.218-235.

Yuan, Z., Bi, J. and Moriguichi, Y., 2006. The circular economy: A new development strategy in China. *Journal of Industrial Ecology*, *10*(1-2), pp.4-8.

Zarrouk, S.J. and McLean, K., 2019. Geothermal well test analysis: fundamentals, applications and advanced techniques.

ZHA, Q.F., HU, X.H., GUO, Y.S., WU, M.B., LI, Z.F. and ZHANG, Y.Z., 2008. Improved antioxidative ability of porous carbons by boron-doping. *New Carbon Materials*, *23*(4), pp.356-360.

Zhang, F., Zhao, P., Niu, M. and Maddy, J., 2016. The survey of key technologies in hydrogen energy storage. *International journal of hydrogen energy*, *41*(33), pp.14535-14552.

Zhao, Y., Kim, Y.H., Dillon, A.C., Heben, M.J. and Zhang, S.B., 2005. Hydrogen storage in novel organometallic buckyballs. *Physical review letters*, *94*(15), p.155504.

Zhao, W., Fierro, V., Zlotea, C., Aylon, E., Izquierdo, M.T., Latroche, M. and Celzard, A., 2011(a). Activated carbons with appropriate micropore size distribution for hydrogen adsorption. *international journal of hydrogen energy*, *36*(9), pp.5431-5434.

Zhao, W., Fierro, V., Zlotea, C., Aylon, E., Izquierdo, M.T., Latroche, M. and Celzard, A., 2011(b). Optimization of activated carbons for hydrogen storage. *international journal of hydrogen energy*, *36*(18), pp.11746-11751.

Zhao, W., 2012. *Synthesis and characterization of microporous carbonaceous materials for hydrogen storage* (Doctoral dissertation, Université de Lorraine).

Zhao, W., Fierro, V., Aylon, E., Izquierdo, M.T. and Celzard, A., 2013, March. High-performances carbonaceous adsorbents for hydrogen storage. In *Journal of Physics: Conference Series* (Vol. 416, No. 1, p. 012024). IOP Publishing.

Zhao, W., Fierro, V., Fernández-Huerta, N., Izquierdo, M.T. and Celzard, A., 2013. Hydrogen uptake of high surface area-activated carbons doped with nitrogen. *international journal of hydrogen energy*, *38*(25), pp.10453-10460.

Zhao, W., Fan, M., Gao, H. and Wang, H., 2016. Central composite design approach towards optimization of super activated carbons from bamboo for hydrogen storage. *RSC advances*, *6*(52), pp.46977-46983.

Zhao, W., Luo, L., Wang, H. and Fan, M., 2017. Synthesis of bamboo-based activated carbons with super-high specific surface area for hydrogen storage. *BioResources*, *12*(1), pp.1246-1262.

Zhao, W., Luo, L., Chen, T., Li, Z., Zhang, Z. and Fan, M., 2018, June. Activated carbons from oil palm shell for hydrogen storage. In *IOP Conference Series: Materials Science and Engineering* (Vol. 368, No. 1, p. 012031). IOP Publishing.

Zhuang, X., Wan, Y., Feng, C., Shen, Y. and Zhao, D., 2009. Highly efficient adsorption of bulky dye molecules in wastewater on ordered mesoporous carbons. *Chemistry of materials*, *21*(4), pp.706-716.